Novel 3D Ultrasound Imaging Techniques Using Top-Orthogonal-to-Bottom-Electrode (TOBE) Arrays

by

Christopher Ceroici

A thesis submitted in partial fulfillment of the requirements for the degree of

Doctor of Philosophy

in

Biomedical Engineering

Department of Electrical and Computer Engineering

University of Alberta

Abstract

Ultrasound imaging is a safe, affordable and reliable diagnostic tool widely used in medical professions. While 2D ultrasound imaging is used extensively in clinical environments, 3D ultrasound imaging has not yet seen wide clinical acceptance. This is partly due to the practical limitations on the design of 2D ultrasound arrays. Due to system constraints on the number of channels an ultrasound probe can have, fully-connected 2D arrays are often limited in size, resulting in a small numerical aperture with weak focusing power and thus poor image quality. Techniques such as multiplexing and backside electronics have been used to circumvent this problem, however, these approaches often compromise on image quality or result in large, bulky probes requiring liquid cooling. This thesis describes several 3D imaging techniques utilizing Top-Orthogonal-to-Bottom-Electrode (TOBE) arrays. These 2D arrays use a row-column connection scheme to reduce the required number of channels yet maintain the ability to address individual elements in the array.

TOBE imaging schemes are outlined for both ultrasound and photoacoustic imaging applications. The Fast Orthogonal to Row-Column Electronic Scanning (FORCES) imaging scheme is an 3D ultrasound imaging schemes which combines high-quality 2D imaging performance with 3D

imaging capabilities. Using this technique, experimental results are compared with a linear array of similar size. Hadamard-encoded TOBE photoacoustic imaging is an imaging scheme used to acquire 3D volumetric data from photoacoustic signals using TOBE arrays. Unlike previous TOBE photoacoustic imaging schemes, this approach allows for the array to receive across the entire 2D aperture simultaneously resulting in substantially improved SNR. Both imaging techniques are demonstrated with wire-phantom 3D imaging experiments where resolution and SNR measurands are compared. Finally, the combination of FORCES, Hadamard-encoded TOBE photoacoustic, as well as a power Doppler imaging is used to demonstrate multimodal imaging of blood flowing in a tube, imitating a blood vessel. This experiment demonstrates the 3D acquisition of acoustic, flow, and optical contrast using the same array and experimental setup.

Capacitive micromachines ultrasonic can be used as an alternative to piezoelectric/electrostrictive transducers and offer the potential of higher sensitivity. The simulation and design of 2D array CMUT transducers is performed with the goal of minimizing transducer element crosstalk and maximizing transmit power, sensitivity and by extension, reconstructed image quality. This model is coupled with an acoustic field simulator, bridging the gap between the simulation of the design and the imaging array.

Preface

This thesis is a combination of original work by Christopher Ceroici as well as previously published work. Chapters 3, 4, 5, and 6 consist of peer-reviewed research publications by C. Ceroici et al. titled *"Large-Scale Nonlinear Lumped and Integrated Field Simulations of Top-Orthogonal-to-Bottom-Electrode CMUT Architectures"*, *"Fast Orthogonal Row-Column Electronic Scanning (FORCES) with Top Orthogonal to Bottom Electrode (TOBE) Arrays"*, *"Fast Orthogonal Row-Column Electronic Scanning (FORCES) Experiments and Comparisons"* and *"3D Photoacoustic Imaging Using Hadamard-Bias Encoding with Crossed Electrode Relaxor Array*", respectively. Chapter 7 summarizes developments in high-speed imaging not demonstrated in the previously mentioned published works.

Acknowledgements

I would like to thank Dr. Roger Zemp for his guidance and mentorship throughout this research project. The work summarized here would also not have been possible without the assistance from my lab colleagues. In particular, Mohammad Maadi, Ben Greenlay, Quinn Barber, Roger Fu and Ryan Chee. I am also grateful for assistance from Dr. Jeremy Brown and his student Katherine Latham on micromachining of electrostrictive arrays. Finally, I would like to thank Dr. Douglas Barlage and his lab members for their contributions and CMUT electronics design. This research work has been supported by scholarships from NSERC, Alberta Innovates Technology Futures, Faculty of Graduate Studies and Research, as well as the University of Alberta. I am also grateful for the research funding provided by CIHR (grant CPG 134739 and grant PS 153067) and NSERC (grant RGPIN-2018-05788, grant STPGP 396444, grant 355544-2008, grant 375340-2009 grant STPGP 396444, grant EQPEQ 440290, grant EQPEQ 423474, grant EQPEQ 423197, and grant RGPIN355544). Finally, I am grateful for the support of my friends and family who have helped motivate and inspire my work.

Contents

List of Tables

List of Figures

Chapter 1: Introduction

1.1 Objective

Ultrasound imaging is a low-cost, noninvasive imaging technique with numerous clinical applications. However, a major deficiency with modern ultrasound systems is the lack of high-quality and high-framerate 3D imaging technology. This is mostly due to the challenges in producing very dense, fully-connected 2D arrays of piezoelectric transducers. This thesis addresses some of these limitations by investigating a class of 2D ultrasound imaging arrays which can be constructed to have many elements but requires far fewer channels than fully-connected arrays. These array types, called Top-Orthogonal to Bottom-Electrode (TOBE) arrays have several design challenges at the transducer level as well as the system level. This thesis also investigates the simulation and optimization of bias-sensitive transducer arrays suitable for the implementation of large-scale TOBE arrays.

1.1.1 TOBE CMUT Transducer Design and Simulation

In this thesis we consider two types of bias-sensitive crossed electrode transducers: capacitive micromachined ultrasound transducers (CMUTs) and electrostrictive relaxor arrays (relaxors). CMUTs are MEMS (micro-electromechanical systems)-based transducers that offer much higher fractional bandwidth and over four orders of magnitude higher sensitivity per unit area than commonly used piezoelectric-based arrays [1]. However, CMUT membrane mechanics are highly non-linear and therefore computationally expensive to simulate. In addition, small-scale array simulations consisting of only a few CMUTs fail to capture the mutual-acoustic impedance effects that can have substantial impacts on array performance.

A SPICE-based nonlinear CMUT model was created in [2] which can simulate large numbers of CMUT as well as their interactions with relatively low computational requirements. This thesis will investigate the use and modification of this model to accommodate large-scale TOBE CMUT array simulations as well as incorporate acoustic field simulations. This is important not just for the study of TOBE array behavior but also in the design of future large-scale arrays.

1.1.2 TOBE 3D Ultrasound Imaging Scheme Design

Large fully-connected 2D ultrasound arrays are impractical due to the enormous number of channels needed for array sizes with similar aperture sizes as linear arrays (1D arrays). Many approaches exist to circumvent this limitation, but most of these use a form of array multiplexing which limits the number of active elements at any given time [3], [4], [5], [6]. The ability to simultaneously use all elements for transmitting and receiving across a large 2D array would allow

for unprecedented imaging quality but this is not currently possible with conventional array designs.

TOBE arrays, having only row and column electrodes connected along the top and bottom, respectively, have been proposed as a potential solution for this [7], [8]. Although the row-column electrodes in a TOBE array can be used to access information and send driving waveforms across the entire 2D, information cannot be directly acquired from each individual element. As a result, volumes cannot be reconstructed with the same quality as a fully-connected array or a translated linear array. This thesis summarizes novel TOBE imaging schemes which use bias-encoding techniques to maximize the amount of information that can be obtained from the array, and in some cases, obtain datasets equivalent to fully-connected 2D arrays. The imaging schemes can potentially be used for a new class of 3D ultrasound imaging systems that exceed the imaging performance and speed of traditional systems.

1.1.3 TOBE 3D Photoacoustic Imaging

While ultrasound measures the mechanical characteristic of tissue, photoacoustics probes its optical properties. As electromagnetic radiation is absorbed by tissue, thermoelastic expansion generates ultrasound signals which can be detected and used to form images. Since the amount of electromagnetic absorption depends on the optical properties and the amount of pressure depends on the amount of absorption, photoacoustics allows optical information to be obtained using ultrasound at depths much greater than an optical-only system. Photoacoustic imaging has many emerging applications such as measuring oxygen saturation in blood vessels [9] and detecting

optical reporters [10]. 3D photoacoustic imaging has been demonstrated mainly through the use of scanned linear arrays which typically have slow readout times and poor axial resolution [11]. In this thesis we summarize a TOBE array-based 3D photoacoustic imaging scheme which uses Hadamard-bias encoding to acquire full 2D array datasets for volumetric reconstruction. This imaging system can acquire 3D photoacoustic volumes without the need for physical scanning improving the acquisition speed and image quality.

1.2 Key Contributions

1.2.1 Large-Scale TOBE Array Lumped-Model Simulations

Imaging systems consisting of TOBE arrays rely on the ability to precisely control and measure the activity of elements across the entire array. This can be made difficult due to the complex behavior of nonlinear transducers such as CMUTs as well as the complex interactions between actuating transducers across the array. Resource intensive finite element simulation models typically are only capable of modeling a handful of CMUT membranes simultaneously which makes it impossible to measure the impacts of mutual -acoustic impedance on array performance. By utilizing large-scale equivalent-circuit models for CMUTs, we have been able to accurately model the behavior of large 2D arrays of CMUTs. The mutual-acoustic impedance and cross-talk

were validated with laser-vibrometry measurements of an equivalent array. This model was used to perform a series of optimization studies for TOBE array design. Metrics such as transmit power, resistive losses, and crosstalk were optimized by considering various membrane sizes and transducer element layouts.

This tool has been useful in both studying the behavior of large-scale TOBE arrays as well as aid in the design of future arrays. Additionally, the SPICE-based simulation model was used to model the advantages of using on-array thin-film amplifiers to improve the signals-to-noise ration as well as reduce cross-talk.

1.2.2 TOBE Array-Based 3D Ultrasound and Photoacoustic System

TOBE array technology has the potential to alleviate many of the deficiencies of traditional 3D ultrasound technology that have limited its adoption in modern clinical environments. Primarily, most modern 3D imaging systems offer volumetric imaging but with degraded 2D imaging performance. A major challenge in the operation of TOBE arrays is the design of the array operation strategy. Since only row-column connections are available, information from each individual array element is not directly available. This then presents several strategies, or imaging schemes, involving the use of bias-encoding. These TOBE array imaging approaches allow for focusing in both the azimuthal and elevation directions and receiving data from each element across the 2D array, which is not otherwise possible without bias-dependent imaging strategies.

In order to experimentally test both the TOBE ultrasound and photoacoustic imaging schemes, an interface PCB was designed housing the electronics necessary for data acquisition and bias control.

The imaging schemes were programmatically implemented using a Verasonics Experimental Ultrasound System, and control signals were used to drive the interface PCB.

Due to the relatively high computational cost of reconstruction volumetric ultrasound data from raw channel data, GPU-reconstruction programs were developed. These custom CUDA-based scripts interface directly with the imaging system and allowed for as much as a 12000× reconstruction rate improvement over the CPU-based method.

Finally, several ultrasound and photoacoustic experiments were carried out on wire phantoms and an ex vivo rat heart to compare with other imaging methods as well as validate experimental results.

1.2.3 Published Work

Work regarding the simulation of large-scale TOBE arrays was published in the journal IEEE Transactions on Ultrasonics, Ferroelectrics and Frequency Control [12] as well as presented at two conferences [13], [14]. This publication and presentations presented the simulation results of large-scale parasitic effects and resulting design optimizations for TOBE CMUT arrays. Comparisons with measured TOBE CMUT arrays were also compared for validation. This work provides groundwork for a nonlinear model which can be used to predict the parasitic effects of operating large-dense CMUT arrays and design optimizations which can be used to mitigate them. An emphasis is placed on optimizing TOBE array designs where crosstalk and element isolation is particularly important.

The fast-orthogonal row-column electronic scanning (FORCES) TOBE imaging scheme, which allows for high-quality 2D ultrasound imaging while also permitting elevational scanning for 3D imaging, was also published. A simulation-only study comparison FORCES to other 3D imaging schemes was published in the journal IEEE Transactions on Ultrasonics, Ferroelectrics and Frequency Control in [15], and again in [16] where experimental results and comparison were presented. This work demonstrates a TOBE arrays imaging scheme which can match the 2D imaging capabilities of a 2D array as well as perform high-quality 3D imaging. As far as the authors are aware, this has not previously been demonstrated.

The use of TOBE arrays for 3D photoacoustic imaging using a unique bias-encoding scheme was presented at SPIE Photonics West in [17] and [18], and published in Optics Letters [19]. TOBE arrays for 3D photoacoustic imaging had previously been demonstrated in [20] but suffered from low SNR and were not practical for diagnostic imaging. The published TOBE bias-encoding photoacoustic technique greatly improves SNR and represents the only 3D photoacoustic imaging approach which doesn't required mechanically scanned arrays and can be scaled for large arrays.

1.3 Thesis Layout

Chapter 2: of this thesis will provide background information on ultrasound transducers and reconstruction techniques, specifically for 3D imaging. Difference strategies for 3D ultrasound are summarized here with the advantages and disadvantages of each indicated.

Chapter 3: describes a top-orthogonal to bottom-electrode (TOBE) capacitive micromachined ultrasound transducers (CMUTs) simulation model. Examples are shown of using this model for optimizing the design of TOBE CMUT arrays to reduce crosstalk.

Chapter 4: demonstrates the fast-orthogonal row-column electronic scanning (FORCES) approach through simulations. This is TOBE array approach is compared with other 3D imaging schemes.

Chapter 5: takes the same FORCES imaging scheme and presents experimental 3D imaging results using a relaxor array. These results are compared with other schemes.

Chapter 6: describes a similar TOBE array imaging scheme incorporating bias patterns but for 3D photoacoustic imaging. This was demonstrated experimentally with a relaxor array and compared with a different approach where bias patterns are not used.

Chapter 7 summarizes developments in high-speed TOBE array 3D imaging using faster bias switching electronics and GPU-based reconstruction.

Finally, Chapter 8: will conclude the thesis with a brief summary as well as a discussion of the information presented here in the scope of other research work.

Chapter 2: Background

2.1 Ultrasonic Imaging

Ultrasound imaging is widely used in clinical applications such as diagnosing illnesses, surgical guidance, as well as therapeutic techniques. From an imaging perspective, ultrasound imaging systems are fast, low-cost compared to magnetic resonance imaging (MRI), and safer than imaging techniques such as X-ray imaging. In contrast to most imaging systems utilizing electromagnetic radiation, ultrasound imaging uses the time-of-flight information of sound propagating through the medium to determine the depth of scattering. This is accomplished by transmitting ultrasound

signals of frequencies in the range of 20 kHz to the GHz regime and measuring the time it takes for scattered signals to return to the transducer. Since different feature of interest such as blood vessels, organs and tumors will have different acoustic impedances from the surrounding tissue, these structures will scatter ultrasound signals, providing acoustic (mechanical) contrast [21].

Unlike with most optical imaging systems, the acoustic time-of-flight information provides depth, or axial resolution of the area of interest. Typically, an ultrasound transducer will consist of a horizontally-distributed arrangement of elements. The separation of the sensing elements allows for resolution to be obtained in the x-direction, or azimuthal resolution. Axial resolution can be approximated as 2λ, where λ is the wavelength of ultrasound used. While the axial resolution will mainly depend on the center frequency (and therefore wavelength) of the ultrasound, the bandwidth (or 3dB bandwidth) of the transducer will also impact the axial resolution since this will limit how short of a transmit pulse can be transmitted and received. The lateral resolution can be approximated as:

$$lateral\ resolution \cong\ 1.4\lambda f_{\#} \tag{2.1}$$

where $f_{\#}$ is the f-number defined as $f_{\#} = F/D$ where F is the focal distance and D is the aperture size. This illustrates in order to achieve a small (finer) lateral resolution the array should have a large aperture size along with a high center frequency $f = c/\lambda$, where c is the speed of sound in the medium. This can present a design challenge, since higher frequency arrays require densely packed elements, or smaller element pitches, to minimize side-lobe artifacts [22]. To maintain small element pitches while maximizing the aperture size, large numbers of elements must be used which can increase costs and complexity.

This type of 1D array, illustrated in Figure 2.1, is referred to as a linear array. With axial and azimuthal resolution, a linear array is capable of obtaining images in XZ-plane, also known as B-scan images.

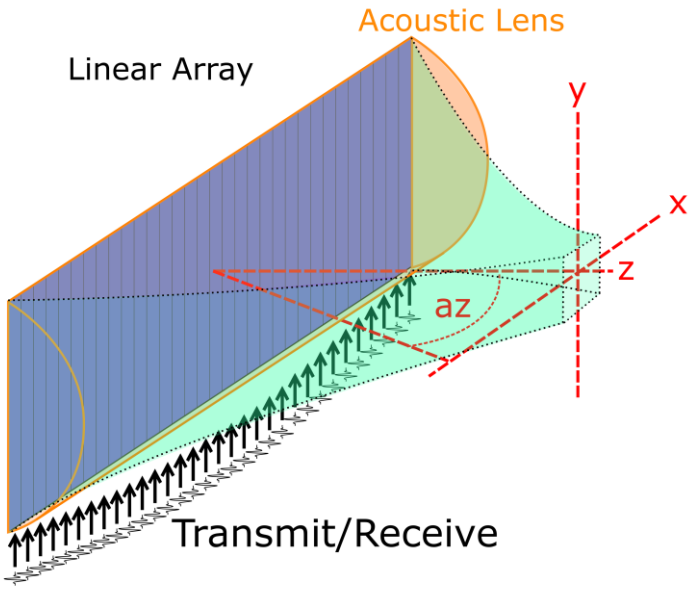

Figure 2.1: Illustration ultrasound linear array (1D array) with a fixed acoustic lens.

In the case of a 2D array where elements are also distributed in the y-direction, elevationally spaced elements provide elevational resolution.

2.2 Photoacoustic Imaging

An alternative to traditional pulse-echo ultrasound imaging, photoacoustic imaging is a technique which uses light to generate ultrasound signals which can then be measured using an ultrasound transducer [23], [24] or optically [25], [26]. Optical imaging methods tend to have high contrast but suffer from high scattering in tissue, limiting the imaging depth, as well as long readout times. By using rf waves to generate ultrasound waves, which have significantly less scattering in tissue, high resolution and contrast are achieved at greater depths. Photoacoustic imaging allows for imaging techniques beyond the purely mechanical measurement properties of ultrasound imaging such as oxygen saturation measurement [9], optical contrast agents [10], and imaging microvasculature [27].

Photoacoustic imaging is enabled through the photoacoustic effect in which a laser pulse is absorbed by tissue and generates heat. This heat results in thermoelastic expansion of the tissue and an increase in pressure p_0 which can be approximated by [28]:

$$\mathrm{p_0} = \left(\frac{\beta \mathrm{c}^2}{\mathrm{C_p}}\right) \mu_\mathrm{a} \mathrm{F} \tag{2.2}$$

where β is the isobaric volume expansion coefficient, C_p is the specific heat, μ_a is the absorption coefficient, F is the light fluence and c is the speed of sound. The dependence of $\mathrm{p_0}$ on the fluence, which is the optical energy per unit area, as well as μ_a, shows that the emitted pressure is proportional to the optical absorption of the material. When applying a heating function $H(r,t)$, a pressure $p(r,t)$ at position r and time t is produced obeying the following wave equation:

$$\nabla^2 \mathrm{p(r,t)} - \frac{1}{\mathrm{c}^2}\frac{\partial^2}{\partial \mathrm{t}} \mathrm{p(r,t)} = -\frac{\beta}{\mathrm{C_p}}\frac{\partial}{\partial \mathrm{t}} \mathrm{H(r,t)} \tag{2.3}$$

Scanned ultrasonic linear arrays have been used for photoacoustic imaging in [11] but suffer from poor elevational resolution and imaging speed. Ring array transducers [29] and sparsely connected 2D arrays [30] have also been used but suffer from increased imaging artifacts and lower SNR than a densely- or fully-connected 2D array.

Since no ultrasonic transmission is required of the array during photoacoustic imaging, a TOBE array can be used to effectively acquire data from every element in the array in a similar manner to a fully-connected array of the same size [31]. This can be done by biasing one column at a time and receiving along rows. Each row signal is equivalent to the signal received by the single biased element in that row. This can be improved upon by using bias encoding, which will allow for the entire array to receive signals for every acquisition and then decoded afterwards.

2.3 Ultrasound Beamforming

The transducer elements are sensitive to acoustic energy, and in response to incident pressure waves will produce measurable electrical traces. Since information regarding the structure and position of the imaged objects is encoded into the time-of-flight information of the received traces at each element, calculations can be performed on the ensemble of element channel data to predict the locations of acoustically scattering structures. This process is commonly referred to as beamforming, or dynamic receive beamforming (DRBF). A common method of achieving this is the delay-and-sum (DAS) beamforming algorithm [32]. In this approach, the expected delay times

are calculated from each transducer element's position to each pixel location on the reconstruction grid. The value of each pixel in the reconstruction grid is then obtained by summing the signal traces for all elements at the time delay associated with the pixel's location. This is summarized with the following equation:

$$y_{ij}(t) = \sum_{n=1}^{N} g_n(t, \delta_n(i,j)) \qquad 2.4$$

where $\delta_n(i,j)$ is the time delay value in samples from element n to the pixel at (x=i,y=j), g_n is the signal trace for element n, and y_{ij} is the pixel value for the pixel at (x=i,y=j). The reconstruction grid is illustrated in Figure 2.2. i and j grid locations

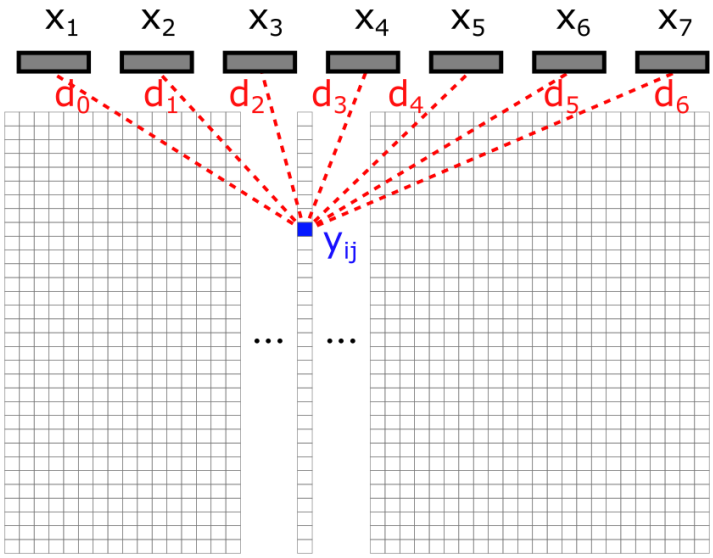

Figure 2.2: Dynamic receive delay-and-sum beamforming for a linear array. The received ultrasound trace at each element x_n is delayed by the time delay difference between the transducer element position and the point (i,j) being reconstructed which is calculated from the distance $d_n(i,j)$ between the element and y_{ij}.

Since it is often desirable to obtain a B-scan within a narrow XZ-slice of tissue, linear arrays typically use a fixed acoustic lens which focusses the acoustic fields in the Y, or elevational direction.

The propagation time is typically measured from the moment that the array transmits a signal. The time-of-flight therefore is equal to the sum of the time required for the transmitted pressure to reach the scatter and the propagation time from the scatter back to the array. This means that the DAS calculation is heavily dependent on the transmitted pressure pattern. In the simplest case, all elements transmit simultaneously resulting in a flat plane-wave beam pattern, also known as flash imaging, shown in Figure 2.3. The transmit delay can then be approximated as dependent only on

depth, with no lateral dependency. A major disadvantage of flash imaging is that the beamformer cannot determine which transmitting element was the source of the pressure, since all elements are transmitting and only the sum of all sources can be measured. This means that flash imaging is unable to perform transmit focusing retrospectively, resulting in poor lateral resolution.

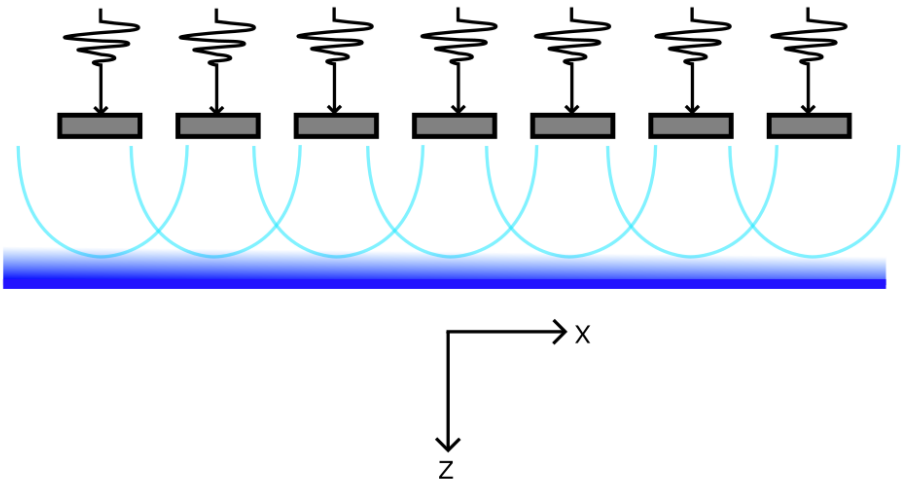

Figure 2.3: Flash imaging transmit beam shape. The transmitted beam pattern in this case can be approximated as having only a z-dependency.

An alternative to flash imaging is synthetic aperture imaging (SAI) [33]. Unlike with flash imaging, SAI involves transmitting only on a single element at a time while receiving on all elements, as shown in Figure 2.4. The next adjacent element then transmits and so on until every element has transmitted.

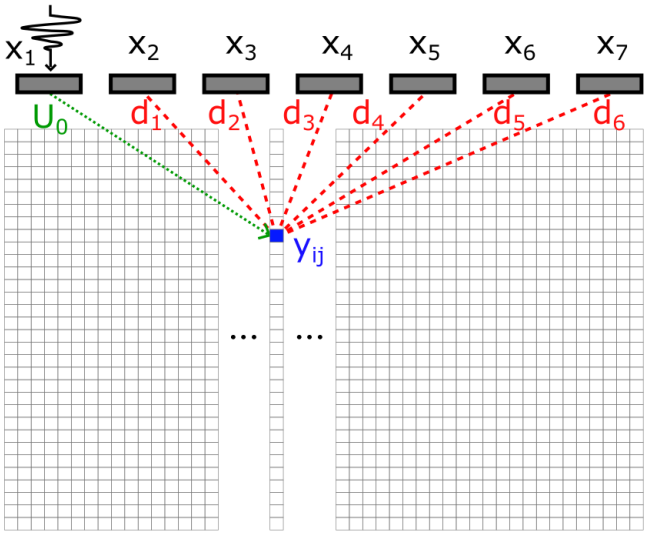

Figure 2.4: Synthetic aperture imaging with dynamic receive beamforming. A single transmitting element x_1 allows for transmit focusing due to the direct knowledge of the source of the transmitted pressure wave.

The advantage in this case is that, for each acquisition, the beamformer has direct knowledge of the travel path of the transmitted and scattered pressure waves. Where previously only the receive delay was considered, SAI will also consider the transmit delay U_k between the transmitting element and point y_{ij} for the SAI acquisition k. After the entire dataset has been accumulated, the retrospective SAI transmit beamforming can be performed during the DRBF calculations. Each SAI transmit event B-scan is beamformed separately using this process and then summed together for the final reconstructed B-scan. One major limitation of SAI is that only a single transmitting element is active per transmit event which limits the SNR of the reconstructed image. This disadvantage can be addressed using coded-aperture imaging [34], [35], where instead of transmitting on a single element, multiple elements transmit signals. By transmitting from certain elements according to a pattern that derives from an invertible matrix such as a Hadamard matrix

or S-matrix, the receive data can be decoded and a version of the channel data can be obtained that resembles the case where only a single element transmitted at a time (traditional SAI) but with much higher SNR.

Another method of performing transmit beamforming is to use active transmit delays. By applying delays to each transmitting element, the transmit beam can be steered and focused to a particular direction of point. These delays are calculated based the distances between each element and the desired focal point or angle. Figure 2.5 shows the simulated transmit pressure from a linear array electronically focused to point.

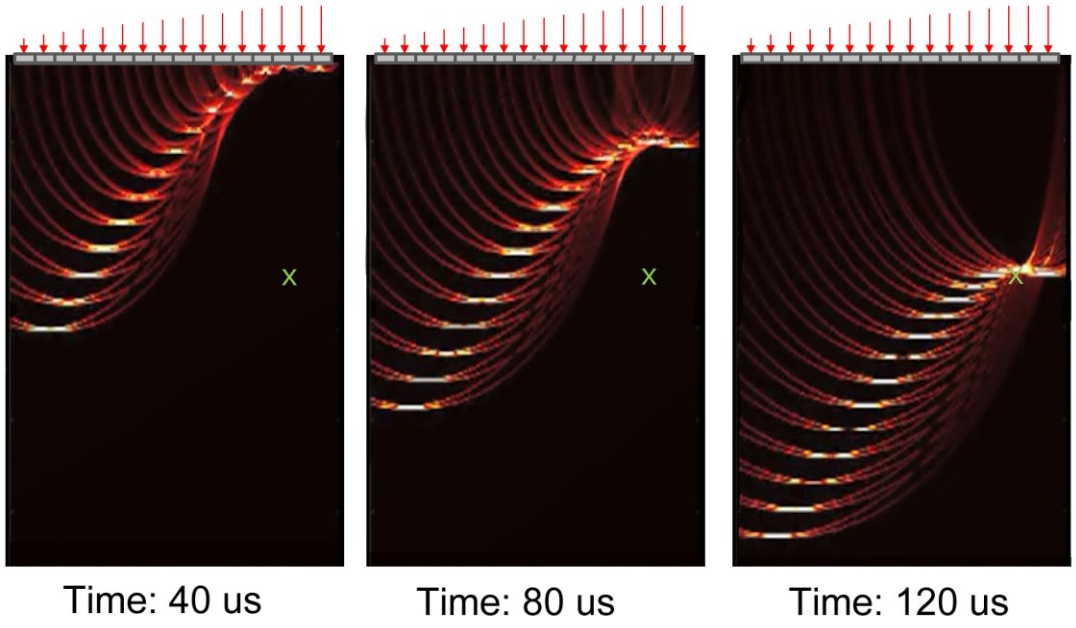

Figure 2.5: Simulated pressure in the azimuthal plane of a 16-element linear array with an electronically generated transmit focus at the location of the green 'x'. Three different frames are shown at 40 μs, 80 μs and 120 μs.

In many cases, a 3D reconstruction is desirable. With a linear array, a 3D reconstruction can only be obtained by mechanically translating or rotating the array in the elevational direction since the

array has a fixed elevational focus. However, this is slow and often leads to poor elevational resolution. A preferable approach is to arrange the transducer elements in a 2D grid instead of a 1D line. With elements distributed in both the X- and Y directions, both azimuthal and elevational resolution can be obtained using delay-and-sum beamforming. The previously described methods of beamforming also apply to 3D imaging but with the additional elevational (y-axis) directional component included in the acoustic travel path.

2.4 3D Ultrasound Imaging

2.4.1 Scanned Linear Arrays

To acquire acoustic information along both the lateral (azimuthal) and elevational directions, a linear array can be mechanically stepped elevationally to acquire multiple elevational slices which can then be formed into a volumetric image [11], [36] as illustrated in Figure 2.1. The advantage of this approach is that high-frequency and large-aperture 1D arrays can be used which can acquire very high quality and high-resolution B-scan images. However, the requirement for mechanical scanning means that volumetric acquisition can be slow. Rather than using fixed motors to translate the linear probe, freehand 3D ultrasound can be used by attaching a positioning sensor to the probe [37]. This was used as an intro-operative neurosurgical imaging tool in [38] where a bulky scanning motor would be unsuitable. Drawbacks of this approach include the dependency of image quality of the accuracy of the positioning sensors as well as the requirement for repeated calibration. Cenni et al. in 2016 demonstrated a freehand 3D ultrasound system based on a 10 MHz

linear probe with high volumetric reconstruction accuracy (less than 3% disagreement across multiple experiments) [39]. This system required a crossed-wire phantom in a water tank for calibration purposes as well as multiple cameras for position tracking. Due to the complexity of positional calculations, the data was processed off-line with an approximate processing time of 450 seconds per volume, limiting the potential for real-time 3D imaging.

In general, 3D imaging systems consisting of linear probes suffer from poor axial resolution due to the presence of an acoustic lens. An acoustic lens with a relatively tight focus is needed in order to restrict the acoustic pressure along a particular elevational slice. The tighter the focus, however, the smaller the axial working distance which can result in poor resolution and SNR at depths away from the fixed focal depth, as shown in Figure 2.6.

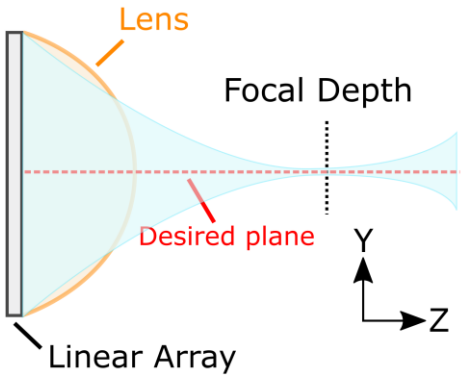

Figure 2.6: Side view (YZ-plane) of a linear probe with an acoustic lens. The Desired B-scan to be acquired is shown as the dashed red line. With a fixed axial focus, however, acoustic energy is unfocused away from the focal depth. This limits the system's ability to section individual elevational planes. As the array is stepped in the elevational direction, regions away from the focal depth suffer from poor elevational resolution.

2.4.2 Matrix Probes and Sparse 2D Arrays

By distributing elements in both the x and y (azimuthal and elevational) directions, DRBF can be directly performed across a 3D space, rather than compositing multiple 2D beamformed images. A major challenge with this approach is that the number channels required for large 2D arrays grows quadratically. For example, many linear array probes use 192 channels. To extend the same aperture size and channel density into a 2D array, 36,864 channels would be needed. In contrast to other sensor types, ultrasonic channels require a substantial amount of electronics and preprocessing due to the need to capture thousands of time samples of pressure for each channel. This means that large number of channels (typically >1000) are often impractical from a design

point of view, since the system would become extremely expensive and difficult to use with very large cables. In addition, the array design itself becomes very challenging with this type of connection scheme since each element connection must be routed to a digitizer through a dense arrangement of elements. This is especially true for high-frequency 2D arrays (giving higher resolution) since elements are packed even more densely. In [40], a 3 MHz, 32×32 element array is used for ultrafast 3D imaging. The imaging system consists of 1024 transmit channels, and 512 receive channels which use 2:1 multiplexing to address the entire array. Due to the limitation of receive channels and the requirement for multiplexing, each acquisition is repeated for one half of the array. This system is capable of volumetric blood flow imaging at approximately 100 volumes per second but the focusing ability and resolution is limited by the small aperture.

Several approaches have been used to circumvent the 2D array high channel count problem. Matrix probes consist of a 2D array of elements, but rather than routing each element from the transducer, interposer electronics are used directly on the transducer to reduce the channel count. These electronics can consist of simple multiplexor to activate different sections of the array, or microbeamformers which perform intermediate reconstruction tasks to reduce the amount of data which needs to be communicated to the ultrasound system [41], [42]. Matrix probes offer the possibility of driving large numbers of elements in a 2D array, and in some cases the entire array. In [42], Savord et al. demonstrates a 2D matrix transducer consisting of approximately 3000 transducer elements. All elements can be sample from simultaneously, and only 128 wires are used communicate data from the probe to the ultrasound system. This is accomplished by integrating microbeamforming circuity into an ASIC attached to the back of the array. Subsections of the array are beamformed independently using these back-end analog electronics, and the resulting

beamformed subsections are digitized and combined on the system side into a final 3D volume. More recently, probes such as the Phillips xMatrix, demonstrated in [43], can support as many as 9,000 elements using this technique. Since there must be interconnects between each element and the analog electronics, this approach requires the use of an ASIC with a surface area equivalent to the size of the array. This limits the overall size of the array, since for larger apertures, ASIC dies capable of spanning the entire size of the array (eg. > 2 cm^2) would become impractically expensive. In addition, the analog electronics must fit within each element's footprint. For a 10 MHz array, elements with a wavelength pitch would have a footprint of 154 μm. But for applications where higher resolutions are required, higher frequencies as high as 40 MHz would be needed, resulting in an element pitch of 38.5 μm. Fitting the same electronics in this area is much more difficult, especially considering that many matrix probes already require bulky active cooling systems across the array due to the power density of the these electronics, such as in [44]. As a result, matrix probes with backside ASIC electronics are often limited to operating at less than 15 MHz.

Sparse 2D arrays address the high channel count problem by only connecting a sparse selection of elements across the array chosen either randomly or in a period pattern [45], [46]. This allows for a 2D array with a large aperture size (providing higher resolution) but with a low channel count. However, sparse 2D arrays have rarely been used for clinical applications due to compromises on image quality. In [47], Lockwood et al. shows that for a 64×64 element array, a sparse 2D array can acquire B-scans at multiple elevations at 1,000 frames/sec, while a conventional 64 element linear array will be substantially slower due to the limitations of mechanical scanning systems. However, the sparse array is shown to have an SNR 4.7 dB lower than a conventional 64 element

linear array due to the inhomogeneous transmit radiation pattern. A sparse arrangement of elements, whether distributed randomly or periodically, results in diminished focusing ability and SNR. Periodically distributed sparse arrays tend to produce gradient artifacts due to large effective element pitches while randomly distributed sparse arrays tend to result in large side lobe artifacts.

2.4.3 TOBE Arrays

TOBE arrays, also known as crossed-electrode or row-column arrays, were first suggested as a method of 3D ultrasound imaging in [48] and later demonstrated experimentally in [8]. Any type of transducer can be connected in a TOBE connection scheme such as piezoelectric composites [7], or micro-electromechanical system (MEMS) -based piezoelectric [49] and capacitive [50], [51], [52] transducers. TOBE arrays allow for a relatively small number of row- and column-electrodes to address a large 2D array. Figure 2.7 illustrates a simple method of using TOBE arrays for 3D imaging by transmitting and receiving along both rows and columns interchangeably. This strategy is similar to that demonstrated in [7], where a 5 MHz, 256×256 element row-column array consisting of a 1-3 piezoelectric composite is used for phantom imaging experiments. A 64×64 2.7 MHz is also shown in [50], this time using CMUT elements fabricated with a wafer bonding approach. These demonstrations show that the images acquired from a row-column arrays are similar to that of a linear array. This is expected considering that receiving across rows and then columns is equivalent to acquire with a linear array at two different orientations. This is useful for imaging the central Z-X and Z-Y orthogonal planes but not for full volumetric imaging where reconstructions along the X-Y or an arbitrary plane are desired.

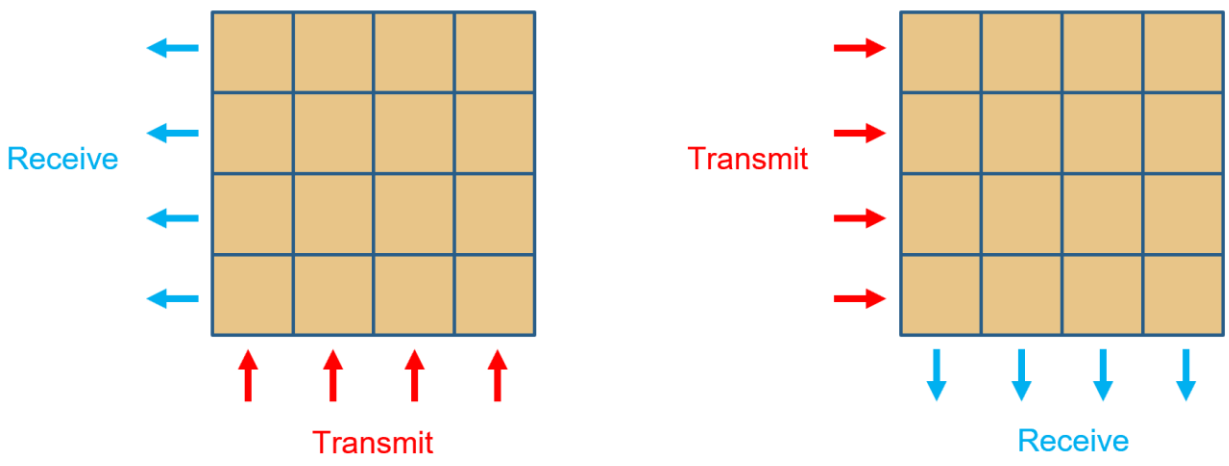

Figure 2.7: Example of simple TOBE array 3D imaging scheme. Row and column electrodes are interchangeably used a transmit and receive channels and the reconstructed volumes are compounded.

Another approach which has been proposed is compounding multiple steered plane waves [53]. This allows for a form of transmit focusing along the direction of the steered plane waves. Since the transmit waves can only be steered along either the rows or columns, this focusing can only be applied elevationally or azimuthally. In each case, the resolution and sidelobe levels suffer in the other direction. Finally, TOBE array synthetic transmit aperture imaging was proposed in [54]. This was compared with explososcan, a commonly used 3D imaging approach using fully or partially connected 2D arrays, in [6] where it was found to have near-equivalent imaging quality. These previous approaches suffer from the inability to address individual elements on transmit or receive using only row and column electrodes. For example, transmitting at only a single element in the center of the array is impossible using only AC pulses along row and column electrodes. In order to accomplish this, and more complex row-column array behavior for improved imaging

performance, more complex imaging strategies combined with bias-sensitive transducers can be used. Bias-CMUT row-column arrays have been demonstrated in [49] and [52], however, imaging is performed using the rows and columns as orthogonal 1D arrays, such as in Figure 2.7, rather than using the bias sensitivity for improved addressing. [55] introduces an imaging scheme for a row-column array of piezoelectric elements where high-voltage switched are used to toggle row-column connections to create synthetic aperture focusing. An example of using bias switching to create patterns, or codes, across the array is [56]. In this case, bias-sensitive CMUT elements allow for a coded SAI approach with a TOBE array resulting in a 37.2 dB SNR improvement over the approach illustrated in Figure 2.7 with wire phantoms. This is shown only in simulations and doesn't address the added complexity of bias switching electronics. Furthermore, an S-sequence encoding approach is used here, where the coding matrix is a truncated Hadamard matrix with all -1s replaced with zeros. This means that many applied biases will be at 0V at a given time, and there will be fewer active transmitting and receiving elements resulting in poorer SNR.

A summary of 3D ultrasound imaging technologies is shown in Table I, comparing the imaging quality, speed and practicality of the discussed methods.

Table I: Comparison of 3D Imaging Speed, Quality and Practicality for Existing 3D Ultrasound Technologies

3D Imaging Technique	# of Channel Needed for Array Size N	Imaging Quality	Imaging Speed	Practicality
Scanned Linear Array	N	High in azimuthal plane, low in elevation	Slow	Widely used due to simplicity
Fully Connected 2D Array	N^2	High	High	Limited by high channel counts
Sparse 2D Array	$<N^2$	Low	High	Limited by imaging artifacts
Matrix Arrays	$<N^2$	High	High	Expensive to manufacture, but more practical than fully connected
TOBE Arrays	2N	High, equivalent to linear array	Depends on imaging scheme	Lack of high-quality 3D imaging schemes has limited field of use

2.5 Bias-Sensitive Ultrasound Transducers

Bias sensitive transducers are transducer which are only sensitive to ultrasound and only transmit ultrasound when a DC electric field is applied across them. This can be useful for a variety of imaging techniques, but mainly because it allows for modulation and addressing of array elements across large arrays. Bias dependency is particularly useful for TOBE arrays since merely using the AC transmit signals along the row or column electrodes allows for only minimal control over the arrays imaging behavior. DC biasing presents an additional level of control for these types of arrays, allowing for a wide range of imaging techniques for improving resolution and SNR.

Two main types of bias-sensitive transducers are considered here: capacitive micromachined ultrasound transducers (CMUTs) and electrostrictive relaxor transducers (relaxors).

2.5.1 Capacitive Micromachined Ultrasound Transducers

Capacitive micromachined ultrasonic transducers (CMUTs) are a type of micro-electro-mechanical system (MEMS) based transducer. Shown in Figure 2.8, CMUTs consist of a flexible, conductive membrane suspended over a gap, with a second conductive electrode at the bottom of the gap. When a voltage is applied across the top membrane and bottom electrode the membrane deflects, resulting in a change in the CMUT capacitance which can be modeled using the expression:

$$C(t) = \frac{\varepsilon_0 \pi a^2 \tanh^{-1}\left(\sqrt{\frac{x_p(t)}{a}}\right)}{2\sqrt{t_{ge} x_p(t)}} \qquad 2.5$$

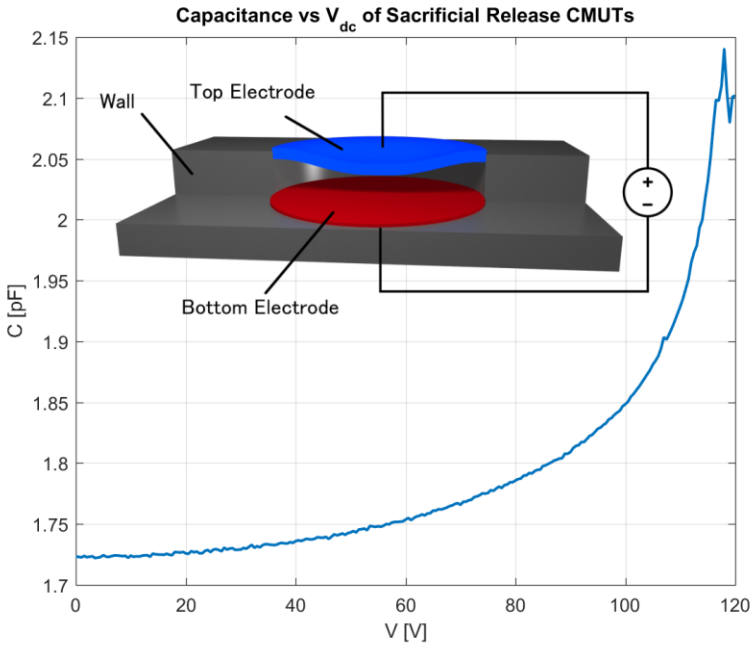

Figure 2.8: Cross section of CMUT with Capacitance-Voltage measurement sweep of a sacrificial release CMUT TOBE array element.

derived in [57], where C is the CMUT capacitance, a is the membrane radius, $x_p(t)$ is the peak membrane deflection and t_{ge} is the effective membrane gap. A measurement of the change of capacitance with an increasing bias voltage is shown in Figure 2.8.

If an AC voltage is applied, the membrane will oscillate and generate ultrasound radiation. Similarly, when an ultrasound signal is incident on the array it will cause the membrane to oscillate which will generate a voltage signal. These two mechanisms allow for the pulse-echo imaging procedure, which is necessary for forming ultrasound images. As the membrane deflects, the sensitivity of the CMUT, defined as the change in capacitance experienced with a change in deflection, $\partial C/\partial V$, increases. Thus, CMUTs display a highly nonlinear deflection-applied voltage relationship and are bias sensitive. By biasing CMUTs near the snapdown region, where the

electric field is strong enough to completely pull down the membrane, high sensitivities can be reached. CMUTs have been shown to display higher sensitivity and much wider bandwidth than piezoelectric transducers [58]. Additionally, CMUT fabrication is very scalable when compared to other ultrasound array technologies such as piezoelectric, which are complex to manufacture in comparison. As a result, large-scale, high-density 2D CMUT arrays can be fabricated in a TOBE wiring configuration without the need for on-chip electronics or an impractically large number of channels.

There are two main methods for fabrication CMUTS: sacrificial release and wafer bonding. The sacrificial release process, illustrated in Figure 2.9 (a), creates a gap underneath the membrane by etching a sacrificial poly-silicon layer underneath the SiN membrane. The wafer bonding approach, illustrated in Figure 2.9 (b), involves etching the gap into a SiO_2 layer on top of a SOI wafer device layer. This oxide surface is then bonded to the device layer of an additional SOI wafer

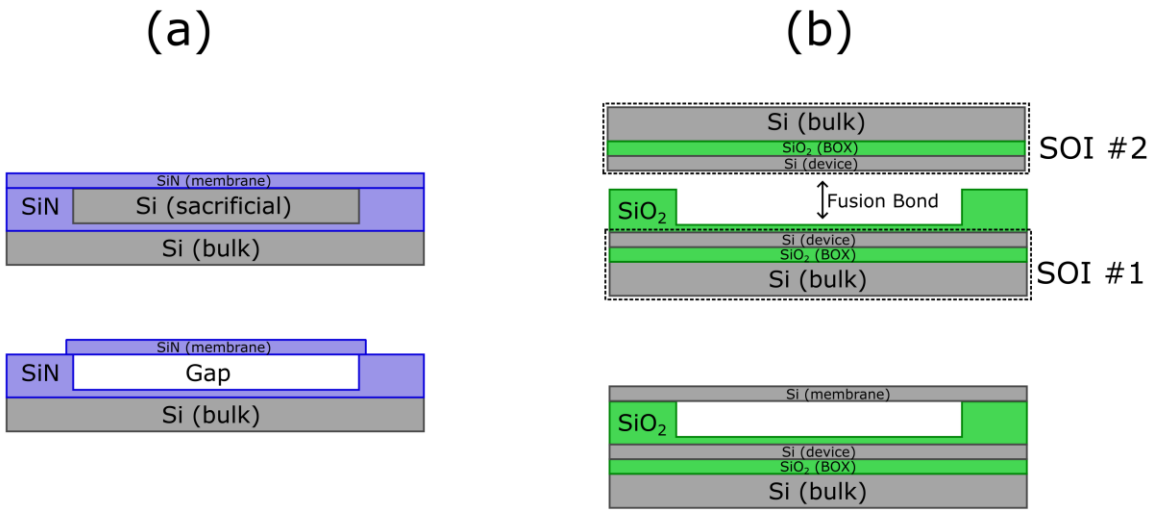

Figure 2.9: Summary of CMUT fabrication techniques: (a) sacrificial release and (b) wafer bonded.

and the handle (bulk Si and buried SiO_2) of the second SOI is remove, leaving only the device layer as the CMUT membrane.

While CMUTs have sensitivity and bandwidth advantages over piezoelectric transducers, they require high DC voltages to reach the deflections that offer high sensitivities. This can pose challenges from an electrical design and safety point of view, but also because of dielectric charging effects. With high electric fields applied across a dielectric, charges can become trapped in the dielectric, resulting in a long-term and sometimes permanent electric field [59]. This effect is especially pronounced when the membrane snaps down, as the field strength sharply increases. Charging means that as the device operates, increasing biases are needed to maintain the desired deflection and sensitivity. Solutions to this problem such as isolated isolation posts in [59] have been proposed to eliminate charging effects.

2.5.2 Electrostrictive Relaxor Transducers

Another type of bias-sensitive transducer discussed in this thesis are electrostrictive relaxor arrays [60], [61], [62]. These are materials in which the electrorestrictive effects are dependent on an applied electric field. Relaxors are ferroelectric materials that exhibit high electrostriction.

Now to describe the difference between piezoelectric and electrostrictive tranducers. We begin by explaining the forward piezoelectric effect. The forward piezoelectric effect involves material strain upon applying an electric field, usually from applying a voltage between a top and bottom electrode. The inverse effect involves creation of voltages upon application of a force. These effects are due to molecular asymmetries and require polarized domains in the material. These domains are polarized via a poling process with high voltages and high temperatures. When the

material cools, residual polarization results in the piezoelectric behavior with strains and voltages roughly linearly proportional. Piezoelectric transducers exhibit both a forward and inverse piezoelectric effect.

Electrostrictive transducers, in contrast have no inverse piezoelectric effect, that is, unless there is an applied bias voltage. Electrostrictive transducers exhibit strains that are quadratic with applied voltages. In tensor notation, a strain can be modelled as $\epsilon_{ij} = Q_{ijkl} D_k D_l$, where Q_{ijkl} is the electrostriction tensor, and D_k are components of the electric displacement field, equal to the sum of applied electric field and residual/induced polarization: $D_k = \varepsilon E_k + P_k$.

More generally, the displacement field can be viewed as a component of the electric field that changes quickly, and a component associated with a slower polarization response. From Y. Feldman et al., Dielectric Relaxation Phenomena in Complex Materials, this can be written as:

$$D(t) = \varepsilon_0 \left[\varepsilon_\infty E(t) + \dot{\Phi}(t) * E(t) \right],$$

where $\Phi(\mathrm{t}) = (\varepsilon_r - \varepsilon_\infty)[1 - \phi(t)]$, * is temporal convolution, $\phi(t) = P(t)/P(0)$, and ε_r and ε_∞ are the low- and high-frequency limits of relative dielectric permittivity. The complex frequency-dependent permittivity is related to ϕ as:

$$\frac{\varepsilon^*(\omega) - \varepsilon_\infty}{\varepsilon_r - \varepsilon_\infty} = \mathcal{L}\left\{ -\frac{d}{dt}\phi(t) \right\},$$

where $\mathcal{L}$ is the Laplace Transform operator. The Debye model for ϕ is a decaying exponential: $\phi(t) = e^{-\frac{t}{\tau_m}} u(t)$ where $u(t)$ is a step function and where τ_m is the characteristic relaxation time. Many other more complex phenomenological models of relaxation have also been proposed.

When the thickness-mode excitation axis is $k = 3$, and electric fields are applied in this direction, and when there is a residual polarization, the relevant strain is $\epsilon_{33} \propto Q(\varepsilon E_3 + P_3)^2$, where $Q = Q_{3333}$. Dropping subscripts for convenience, the AC strain due to a transient voltage excitation δE is $\epsilon_{AC} \propto HPF\{(\varepsilon(\delta E) + P)^2\} \propto \varepsilon P \delta E$ to first order in δE. This is the forward piezoelectric effect showing linearity with excitation voltage. Thus piezo-electricity is described here as an electrostrictive effect when there is a residual polarization present. For a purely electrostrictive material, there is no residual polarization, $P_k = 0$. However, if the transducer is biased with a DC electric field E_3, then, again dropping subscripts: $\epsilon_{AC} = h(t) * \epsilon_{33}$ where h is the bandpass transducer electromechanical response, thus $\epsilon_{AC} = h * Q\{D(t)^2\}$. Expanding, we have

$$\epsilon_{AC} = h(t) * \left(\varepsilon_0\left[\varepsilon_\infty E(t) + \dot{\Phi}(t) * E(t)\right]\right)^2 Q = h(t) * \left(\varepsilon_0\left[\varepsilon_\infty (E + \delta E) + \dot{\Phi}(t) * (E + \delta E)\right]\right)^2 Q$$

$$= h(t)$$

$$* \left\{\varepsilon_0^2 \varepsilon_\infty^2 (E + \delta E)^2 + 2\varepsilon_0 \varepsilon_\infty (E + \delta E)\varepsilon_\infty \dot{\Phi}(t) * (E + \delta E)\right.$$

$$\left. + \varepsilon_0^2\left[\dot{\Phi}(t) * (E + \delta E)\right]^2\right\} Q$$

When $E(t) = E$ is a constant DC field, we have

$$\dot{\Phi}(t) * E(t) = E \int_{-\infty}^{\infty} \dot{\Phi}(t)dt = -E(\varepsilon_r - \varepsilon_\infty) \int_0^\infty \dot{\phi}(t)dt = (\varepsilon_r - \varepsilon_\infty)E\big(\phi(0) - \phi(\infty)\big) =$$

$(\varepsilon_r - \varepsilon_\infty)E$.

when the material has a large relative dielectric constant, as in our case (e.g. PMN has a giant relative permittivity of 20,000), the relative permittivity $\varepsilon_r \gg \varepsilon_\infty$ and we have that $\dot{\Phi}(t) * E \approx \varepsilon_r E$.

Also, when the transducer is driven with an AC electric field $\delta E(t)$ with a frequency much higher than the relaxation-rate $1/\tau_m$, the material cannot adequately respond and $\dot{\Phi}(t) * \delta E \approx 0$ (or small). Thus,

$\dot{\Phi}(t) * (E + \delta E) \approx \varepsilon_r E.$

Simplifying with these approximations:

$$\epsilon_{AC} \approx h(t) * \{\varepsilon_0^2(2E\delta E + \delta E^2) + 2\varepsilon_0\varepsilon_\infty \delta E \varepsilon_0 \varepsilon_r E\} Q$$
$$= h(t) * \{\varepsilon_0^2\varepsilon_\infty^2(1 + \varepsilon_r/\varepsilon_\infty)2E\delta E(t) + \varepsilon_0^2\varepsilon_\infty^2\delta E^2(t)\} Q$$

When $\varepsilon_r \gg \varepsilon_\infty$, and when $2\varepsilon_r E \gg \varepsilon_\infty \delta E$ (i.e. $\delta E/E \ll 2\varepsilon_r/\varepsilon_\infty$), this becomes simply

$$\epsilon_{AC} \approx 2Q(\varepsilon_0^2\varepsilon_\infty\varepsilon_r E)(h(t) * \delta E(t)) = h(t) * 2QP_I(\varepsilon_0\varepsilon_\infty\delta E(t))$$

Here $P_I = \varepsilon_r E$ is an induced polarization, and $2QP_I$ is an effective (induced) piezoelectric coefficient.

Thus, the material behaves like a piezoelectric material with approximate linearity in driving voltage δE. Importantly, the induced polarization εE has a polarity dependent on the biasing field polarity. This leads to important properties that we require for bias-encoded imaging schemes discussed below. In particular, the response to an excitation δE with a positive bias is the same as that of an amplitude-inverted excitation $-\delta E$ with a negative bias: $\epsilon_{33} = Q(E_3 + \delta E_3)^2 = Q(-E_3 - \delta E_3)^2$. Also, $Q(E_3 - \delta E_3)^2 = Q(-E_3 + \delta E_3)^2$. Likewise, measured voltage signals $\delta V \propto \delta E$ depend linearly on AC strain and bias voltage to first order. Thus, the received signal due to a pressure transient δp received with a positive bias voltage is effectively polarity inverted with a negative bias voltage.

Electrostrictive transducers have been investigated for many years but our recent work has fabricated bias-switchable row-column arrays and demonstrated new ways of using these arrays for unprecedented ultrasound and photoacoustic image quality.

2D relaxor arrays were fabricated by our collaborators in the Brown group at Dalhousie University using a dice-and-fill approach, and more recently electrostrictive relaxor transducers have been created in the Zemp lab. The structure of the relaxor TOBE arrays is shown in Figure 2.10. As described in [63], the PMN-PT electrostrictive relaxor material was partially diced into 2D array elements and gaps were filled with an epoxy. This improves the radiation directivity as opposed to using the bulk material. Metal electrodes were sputtered and patterned with scratch dicing along the top and bottom, where the top and bottom electrode strips are orthogonal. The resulting piezoelectric transducers have a center frequency of 10 MHz.

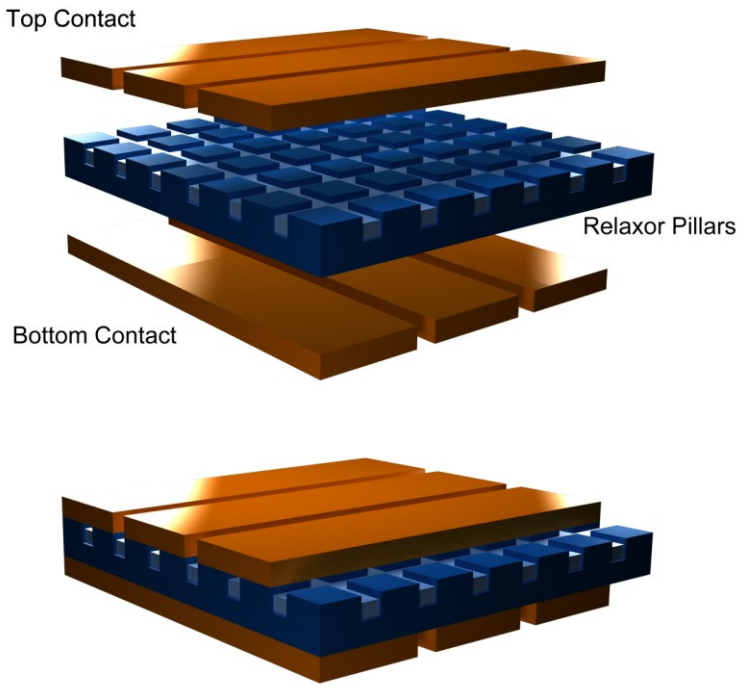

Figure 2.10: Diagram showing relaxor TOBE array structure. The relaxor surface consists of partially dices square posts with an epoxy filling.

Although relaxor transducers don't demonstrate many of the advantages of CMUTs, such as wider bandwidth and higher sensitivities, they are much simpler to fabricate, have linear sensitivity-DC bias relationships, and require smaller biases to operate. This makes them ideal for initial testing of TOBE imaging schemes.

Chapter 3: Design and Simulation of TOBE CMUT Arrays

Designing CMUT arrays is challenging because of the complex, nonlinear electro-mechanical behavior of CMUT membranes. Understanding how design changes at the device level, such as membrane thickness or radius, affect the overall operating characteristics is essential when designing arrays for specific applications and minimizing parasitic effects. A lumped model approach for simulating many CMUT membranes is summarized by Ceroici et al. in the published journal paper titled "*Large-Scale Nonlinear Lumped and Integrated Field Simulations of Top-Orthogonal-to-Bottom-Electrode CMUT Architectures*" [12] © 2017 IEEE which is presented here. Of the two authors, C. Ceroici constructed the simulation models and performed the experiments in this paper as well as wrote the manuscript. R. J. Zemp provided guidance and

advisement for the design and testing of these simulation models as well as assisted with writing the manuscript.

3.1 Introduction

Capacitive micromachined ultrasonic transducers (CMUTs) offer the possibility for large 2D imaging arrays [64]. In order to avoid the wiring constraints of a fully wired array, Top-Orthogonal-to-Bottom Electrode (TOBE) CMUT arrays have been proposed to reduce the number of channels in an NxN array to 2N [65]. TOBE arrays rely on the ability to dominantly actuate an individual element at the intersection of a row and column using bias sensitivity. In reality, both electrical and acoustic parasitic effects will limit this dominant element isolation and result in nearby elements actuating.

Recently, equivalent-circuit models have been developed which account for the nonlinear transduction mechanism as well as the interactions between membranes in the medium [2], [66], [67], [68]. This model has been demonstrated to accurately fit the membrane motion of fabricated CMUTs. In this paper, we adapt this model to simulate TOBE arrays and analyze the contributions of parasitic effects. The simulated dominant element isolation is then compared with a small TOBE CMUT array fabricated using a sacrificial release process.

3.2 Simulation Design

The simulations shown in this paper use the nonlinear equivalent circuit CMUT model described in [2]. The model schematic is shown in Figure 3.1 (a).

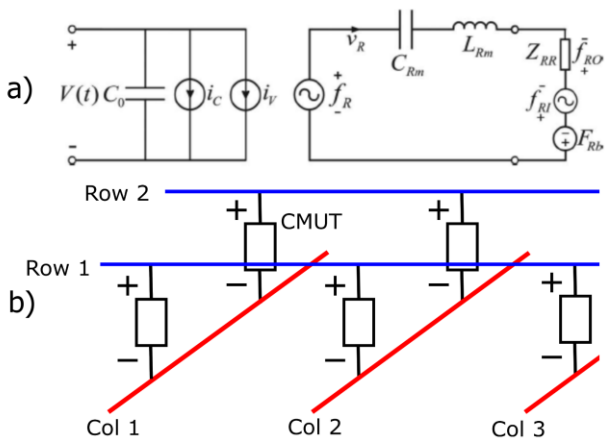

Figure 3.1: (a) Schematic of nonlinear CMUT equivalent circuit model from [2]. (b) Illustration of TOBE configuration for CMUTs.

The model accounts for the radiation impedance interaction between membranes with an impedance matrix. This is useful in simulating TOBE arrays, as it has a significant effect on dominant element isolation.

This SPICE-based simulation is evaluated in the Agilent Advanced Design Systems (ADS) software. Within ADS, a script is constructed to generate a netlist for a network of CMUTs in a TOBE configuration, illustrated in Figure 3.1 (b). These models are evaluated using harmonic balance (HB) simulations.

3.3 Results

3.3.1 Capacitive coupling along row connections

One possible limitation of large TOBE arrays is the capacitive effects of large numbers of inactive CMUTs connected along a row wire. This extra capacitance will shunt current from the row line,

diminishing the signal. Figure 3.2 shows the output current along the row of a TOBE array with 3x3 CMUTs per element for various array sizes. The array consists of circular CMUTs with 4 µm thick membranes consisting of SiN with a 40 µm radius and a 5 MHz center frequency immersed in oil. Each CMUT has a 250 nm gap, with an additional 100 nm layer of SiO2. These CMUTs have a simulated snapdown voltage of 130 V. A single element in the active row is excited by a 1.2 kPa pulse and the output current is measured along the row to simulate the TOBE array in receive mode. The capacitive coupling effects in this case are independent of which element is excited. The column of the active element is biased at 94 V while the other rows and columns are grounded.

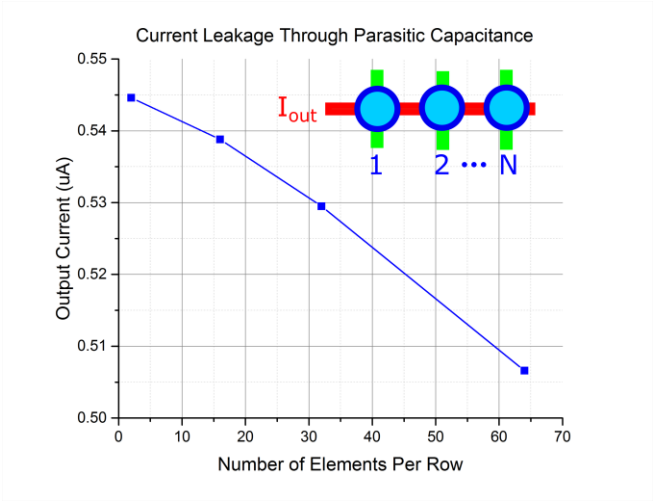

Figure 3.2: Simulated peak output current along a TOBE row connection. A single element along the row is excited by a 1.2 kPa acoustic pulse.

As the TOBE row size increases from 2 to 64 elements, the total output current decreases by 7%. As much larger (eg. 256 element) TOBE arrays are considered, the current shunting effect will have a greater parasitic effect on the arrays performance. This simulation demonstrates a potential design consideration for TOBE arrays, in particular, smaller TOBE sub-arrays mosaicked into a larger array may be advantageous to reduce parasitic losses.

3.3.2 Optimization of AC and DC driving voltages

Traditionally, active CMUT elements are biased as near to the snap down voltage as possible in order to maximize sensitivity. However, the biasing along a column in a TOBE array causes all membrane in the column to deflect, including those inactive elements. Just as the active element is more sensitive to a driving signal with a larger DC bias, nearby inactive elements along biased columns will be more sensitive to both acoustic and electrical coupling.

In order to characterize this effect, the DC voltage was varied in a simulated 6x6 TOBE array with an AC driving pulse signal along the active row, shown in Figure 3.3. The simulation uses 40- μm-radius membranes with a resonance frequency of 5 MHz and a membrane thickness of 4 μm. The CMUT gap height is 250 nm with a 100 nm SiO2 dielectric layer. The TOBE array elements have λ-pitch and are symmetrical. The dominant element isolation was calculated as the ratio of the average membrane velocity in the target element to the average membrane velocity of the nearest-neighbor, inactive elements.

The dominant element isolation ratio is significantly higher for lower VDC. However, it is important to note that the total output power of the array is much higher for larger VDC. This presents a clear trade-off between the ability to isolate individual elements and the total array output power.

The AC driving voltage amplitude also has an impact on the ability to isolate individual elements. As the membrane velocity increases, more energy is coupled to adjacent elements. Figure 3.4

shows the dominant element isolation in the same 6x6 TOBE array but with varying AC voltages along rows.

In order to further investigate the capacitive coupling effects, an ideal electrical isolation stage was added between each element and row connection, as illustrated in Figure 3.5 (right). This isolation stage is equivalent to an ideal op-amp with the negative input shorted to the output. Such an isolation stage could be accomplished by integrating electronics during the fabrication process.

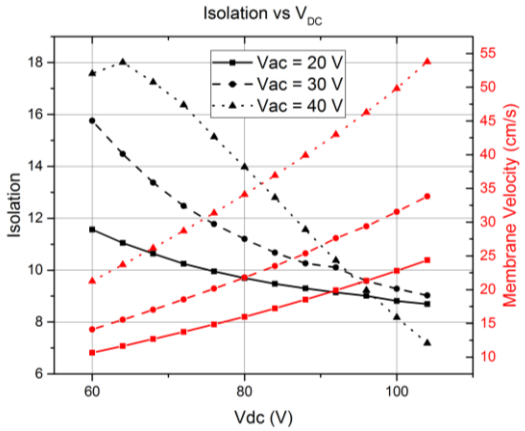

Figure 3.3: Simulated dominant element isolation for a 6x6 TOBE array versus the DC driving voltage. Simulations are shown for different AC driving voltages.

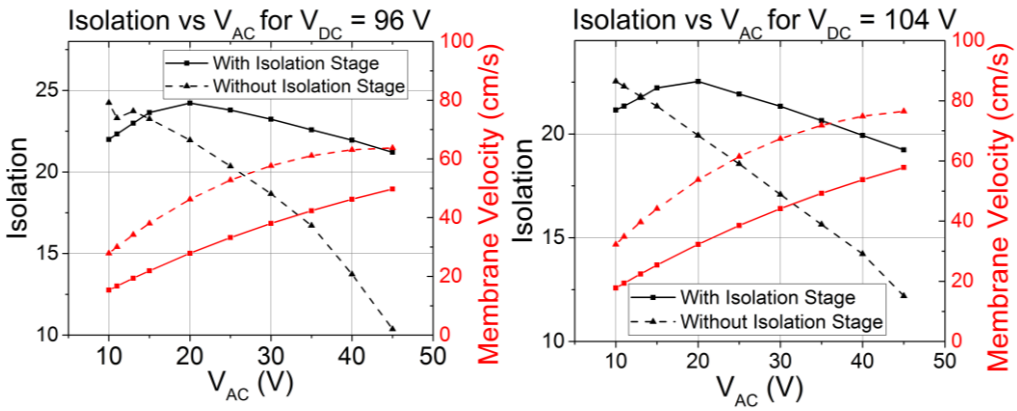

Figure 3.4: Simulated dominant element isolation for a 6x6 TOBE array versus the AC driving voltage. Simulations are shown for Vdc = 96 V (left) and 104 V (right). The effects of electrically isolated TOBE rows are also shown.

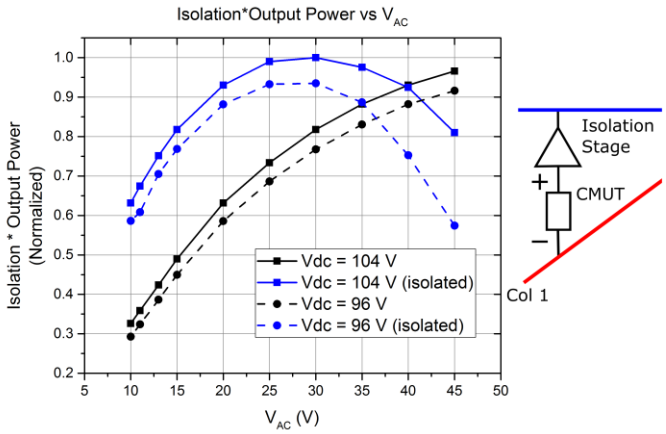

Figure 3.5: Simulated dominant element isolation for a 6x6 TOBE array versus the AC driving voltage (left) and illustration of the use of electrical isolation stages in the simulated TOBE arrays (right). Simulations are shown for Vdc = 104 V, 96 V and for electrically isolated TOBE rows.

These isolated arrays are also shown in Figure 3.4, where it can be seen that the maximum dominant element isolation is reached at VAC = 20 V. This suggests that a larger AC signal may not always be preferable when driving TOBE arrays, despite the larger output power. However, the membrane velocity of the isolated TOBE arrays at Vac= 45 V is 32% higher for VDC = 104 V and 28% higher for VDC = 96 V than the non-isolated arrays. To better understand the benefits of isolating TOBE row connections, we also consider the output power of the target element as well as the dominant element isolation as a figure of merit. This is shown in Figure 3.5 (left). With this definition for the overall performance, a clear maximum is achieved at VAC = 30 V for the isolated arrays. This point provides a balance between dominant element isolation and overall output power of the active elements.

3.3.3 Optimization of CMUT design parameters

In addition to the operating voltages of the array, the physical characteristics of CMUTs were also varied in order to investigate the effects on dominant element isolation. The CMUT membrane radius and gap were both varied and the isolation was measured as the ratio of the average velocity of the target element to adjacent elements. This is shown in Figure 3.6. A 90 ns transmit pulse was used in this case with a pulsing period large enough to neglect standing wave patterns in CMUT displacement. Average membrane velocity consistently decreased further away from the target element. In order to maintain a center frequency of 5 MHz as the membrane radius was changed, the membrane thickness was also varied. Also, in both cases, the bias voltage was varied to maintain a voltage of 80% of the snap down voltage.

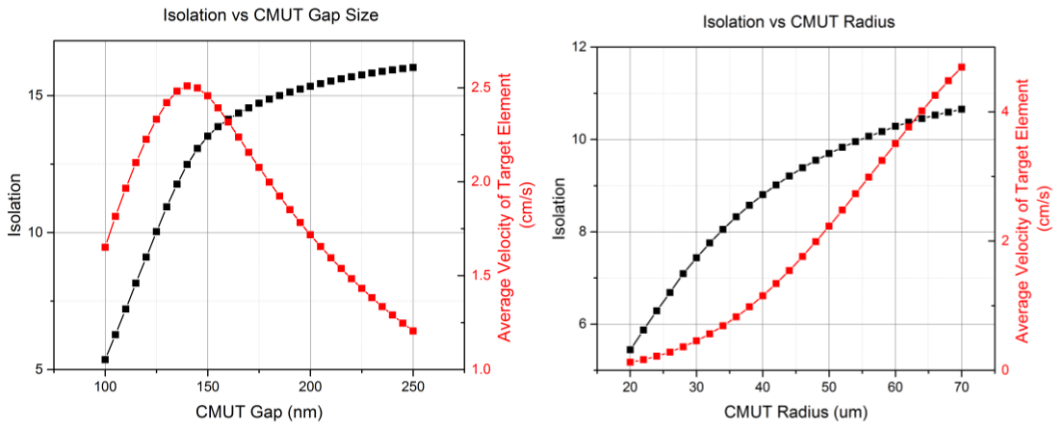

Figure 3.6: Simulated dominant element isolation for a 6x6 TOBE array with varying CMUT membrane radius (right) and gap height (left). The average velocity of the target element is also shown in red.

As the radius is increased, the simulated isolation increases. This is because larger radii require thicker membranes in order to maintain the center frequency which, in turn, require larger bias

voltages to maintain the bias deflection point. Note that, although a larger membrane radius will have smaller snapdown voltage, the increasing membrane thickness dominates the change in snapdown. Larger snapdown voltages provide better isolation across row connections. However, the upper bound of the radius is limited by the decreasing membrane thickness which at some point will make the design impractical.

As the CMUT gap height is changed, the membrane velocity reaches a peak at 150 nm. This can be explained by the constant AC signal applied as the gap height is changed. At each gap height value, the active CMUTs are biased at 80% of the snap down voltage. However, at larger gaps there is a larger voltage swing between the bias point and the snap down voltage, allowing for larger AC signals. Conversely, smaller gap heights allow for smaller voltage swings. The 20V AC signal makes best use of the voltage swing for the 150 nm gap height. The parasitic behavior of adjacent CMUTs is also strongly affected by the gap height. As the gap decreases, so does the snap down voltage. The unbiased CMUT elements along the same row as the active element therefore receives an AC signal larger relative to the snap down voltage as the gap decreases, decreasing the isolation.

3.3.4 Field II Simulations

The simulated CMUT array behavior in ADS was also integrated with the Field II acoustic field simulator to predict the arrays imaging performance [69]. Of particular interest was the effect of channel crosstalk in the TOBE array. To investigate this, a 32x5 TOBE array was simulated in ADS with a 100 ns, 20V transmit pulse, and the pressure output of each CMUT was used to simulate the acoustic pressure fields. This is shown in Figure 3.7. Only the center of the 5 columns is biased while the others are grounded. Transmit pulses are sent along the 32 rows with the

appropriate delays for focusing at 10 mm from the array. This results in an f-number of 1.4. The unbiased columns on either side of the biased one provide insight into the effects of acoustic impedance in TOBE arrays. For comparison, a 32x1 TOBE array with only a single column is also simulated. To compare with the ideal case, a Field II simulation was conducted of the same array but without considering the circuit-level or mutual acoustic impedance effects.

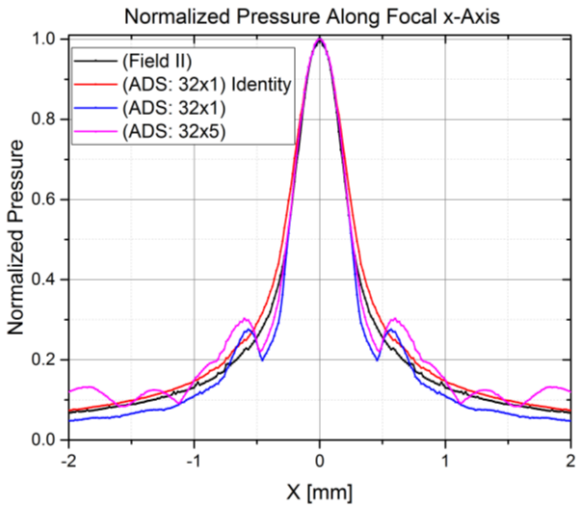

Figure 3.7: Simulated lateral resolution of a 32x5 TOBE array. Simulations using only Field II (black) as well as including the circuit level simulation of ADS with Field II (blue, red, pink) are shown. The blue line represents a 32x1 TOBE array, and the red a 32x1 TOBE array with a identity acoustic impedance matrix to examine the resolution neglecting the acoustic crosstalk between rows.

The Field II simulation of the array without any circuit-level component produced a full width at half max (FWHM) lateral resolution of 0.52 mm. The 32x5 and 32x1 TOBE arrays with both Field II and ADS components gave lateral resolutions of 0.45 mm and 0.5 mm, respectively. The existence of side lobes is likely due to the acoustic crosstalk between elements since the side lobes are not present in the case where acoustic crosstalk is disabled (using an identity matrix for the acoustic impedance). Although the simulated array which included the acoustic crosstalk effects

(the 32x5 array) had a smaller resolution, the side lobes were 1.6x larger than without acoustic crosstalk (32x1). This suggests that the presence of acoustic crosstalk across a TOBE array could increase the overall imaging clutter and degrade contrast-to-noise.

3.3.5 Comparison with measurements

To verify the simulation results, the dominant element isolation simulations were compared with a 5x5 TOBE CMUT array fabricated using a sacrificial release process described in [64], [70]. The array has 2x2 CMUTs per element consisting of 115 µm membranes with a thickness of 1 µm. The measurements were made using a Microsystem Analyzer MSA-500 laser vibrometer and were conducted in air. An 8 MHz AC voltage was used across the center row and a 100 V bias voltage was applied across the central column. Other rows and columns were grounded. The measured normalized displacement and the simulated displacement a shown in Figure 3.8.

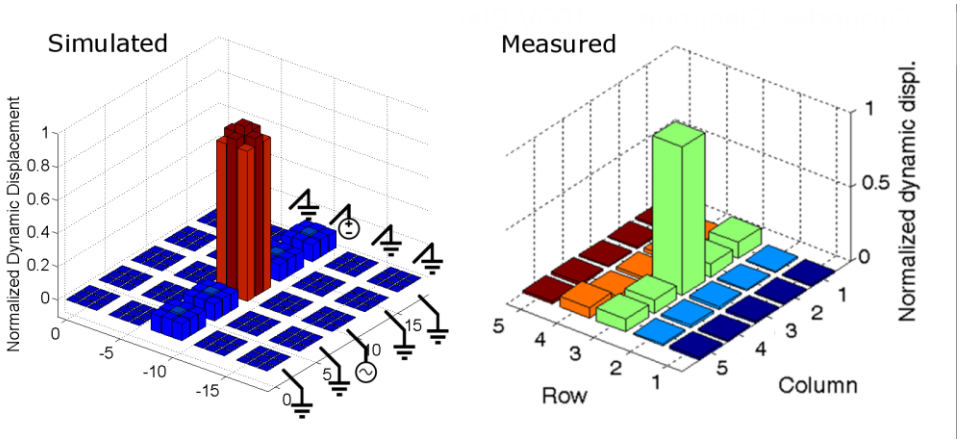

Figure 3.8: Comparison between measured (right) and simulated (left) normalized displacement of a 5x5 TOBE array in air.

A nearest-neighbor crosstalk was measured to be 19.2 dB, while the simulated crosstalk is found to be 20.1 dB. This shows that the parasitic effects predicted by the model manifest themselves in real-world devices.

3.4 Conclusion

An equivalent circuit CMUT model was used to simulate TOBE arrays of varying parameters. The impact of parasitic effects was investigated, and an optimization analysis was conducted with regards to the AC and DC driving voltages with the goal of maximizing the dominant element isolation. In addition, the effects of different CMUT radii and gap lengths on isolation was simulated. The studies presented here could be used as a framework for designing efficient TOBE arrays in the future. The use of electrical isolation stages was investigated by introducing buffer stages in between TOBE elements and rows. It was found that these arrays provide a better balance of dominant element isolation and output power.

The ADS simulations were integrated with the Field II acoustic field simulator to look at the effects of acoustic crosstalk on the lateral imaging resolution.

The simulation results of parasitic effects were compared with laser vibrometry measurements of a CMUT array. The measured crosstalk was found to be 20.1 dB while the simulated crosstalk was 19.2 dB. This suggests that the parasitic effects observed in simulations accurately model the physical systems.

Chapter 4: TOBE FORCES Imaging Scheme - Simulations

Although TOBE arrays allow for all elements in the array to transmit and receive simultaneously, the constraint of only having access to rows and columns places limitations on how the array can be controlled. In the journal paper "*Fast Orthogonal Row-Column Electronic Scanning (FORCES) with Top Orthogonal to Bottom Electrode (TOBE) Arrays*" [15] © 2017 IEEE, an imaging methodology is presented which uses coded bias patterns to provide substantially improved image quality than previous approaches. This publication, which presents simulation-only work, is shown here. Of the authors for this paper, C. Ceroici designed and carried out the simulations shown as

well as helped develop the FORCES imaging scheme and wrote the manuscript. T. Harrison assisted with code development and help develop other TOBE imaging schemes mentioned in the paper and in some cases, used for comparison. R. J. Zemp helped develop the FORCES imaging scheme and advised the work of the other authors.

4.1 Introduction

While 3D ultrasound imaging offers significant promise for a wide range of clinical applications, clinicians do not always prefer to use it, in part because image quality is often inferior to high-quality B-scan imaging using linear or phased-array transducers. It is essential that future 3D ultrasound systems overcome the technical challenges limiting B-scan imaging performance. One major challenge is the wiring congestion of fully-wired high-density 2D arrays as the channel number increases. A fully wired N×N channel 2D array with N^2 elements would require the same number of channel connections which would quickly become impractical for large arrays or for invasive probes where cable and probe sizes must be small. Explososcan 3D imaging methods use sparse multiplexed schemes to operate a 2D array with limited channel count [5], as illustrated in Figure 4.1 (a). Owing to limited-aperture transmit sub-arrays, only weak transmit focusing is possible reducing resolution and signal-to-noise. Matrix probes also offer integrated microbeamformers with analog-to-digital converters behind each element [3]. Such Matrix probes can be bulky and may require active cooling. They also make image-quality trade-offs to image quickly.

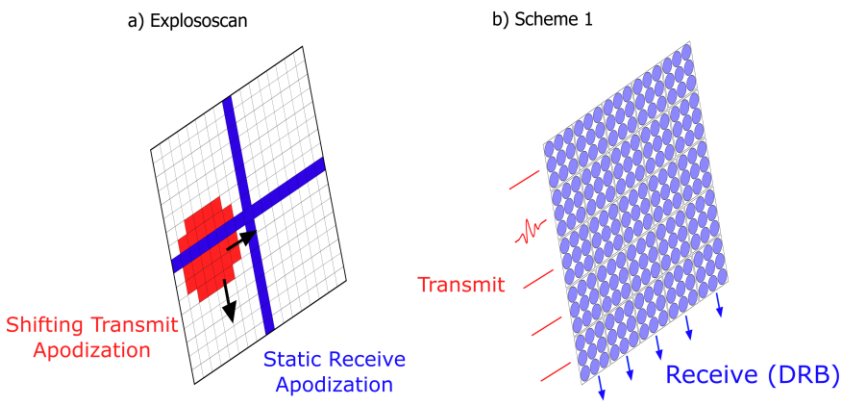

Figure 4.1: Diagrams of (a) Explososcan and (b) Scheme 1 imaging schemes. Explososcan involves a shifting transmit aperture with a static receive apodization. DRB: Dynamic Receive Beamforming. Explososcan uses a sparse multiplexed wiring scheme while Scheme 1 uses a TOBE wiring scheme.

Top-Orthogonal-to-Bottom Electrode (TOBE) arrays have been proposed as an alternative method of wiring 2D arrays. We have recently fabricated capacitive micromachined ultrasonic transducers (CMUTs) with a TOBE architecture [65]. We have demonstrated that individual elements can be dominantly actuated by applying a bias along the desired column electrode and transmitting or receiving a signal along the orthogonal row connection. In this case the 2D array can be fully controlled using only 2N channel connections. Dominant element sensitivity is only possible in such schemes when using bias-sensitive arrays such as TOBE CMUT arrays or potentially bias sensitive piezoelectric arrays [71], [72], [51], [7]. The use of TOBE architectures in CMUT array designs creates a new range of possibilities for large-scale 3D whole-organ imaging. However, one major obstacle for TOBE array technology is the imaging scheme used to acquire images. In order to be versatile enough to compete with linear arrays or matrix probes, it is essential that 2D imaging arrays be capable of acquiring high-quality B-scans with a high frame-rate in addition to having 3D imaging capabilities. This is the challenge tackled in the present paper.

One imaging scheme initially proposed for TOBE arrays is sometimes referred to as row-column-imaging [65], [73] or rectilinear imaging, originally proposed by Lockwood [8] and further discussed by Yen et al. [71]. This imaging scheme, illustrated in Figure 4.1 (b), involves transmitting along rows and receiving along all columns. Either a focused transmit signal can be used across all rows or one row transmits at a time. We consider the latter case, which we will refer to as Scheme 1, where the array is able to focus elevationally with retrospective transmit focusing using synthetic aperture beamforming [74], [75]. On receive, column signals are focused in the azimuthal direction using dynamic receive beamforming. This imaging scheme is therefore capable of only one-way focusing in both the azimuthal and elevational directions during 3D imaging. Due to the lack of two-way focusing, the sidelobe levels of Scheme 1 are greater than a linear array of the same size. A second imaging scheme, which we will refer to as Scheme 2, and which is described in detail in [65] involves signals transmitted and received along row electrodes allowing for two-way focusing in the elevational direction. The bias along the columns is stepped across the array to allow for one-way focusing in the azimuthal direction using retrospective synthetic aperture beamforming. In this case, since only one column is active in each transmit event, the signal-to-noise ratio (SNR) of the array suffers. Additionally, one major drawback is that N^2 imaging events are necessary not just for generating 3D images but also for a single two-way focused B-scan.

In this paper, we propose a new imaging scheme for bias-sensitive TOBE arrays: Fast Orthogonal Row-Column Electronic-Scanning (FORCES). This imaging scheme provides resolution and sidelobe advantages over Scheme 1 and two-way-focused B-scan frame rate advantages over Scheme 2. After describing the imaging scheme, we will compare the simulated imaging

performance of a FORCES TOBE array with Scheme 1 as well as with an Explososcan array with an equivalent number of transmit and receive channels. Although this paper does not present experimental validation, comparative simulations of FORCES with other imaging schemes illustrates the benefits in imaging speed and quality.

4.2 Proposed Imaging Scheme

In the FORCES imaging scheme, focused pulses are transmitted along rows to allow for fixed-cylindrical elevational focusing. Transmit signals are encoded by biasing columns with aperture-encoded patterns for increased SNR, shown in Figure 4.2. The biasing sequences are obtained from a Hadamard Matrix or S-Matrix.

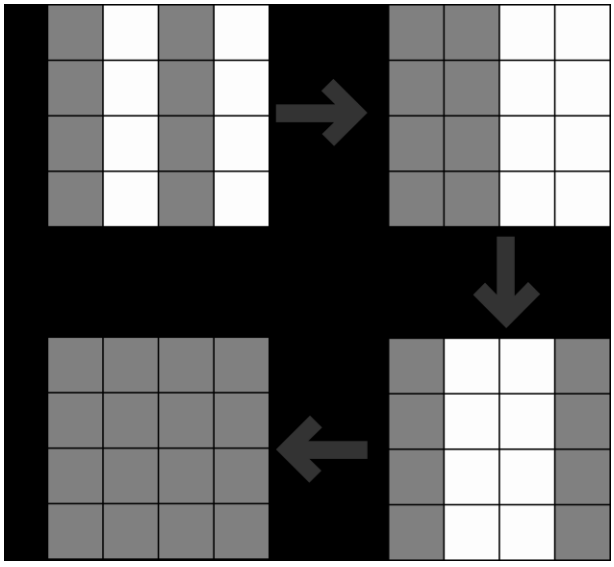

Figure 4.2: Illustration of transmit column bias sequence for a 4x4 TOBE array. Gray represents a positive bias and white represents a negative bias. Orthogonal biasing vectors are determined from the Hadamard matrix. If an S-matrix is used, the negative biases will become zero-biases.

We recently introduced S-matrix aperture coding for linear arrays, which has been shown to significantly improve the SNR over synthetic aperture imaging [56], [76]. Rather than activating

a single column in each imaging event, a coded sequence of elements are activated in a pattern selected from a Hadamard Matrix or S-Matrix. An S-matrix is obtained from a Hadamard Matrix by replacing -1 values with zeros and truncating the first row and column. By having multiple columns active in each imaging event, the array is capable of greater transmit power, allowing for higher SNR. The received signals are then unmixed using the inverse of the S-Matrix to obtain the equivalent receive signals to that of an imaging scheme with single columns active during transmit, though with a higher SNR.

In the TOBE FORCES imaging scheme, we use Hadamard sequences to bias columns of TOBE arrays as shown in Figure 4.2. Signals are transmitted along rows but received along columns, decoupled from DC biases. The advantage of the S-sequence or Hadamard encoding is two-fold. One is that we achieve SNR improvements. Perhaps more importantly, however, columns will only have appreciable sensitivity to echoes when they are biased. Hadamard biasing would allow all columns to be read out for each transmit event. S-Sequence biasing would allow half of the columns to be read out with the unbiased columns having no sensitivity. In contrast, biasing one column at a time would allow for only one column to be read out.

The column biasing pattern and de-mixing scheme allows for azimuthal synthetic aperture transmit beamforming in addition to azimuthal dynamic receive focusing. This scheme is limited to a single elevational transmit focus per transmit event, as illustrated in Figure 4.3. Multiple transmit focal zones are used to improve the depth-of-field in elevation. The two-way active focusing in the xz-plane perpendicular to the array means the FORCES imaging scheme can acquire higher quality B-scan images than Scheme 1 and with comparable image quality to a linear array as will be demonstrated.

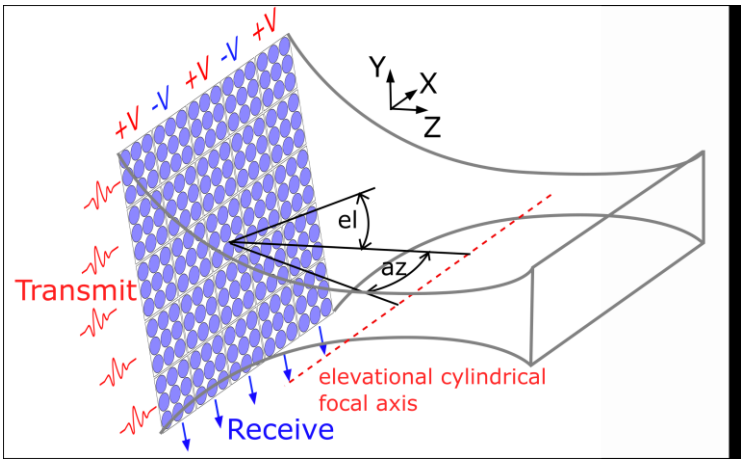

Figure 4.3: Schematic of proposed FORCES TOBE imaging scheme. Transmitted delayed pulses along rows enables a cylindrical elevation focus. Signals are received from columns and beamformed. az: azimuthal, el: elevational directions.

In contrast to Scheme 1 and Scheme 2, the FORCES imaging scheme is capable of obtaining a B-scan with two-way-focused azimuthal resolution using only N transmit events. This number can be further reduced by binning the column biases at the expense of some azimuthal resolution or sidelobe levels. As will be shown later, the FORCES imaging scheme is capable of generating B-scans with comparable imaging quality to a linear array with the same channel count and with the same number of transmit events but with improved elevational focusing owing to a larger elevational aperture. Extended depth-of-field 3D imaging can then be performed by obtaining additional B-scans at different elevational foci by adjusting the delays of transmit pulses along rows. 2D imaging arrays using the FORCES imaging scheme could potentially replace linear arrays to provide similar functionality and performance but with the additional capability of electronically-scanned 3D imaging and the potential for tighter elevational focusing compared to linear arrays with limited element height and fixed acoustic lenses.

4.3 Methods

To demonstrate the potential of the proposed TOBE FORCES imaging technology, we performed Field II simulations [69]. We modelled 64×64 TOBE arrays with 110μm × 110μm elements having 5.8 μm kerfs and a center frequency of 6.67 MHz. This provides an array with λ/2 pitch which was implemented in Field II using the xdc_2d_array function. The array types simulated here have similar center frequencies to clinical probes such as L7-4. The small array size of 14mm×14mm could be suitable for applications such as surgical guidance or transesophageal operations. These are applications where matrix probes don't exist due to the cumbersome probe electronics. We binned columns in groups of 2 to reduce the number of transmit events. We simulated point targets and a scattering phantom and used 4 elevational transmit focal zones at 15 mm, 25 mm, 35 mm, and 45 mm depths. An image for each x-z B-scan was created for each elevational focus, and the B-scans were stitched together to form a single x-z B-scan using a Gaussian weighting function. To form a single x-z B-scan, delay times were calculated for each row and each y-z focal point to define the elevational slice. Column biasing was determined by the rows of a Hadamard or S-matrix. The received scattered signals were summed across each column. After 32 transmit events (each with a separate bias-encoding), we decoded using the inverse Hadamard Matrix to recover the synthetic aperture dataset. Synthetic transmit aperture imaging was accomplished using a beamforming toolkit developed by Nikolov [77].

Explososcan simulations were conducted over a 65×65 element array with identical element dimensions to the TOBE array. A 12×12 square apodization with the corners removed was used as the transmit aperture, resulting in 128 transmit channels which is equivalent to the TOBE array

simulations. A static cross-shaped apodization which spans the width and height of the array was used for receiving, having 129 receive channels.

4.4 Results

4.4.1 Linear array comparison

A 64×64 element array using the FORCES imaging scheme was compared with an equivalent 64 element linear array to investigate the ability of the FORCES imaging scheme to generate B-scan images. Both arrays are 14 mm wide, however the TOBE array has a height of 14 mm while the linear array has a height of 5 mm. This difference is to show a more practical linear array geometry with a wider depth of field. The linear array is translated in the elevational direction to obtain

elevational resolution, while the TOBE array uses electronic elevational focusing. The x-y and x-z-plane images from a point-scattering phantom 24 mm from the array are compared in Figure 4.4.

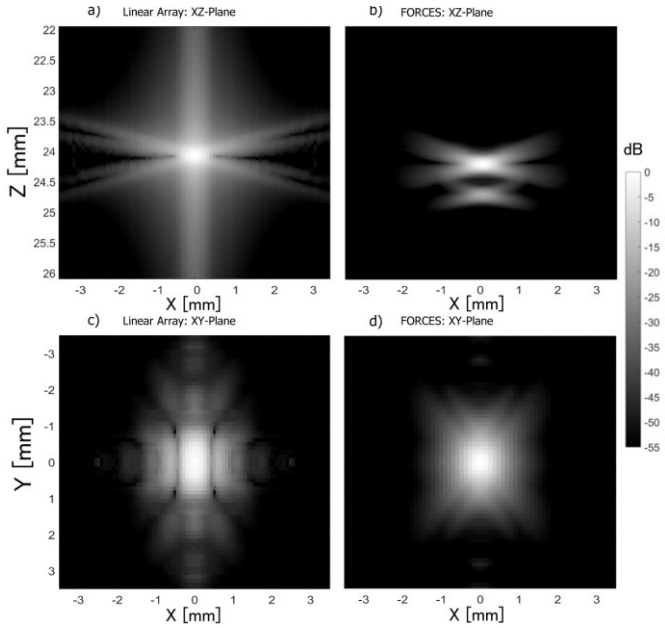

Figure 4.4: Simulated point target xz and xy-plane images. The point is 24 mm from the array. A 64 element linear array with a fixed elevational focus (a,c) is compared with a 64x64 element FORCES array (b,d).

The linear array showed an azimuthal resolution of 0.57 mm while the FORCES scheme had a azimuthal resolution of 0.52 mm. Since the arrays have the same number of horizontal elements, they have the same theoretical 3.46 ms B-scan acquisition time for an imaging depth of 4 cm. In this simulation, the linear array used 128 elevational steps and FORCES scheme used 128 elevational focal planes. Therefore, they also have the same volumetric acquisition time, 442.81 ms, assuming there is no additional delay from physically scanning the linear array. The elevational resolution of the FORCES scheme is 0.61mm compared to 1.09mm for the linear array. This is due to the large aperture and electronic steering capabilities of the TOBE array.

4.4.2 FORCES Bias Pattern Column Bin Sizes

While using the FORCES imaging scheme, column biases can be combined into bins to increase the imaging speed of the array at the cost of image quality. Increasing the bin size from 1 to 2 will decrease the total number of transmit events by a factor of 2, reducing the total acquisition time by half. Simulations were conducted with a point scattering phantom 24 mm from the array to determine the effects of the bias bin size on the image quality. Figure 4.5 shows the xz-plane images obtained using a variety of bin sizes as well as the amplitudes of the point spread function sidelobes, which signify artifacts and diminished resolution in the acquired image. It was found that only after increasing the bin size from 4 to 8 was a 15 dB increase in sidelobe amplitude observed. Using bin sizes of 2 and 4 showed negligible increases in sidelobe amplitude.

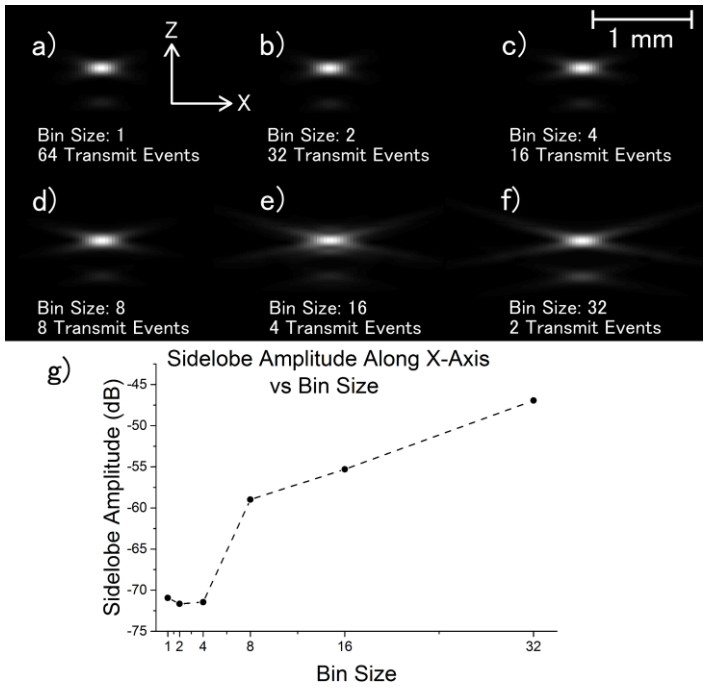

Figure 4.5: Comparison of bias bin sizes versus sidelobe amplitude for a 64x64 element array with the FORCES imaging scheme for a point scattering phantom 24 mm from the array. Images are shown in the xz-plane.

4.4.3 Comparison with Other 3D Imaging Schemes

The FORCES imaging scheme was compared to Scheme 1 and Explososcan in both point phantom and cyst phantom simulations. Simulated point phantom images are compared in different imaging planes in Figure 4.6. Point-spread functions along the x and z-axis are compared in Figure 4.7. The azimuthal resolution of the Explososcan, Scheme 1 and FORCES imaging schemes is 1.13 mm, 0.68 mm and 0.52 mm, respectively, with present parameters. Although the azimuthal resolution of Scheme 1 and FORCES is similar, the FORCES sidelobes are 25 dB smaller.

The additional peaks seen in Figure 4.7 (a) with Scheme 1 and FORCES are due to edge waves of the transducer and may be mitigated with apodization at the expense of slightly wider lateral resolution.

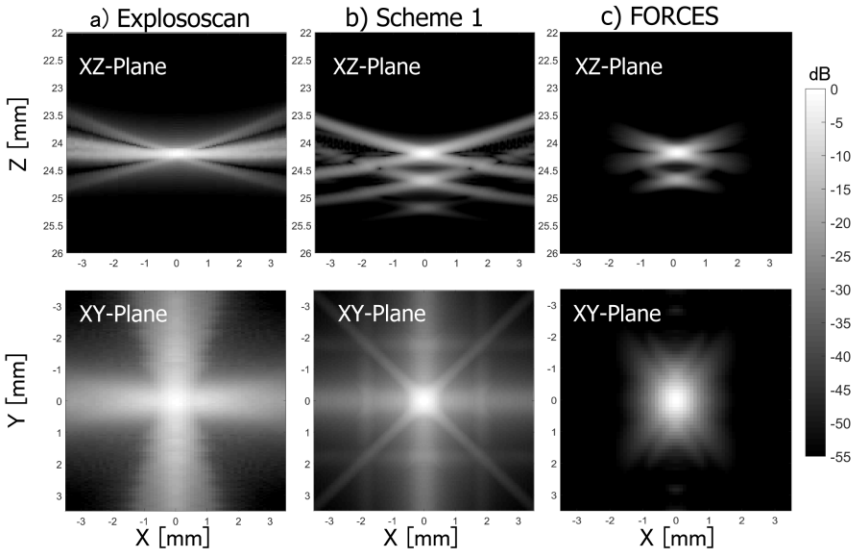

Figure 4.6: Scattering point phantom simulations for a phantom 24 mm from the array. Images care compared for the FORCES imaging scheme and Scheme 1 in the XZ and XY imaging planes. The image colors are mapped on a log-scale.

For the images in Figure 4.6, 128 B-scan slices were taken to resolve the point-scatter phantom in the y-axis. Scheme 1 lacks an active transmit focus, allowing for faster 3D imaging at the cost of image quality. With Gaussian random noise applied during the simulation, the SNR of Explososcan, Scheme 1 and FORCES was found to be 28.3 dB, 50.6 dB, and 54.2 dB, respectfully. The low SNR of Explososcan can be explained by the fact that only a limited number of elements are active during each transmit event.

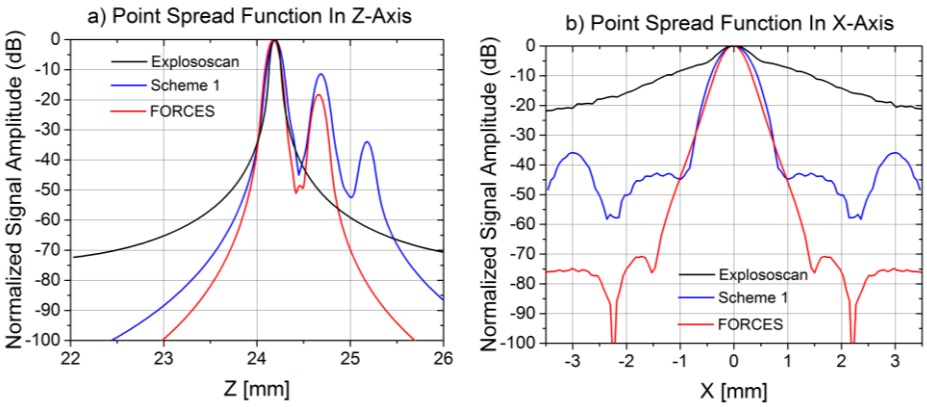

Figure 4.7: Point spread functions in the Z (a) and X (b) axis for a point phantom simulation. Results are compared for the FORCES imaging scheme and Scheme 1

The FORCES simulations shown in Figure 4.6 used bin size of 2. For a 4 cm imaging depth, this results in a theoretical total B-scan acquisition time of 1.73 ms or a total volumetric acquisition time of 221.41 ms. Scheme 1 requires only N transmits for both a B-scan and C-scan, and therefore has a theoretical total acquisition time for both of 3.46 ms. The Explososcan scheme had a transmit aperture which was translated both horizontally and vertically across the array 54 times each. In this case, the total B-scan acquisition time is 2.92 ms and 157.62 ms for a volumetric scan. Results are summarized in Table II.

Table II: Comparison of Simulated Imaging Speed and Quality for a Volumetric Scan Using a 64×64 Element Array with Different Imaging Schemes

Imaging Scheme	Acquisition Time (ms)	Azimuthal Resolution	Sidelobe Amplitude
Explososcan	157.62	1.13 mm	-13 dB
Scheme 1	3.46	0.68 mm	-44 dB
FORCES	221.41	0.52 mm	-74 dB

The technique of sectioning multiple elevational imaging planes was demonstrated in a simulation of point phantom-targets, spherical hyper-echoic targets, and spherical cysts of various sizes, shown in Figure 4.8. Two image planes are shown at y = 0 mm and y = 1 mm. In these cases, 4 different depth-focal-zone images were stitched together to increase the overall image depth-of-field. Each image plane consists of multiple elevational steering angles for each focal depth. Clearly, as the image plane is steered across the cyst phantoms, the cyst visibility decreases, and the wire targets are no longer visible.

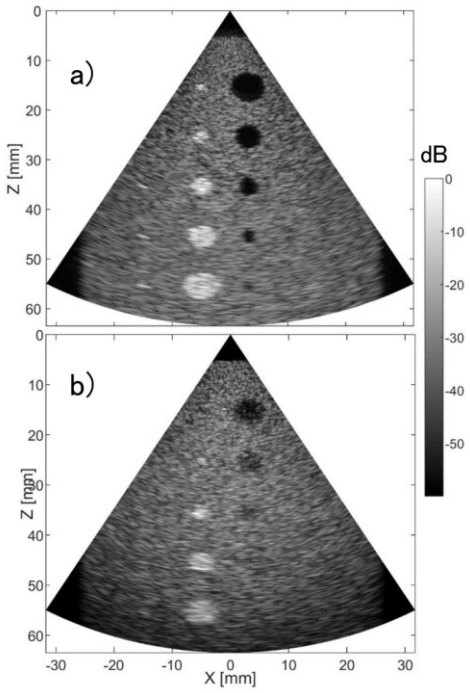

Figure 4.8: Scattering phantom simulated image using FORCES TOBE imaging scheme. (a) y=0 imaging-plane. (b) y=1 mm imaging plane.

These encouraging results could form the basis of more advanced 3D imaging capabilities. By electronically switching the imaging scheme from row-transmit, column-receive to column-transmit, row-receive, (effectively rotating the array by 90º) an additional B-scan can quickly be obtained in the perpendicular yz-imaging plane. This means that FORCES can be used for fast cross-sectional imaging, as shown in Figure 4.9 compared with similar images acquired with Scheme 1 and Explososcan.

From these cross-sectional images of a 3 mm radius cyst the contrast-to-speckle ratio, defined as:

$$\mathrm{CSR} = \frac{\mu_{\mathrm{in}} - \mu_{\mathrm{out}}}{\sqrt{\sigma_{\mathrm{in}}^2 - \sigma_{\mathrm{out}}^2}} \qquad 4.1$$

where μ is the mean signal and σ is the standard deviation of the signal, was found to be -8.98 for Explososcan, -11.26 for Scheme 1, and -29.42 for FORCES.

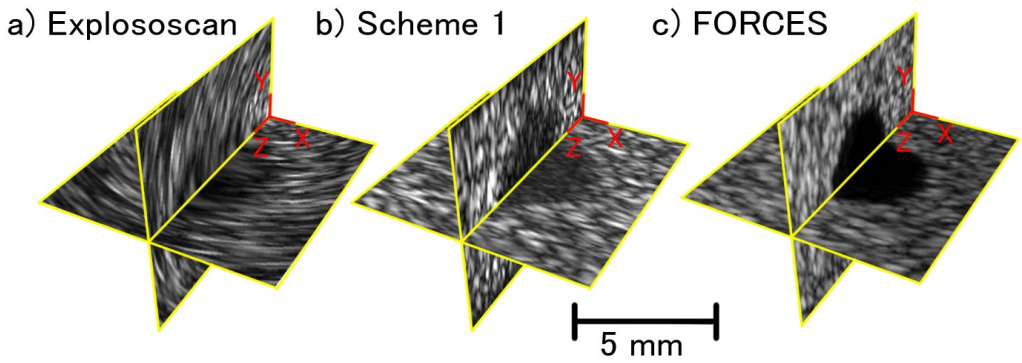

Figure 4.9: Simulation of cyst scattering phantom imaged with a 64x64 element array with Explososcan (a), Scheme 1 (b) and FORCES (c) imaging schemes. With the FORCES imaging scheme, both xz- and yz-plane images are obtained by switching the imaging scheme from row-transmit, column-receive to column-transmit, row-receive. Scheme 1 needs to acquire a full 3D image scan in order to produce the cross-section.

4.5 Discussion

In the proposed FORCES TOBE imaging scheme, a B-scan can be formed with good two-way focused in-plane azimuthal resolution, and because each transmit event is accompanied by in-plane dynamic receive focusing, each transmit event can produce a low-resolution image. The imaging quality is comparable to an equivalent sized linear array and can obtain B-scan images at the same speed. The sum of multiple low-resolution images will yield a high-resolution image as per previous synthetic aperture imaging methods. To image more quickly, columns can be binned together to produce an effectively coarse transmit array. For example, a 64x64 array using a bin size of 2 would use a 32x32 Hadamard matrix where each '1' in the bias vector would represent two adjacent biased columns. This would sacrifice azimuthal transmit focusing quality, however, this can be compensated for with dynamic receive focusing. Elevational sectioning may suffer

unless multiple transmit focal zones are used. The FORCES image scheme also offers the possibility of generating high-speed cross-sectional images by electronically switching the transmit/receive directions. This may prove to be a faster alternative to full 3D imaging when the area of interest is constrained to a smaller region along the imaging axis of the array.

Our proposed TOBE FORCES imaging scheme is shown to have significant image-quality advantages over Scheme 1 and Explososcan. Although the present study is simulation-only, future work will require the practical implementation of bias sensitive TOBE arrays. CMUT arrays fabricated using wafer bonder or sacrificial release are being investigated [65]. Additionally, bias-sensitive piezoelectric transducers based on piezoelectric relaxers may also prove promising [78], [63].

The present study ignores electrical and acoustic crosstalk between array elements. Future work should study the impacts of these effects on TOBE FORCES imaging quality.

Because TOBE architectures require only row-column addressing, they offer promise in scaling to very large arrays which would otherwise be cost-prohibitive. The TOBE FORCES approach also has considerable promise for small-scale 3D imaging probes for invasive and surgical guidance applications where probe footprint and cable size must be minimized.

TOBE FORCES technology may also provide advantages over traditional linear array B-scan imaging due to the flexibility of electronic elevational focusing versus a fixed elevation focus. Future work will test these hypotheses and compare with previous imaging technologies including MATRIX probes which have significantly higher complexity and potentially cost.

4.6 Conclusions and Future Work

In summary, we have proposed a new imaging scheme which we call FORCES (Fast Orthogonal Row-Column Electronic Scanning). This FORCES TOBE imaging scheme promises B-scan image quality comparable to a linear array transducer but with the flexibility to perform electronic 3D scanning. Row- and column addressing can be switched, for example to transmit along columns and receive along rows to obtain fast y-z B-scans. By quickly switching imaging orientations one may acquire fast x-z and y-z orthogonal imaging planes. Alternatively, multiple B-scans can be scanned to form a volumetric 3D image. Work in progress is focusing on experimental realization of these imaging schemes with crossed electrode TOBE CMUT arrays and bias-sensitive piezoelectric row-column arrays.

Chapter 5: TOBE FORCES Imaging Scheme – Experimental Results

In this chapter, experimental results of the FORCES imaging scheme are shown. Comparisons are made both to a linear array and a common method of row-column 3D imaging which doesn't use bias encoding. The content of this chapter is from the journal paper "*Fast Orthogonal Row-Column Electronic Scanning (FORCES) Experiments and Comparisons*" [16] The contributions of the authors of this paper are described as follows: C. Ceroici helped develop the FORCES imaging scheme and imaging system design, carried out the experiments, and wrote the manuscript. B. Greenlay designed the interface PCB. R. J. Zemp supervised these previous two roles as well as helped develop the FORCES imaging scheme and write the manuscript. K. Latham and J. A. Brown constructed the relaxor arrays.

5.1 Introduction

Top-Orthogonal-to-Bottom Electrode (TOBE) arrays consist of bias-sensitive transducers with top electrodes connected along rows and bottom electrodes along columns. These arrays have been shown to have several advantages over fully connected 2D arrays such as substantially lower channel counts and improved signal-to-noise ratio (SNR) due to the ability to transmit and receive across entire 2D [7], [8], [73], [79], [72], [65], [71]. However, one major drawback of TOBE arrays using traditional imaging schemes is the inability to focus on transmit both elevationally and azimuthally, which is possible using fully connected 2D arrays such as matrix probes [3], [42] as well as with Explososcan [5], [6]. This is due to the fact that electronically delayed pulses can only be applied in either the elevational or azimuthal direction. The result is that B-scans obtained using TOBE arrays are often of poorer quality than equivalent linear arrays. However, this is also true for Explososcan, which uses limited transmit and receive apertures to beamform multiple lines per emission. While matrix probes can provide improved resolution over crossed-electrode arrays, they are limited in size due to the required number of channels.

We previously proposed a TOBE imaging scheme, Fast Orthogonal Row-Column Electronic Scanning (FORCES), which was shown in simulation to have nearly equivalent B-scan imaging performance to a linear array with an equivalent number of channels yet offers the flexibility for volumetric scanning [15]. In addition, FORCES was shown to have had superior imaging performance to that of an alternative TOBE imaging scheme, Scheme 1, and also to that of a commonly used fully-connected array imaging scheme, Explososcan.

In this paper we test the hypothesis that the proposed FORCES imaging scheme can be implemented with a bias-sensitive row-column relaxor array and be able to form high-quality 3D

ultrasound images with two-way focused 2D synthetic aperture imaging (SAI) performance superior to existing TOBE imaging schemes exhibiting one-way azimuthal focusing. Additionally, we hypothesize that the FORCES imaging scheme will exhibit comparable or improved elevational resolution to linear-array transducers while offering electronic scanning capabilities. We experimentally demonstrate the FORCES imaging scheme using a 2D array consisting of 64×64 electrostrictive relaxor transducers. Imaging experiments are conducted on wire phantoms as well as with rat hearts. Our approach emphasizes achieving high in-plane 2D image quality as this is a deficiency of many 3D systems.

Three different 3D imaging schemes are considered for comparison. These imaging schemes are illustrated in Figure 5.1. Since the linear array's pitch and element width differ from the relaxor array's, comparisons with the linear array are only made in the elevational imaging characteristics. Scheme 1, also referred to as pyramidal scanning, illustrated in Figure 5.1 (b), was originally proposed in [48]. This imaging scheme utilizes TOBE arrays by transmitting along rows and receiving along columns. Row-transmit focusing can be accomplished by using an electronically delayed set of pulses or using SAI. Groups of elements with a virtual point source can also be used for SAI. We will consider the former case, where delayed pulses are used to steer and focus the beam in order to have a more equivalent SNR to that of our proposed imaging scheme. Since Scheme 1 has no ability to focus azimuthally on transmit, B-scans obtained using this imaging scheme have substantially larger side-lobe levels compared with a linear array using both transmit and dynamic-receive focusing. In contrast, the FORCES imaging scheme provide two-way focusing in the azimuthal direction.

The FORCES imaging scheme, shown in Figure 5.1 (c), transmits an electronically focused beam across rows but applies a set of encoded bias patterns along receiving columns. These patterns are obtained from the rows of a Hadamard matrix. Once the dataset is obtained using all of the encoded bias patterns, the dataset can then be decoded by multiplying the dataset by the inverse of the

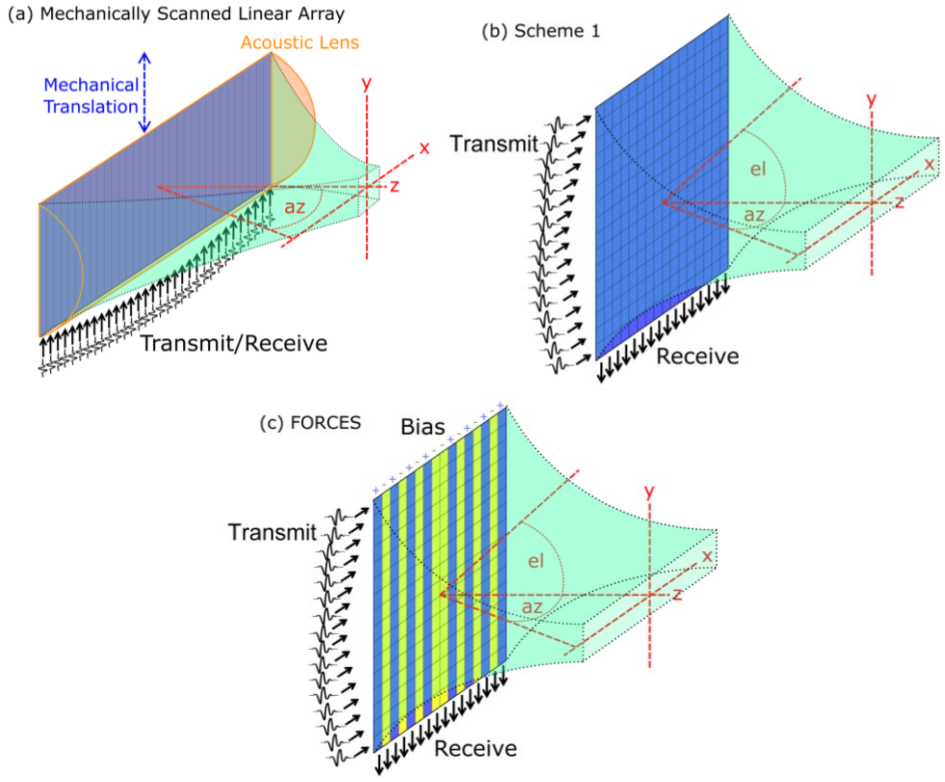

Figure 5.1: Illustration of three different 3D ultrasound imaging schemes. (a) Mechanically-scanned linear array, (b) Scheme 1 TOBE array, and (c) FORCES TOBE array.

Hadamard matrix [80]. The end result is a dataset equivalent to a form of 1D SAI where one column transmits at a time except the SNR is significantly improved due to the entire array being used for transmitting and receiving. The FORCES imaging scheme offers best-possible in-plane resolution because it offers full SAI capabilities. Elevational focusing is electronically adjustable and can be optimized for desired target depths.

5.2 Methods

Experiments are conducted on a 64×64-element TOBE array and a 192-element linear array. To match the linear array and TOBE array experiments as close as possible, the channel counts on the linear array are limited to an equivalent number of channels in one case, and an equivalent aperture size in another. To compare our proposed 3D imaging scheme (FORCES) with pyramidal scanning (Scheme 1) we keep all array and channel parameters the same, use the same transmit voltage and bias voltage levels, as well as include an averaged Scheme 1 case with an equivalent number of transmit events. Since the array characteristic of the linear array are not identical to that of the relaxor array, 2D imaging performance comparisons are not made between them, only elevational resolution is considered.

5.2.1 Electrostrictive Relaxor Array

The TOBE array used in these experiments consists of a PMN-PT electrostrictive relaxor material which was developed into a 1-3 composite 10-MHz transducer using a dice-and-fill approach, shown in Figure 5.2 and described in [63], [81], [78]. The array consists of 64 columns and row connections (64×64 elements) with a 1 cm aperture size, a 153 μm pitch (λ-pitch) and a 30 μm kerf.

The array is glued and wirebonded to a PCB which is then connected to a Verasonics Experimental Ultrasound System (Verasonics, Inc., Kirkland, WA, USA) using a custom interface board containing preamplifiers and the bias switching electronics illustrated in Figure 5.3. The experiments are conducted in a water medium.

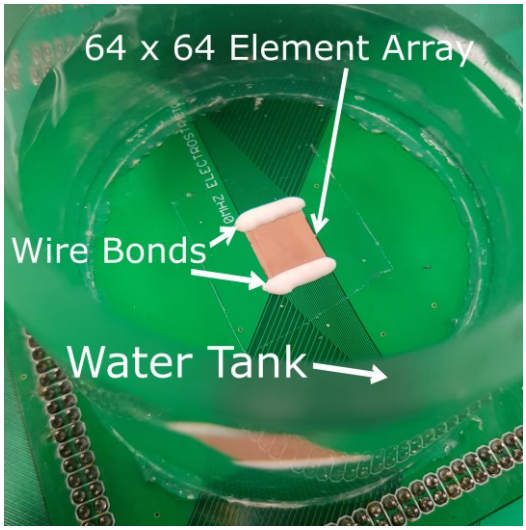

Figure 5.2: 64×64 element PMN-PT electrostrictive relaxor array mounted on a PCB.

5.2.2 Scheme 1 and FORCES

Two imaging schemes are implemented on the relaxor array: Scheme 1, and FORCES.

Scheme 1 involves transmitting delayed pulses to each row to create an elevational focus and receiving along columns while all elements are biased. In this case, only a single transmit is needed to acquire a B-scan. All column electrodes are biased with a positive voltage while all row electrodes are grounded. A modified version of Scheme 1, Scheme 1 averaged, was also

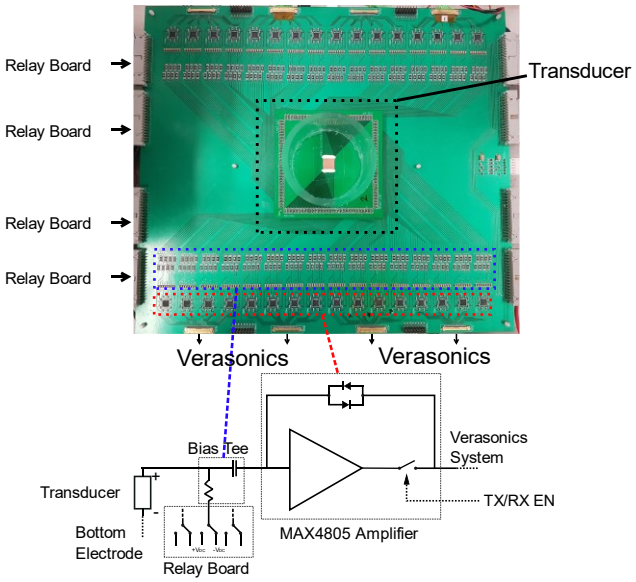

Figure 5.3: Photo of interface board and schematic of bias tee, high voltage relay board, and amplifier stage.

considered. In order to match the required number of acquisitions per B-scan of FORCES for a more fair SNR comparison, Scheme 1 averaged also uses 64 acquisitions but averages the reconstruction without any bias-encoding.

The FORCES imaging scheme, described earlier, also transmits along rows and receives along columns but uses a set of column Hadamard bias patterns to achieve two-way azimuthal focusing. Each column electrode has either a positive or negative bias depending on the Hadamard vector, while all row electrodes are grounded. Given that the reception is using long column elements which lack focus in the elevational direction, receive elevation sensitivity may be limited to points principally above the aperture. This technique relies on the ability to shift the phase of the transmitted waveform and received signals by 180˚ by reversing the applied bias. Typically, an N×N sized array will use N bias sequences, and therefore N transmit events. However, this can be reduced by binning adjacent elements and applying the same bias across both. For example, a 64×64 element array using a bin size of 2 would use a 32×32 Hadamard matrix for bias encoding with 32 transmit events. Since FORCES requires more transmits for each B-scan than Scheme 1, a variation of Scheme 1 where multiple acquisitions are averaged was also tested in order to compare an equivalent number transmit events.

For each B-scan acquisition, a single transmit steering angle is used to steer in the elevational direction. To improve the field of view, multiple focal depths can be obtained along this steering angle by adjusting the electronic focus and then compounding with a Gaussian-shaped weighting function. This offers greater flexibility than a linear array which will have a fixed elevational focus owing to a fixed acoustic lens.

For 3D acquisition, both Scheme 1 and FORCES used row-transmit focused electronic steering (in the elevational direction). 31 steering angles were used in a range from -15° to +15° with a step size of 1°. At a focal depth of 2 cm, this results in an elevational scanning distance of 10 mm. At

different steering angles, the focal depth was adjusted to maintain a constant z-distance from the array.

The driving waveform was a 42 V two-cycle sinusoidal pulse at 10 MHz. Bias control was conducted using a microcontroller connected with a set of relays switching between +55/-55 V biases. Although larger biases could be used for higher transmit power and sensitivity, these values were chosen to ensure long-term reliability of the array. For simplicity, we do not use any transmit or receive apodization for the FORCES and Scheme 1 imaging experiments. Inclusion of apodization may reduce side-lobe artifacts at the expense of lateral resolution and could be further investigated in future work

FORCES imaging sequences consisted of applying the appropriate Hadamard bias pattern to column channels, transmitting delayed pulses to row channels and repeating for all Hadamard patterns.

The FORCES images are reconstructed offline using a custom Hadamard decoding and synthetic-aperture delay-and-sum script, and the Scheme 1 images are reconstructed using a custom delay-and-sum script. All reconstructions are performed using a 36 MHz sample rate, the standard sampling rate for this probe on the Verasonics system, and 151 scanlines.

5.2.3 Linear array

For comparison, a Verasonics L12-5 ultrasound linear array probe is also used. This array has 192 elements with a 4.3 cm aperture size, and element height of 0.75 cm, and a fixed acoustic lens with an elevational focus at 2 cm.

With the L12-5 linear array, a plane-wave angle compounding imaging scheme is used with 64 angles (and 64 transmit events) from -18° to +18° with a steering angle step size of 0.5423°. The array is stepped elevationally to acquire 3D volumes using 31 steps with a step size of 0.3 mm. The same 42 V two-cycle sinusoidal 10 MHz pulse is used for these experiments. Plane-wave angle reconstructions are performed using the Verasonics system.

In order to make a more equivalent comparison, the linear array is restricted in active channel numbers. In one case, 64 elements are used, the same as the relaxor array. In the other case, 46 elements are used in order to obtain a similar aperture size, 10.3 mm, to the relaxor array aperture size, 9.79 mm.

5.2.4 Wire phantom experiments

Imaging experiments are conducted on two 17.8 μm-diameter aluminum wire phantoms at varying distances from the array. The wires are attached to the sides of the tank in a cross pattern where the first wire was oriented parallel to the array columns and the second wire perpendicular. The azimuthal and elevational resolution of the two TOBE array imaging schemes are calculated, and only the elevational resolution are calculated for the linear array.

5.2.5 Rat heart experiments

Imaging experiments are also conducted on a rat heart acquired from a sacrificed 250g Sprague Dawley rat using Scheme 1, Scheme 1 averaged and FORCES with a column bin size of 1 and 2. The heart is suspended approximately 1 cm above the relaxor array for these experiments.

5.3 Results

5.3.1 Array characterization

The array is first characterized in a variety of ways to ensure that it is capable of implementing the FORCES imaging scheme. Of particular interest are the bias-sensitivity characteristics of the transducers. This is tested by measuring the transmitted pressures and received signals with varying DC biases. Figure 5.4 shows (a) the received signal amplitude using an external single-element 10 MHz transducer with a 40 V transmit pulse, (b) the output pressure of the relaxor array measured with a hydrophone, and (c) the measured phase of the relaxor array output pressure waveform.

The receive sensitivity and transmit pressure shows a linear relationship with the DC bias and is approximately symmetrical with positive and negative biases. Most importantly, Figure 5.4 (c) shows that the transmit pressure undergoes a 180º phase-shift when a negative bias is applied. This is an essential feature for Hadamard-encoded bias encoding [80].

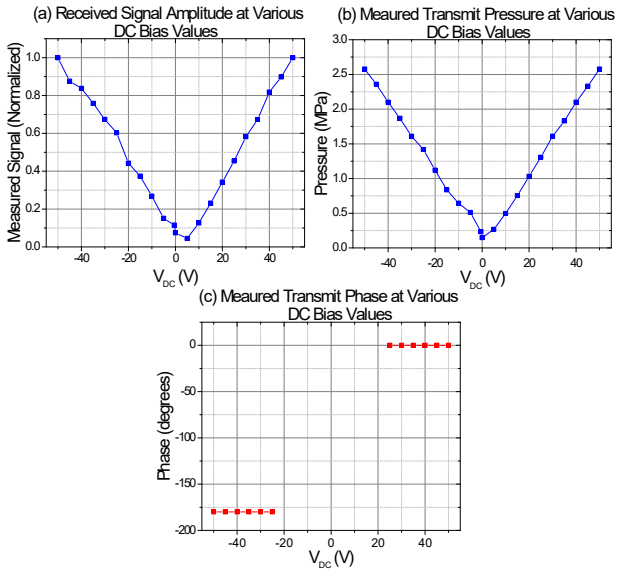

Figure 5.4: (a) Average received signal amplitude across the array columns using an external single-element 10 MHz transducer at 2 cm from the array, (b) pressure output of the array at the 2 cm focus measured using a hydrophone, and (c) the phase of the hydrophone-measured pressure waveforms from (b). Measurements are made across a range of positive and negative DC biases. Phase measurements could not be made reliably at |VDC| < 20 V due to low SNR.

A feature of the FORCES and Scheme 1 imaging schemes is the ability to section B-scans at a variety of elevational angles. This relies on row-transmit electronic focusing, as illustrated in Figure 5.1. This is demonstrated in Figure 5.5 which shows hydrophone measurements conducted in a plane parallel to the array at the focal distance at approximately 2 cm while all elements have a 50 V bias. This experiment is done (a) without steering and (b) with a 5º transmit steering angle. A surface pressure of 0.31 MPa is measured for the array giving a focal gain of 4.1 for the case in Figure 5.5 (a) and 3.9 for Figure 5.5 (b). Figure 5.5 (c) shows the pressure measurement along X = 0 mm from which the full width at half maximum (FWHM) measured pressure intensity along the elevational axis was calculated to be 0.29 mm and 0.30 mm for 0° and 5° steering angles, respectively.

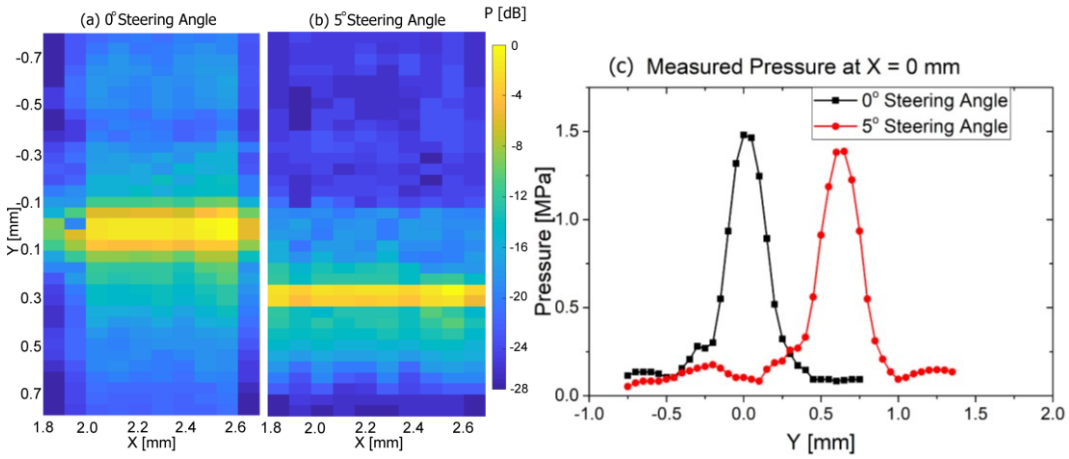

Figure 5.5: Hydrophone pressure measurements in the plane parallel to the array. Electronic focus is applied (a) without a steering angle and (b) with a 5º steering angle. The pressure is normalized to the maximum received pressure, 1.48 MPa. Pressure measurement of both cases are shown at a depth near 2 cm and in (c) along X = 0 mm.

5.3.2 Wire phantom experiments

Figure 5.7 shows the point spread function of the two wires using (a,c,e) the FORCES imaging scheme and (b,d,f) Scheme 1 with 64 frame averaging. The azimuthal and axial point spread functions of these experiments are shown in Figure 5.6 (a) and (b), respectively, and the elevational point spread functions are shown in (c) along with the linear array 64 plane-wave compounding angles elevational point spread functions for comparison.

The experiment is also conducted using a bin size of 2 with the FORCES imaging scheme. This Scheme 1 averaging scheme acquires 64 B-scans without any bias patterns and then averages the reconstruction. To compare the imaging performance of the imaging schemes, the resolution and SNR were calculated with the phantom at three different depths.

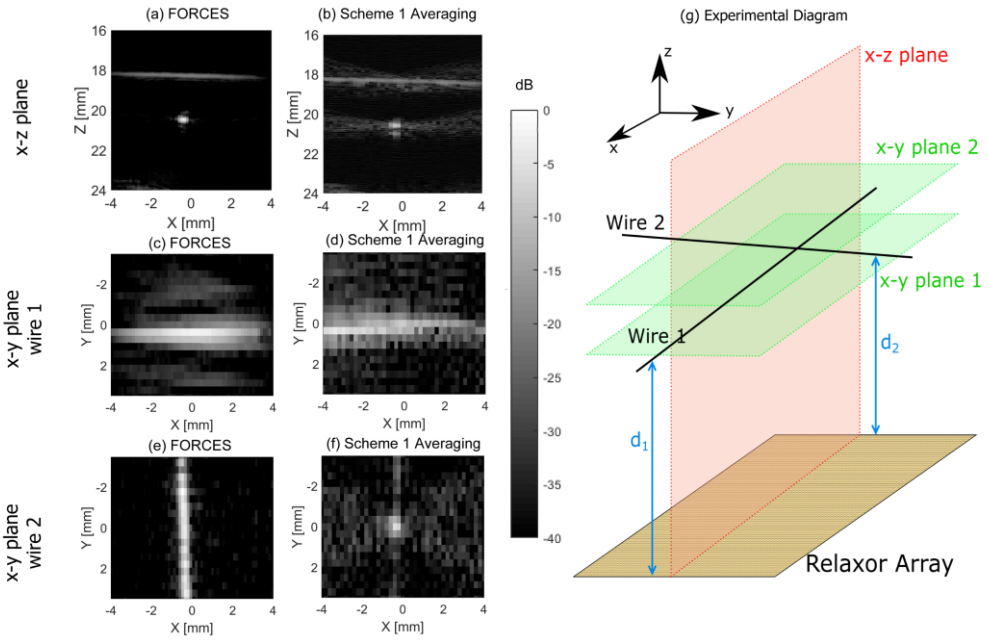

Figure 5.7: Wire phantom images using (a,c,e) the FORCES imaging scheme and (b,d,f) Scheme 1 with 64 frame averaging. The top row shows ZX-plane images of the two wires at d1 = 18 and d2 = 20 mm with y = 0 mm, the second row shows YX-plane images of the first wire and the third column shows YX-plane images of the second wire. Two 17.8 µm-diameter wires are used at 18 and 20 mm from the array. The nearest wire is oriented perpendicular to the array columns while the second wire is oriented parallel as illustrated in (g).

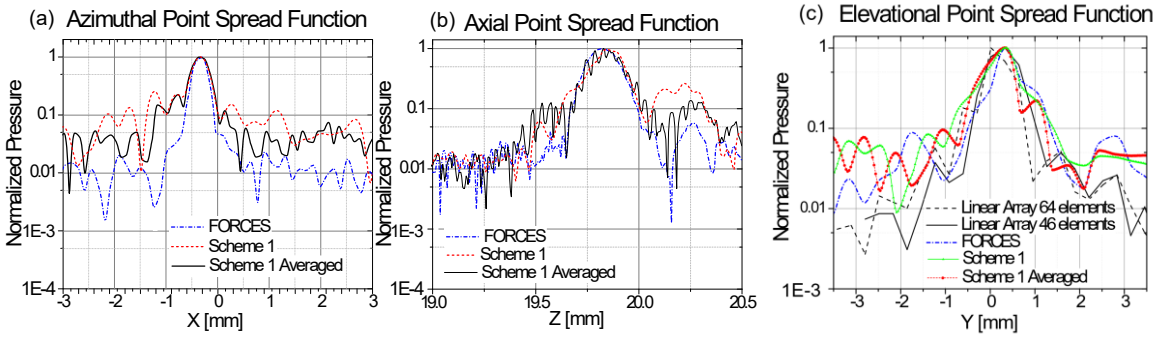

Figure 5.6: (a) Azimuthal and (b) Axial point spread functions of 17.8 µm diameter wire for the two crossed electrode imaging schemes and (c) elevational point spread functions for the crossed electrode and linear array imaging schemes.

Table IV shows the calculated resolution and SNR of the FORCES, Scheme 1 and Scheme 1 averaged imaging schemes with the first wire at a depth of 20 mm. Table III and Table V show the imaging performance of the phantoms at 15 mm and 25 mm, respectively. Table VI shows a comparison of the elevational resolution at the three phantom depths for the crossed-electrode imaging schemes as well as with the linear array plane-wave compounding imaging schemes. Resolution measurements are made with a ±0.04 mm error. The SNR is calculated as the ratio of the largest scattered signal in the second wire to the standard deviation of the signal in a volume outside both wires.

Figure 5.8 shows the axial and azimuthal resolution at different elevational points for the Scheme 1 and FORCES imaging schemes in the azimuthal and axial directions, as well as the linear array, 64-element plane-wave compounding imaging scheme in the elevational dimension. The animation in Figure 5.9 shows the reconstructed 3D image of the wire phantoms obtained using the FORCES imaging scheme with 31 elevational steering angles. Two different axial focal points are used at the axial locations of the first and last wires and then compounded in the reconstruction. In this case, a total of 128 transmit events were used for each B-scan plane.

Table III: Relaxor Array Wire Phantom Measurement Results with Phantom Depth at 1.5 cm

Imaging Scheme	# of Channels	# of Transmits per B-scan	Azimuthal Resolution (mm)	Axial Resolution (mm)	SNR (dB)
Scheme 1	64	1	0.45	0.32	31.8
Scheme 1 (averaged)	64	64	0.45	0.31	36.2
FORCES (Bin Size: 1)	64	64	0.34	0.31	39.5
FORCES (Bin Size: 2)	64	32	0.39	0.33	36.8

Table IV: Relaxor Array Wire Phantom Measurement Results with Phantom Depth at 2 cm

Imaging Scheme	# of Channels	# of Transmits per B-scan	Azimuthal Resolution (mm)	Axial Resolution (mm)	SNR (dB)
Scheme 1	64	1	0.42	0.17	33.3
Scheme 1 (averaged)	64	64	0.42	0.15	37.6
FORCES (Bin Size: 1)	64	64	0.31	0.17	41.7
FORCES (Bin Size: 2)	64	32	0.34	0.17	40.9

Table V: Relaxor Array Wire Phantom Measurement Results with Phantom Depth at 2.5 cm

Imaging Scheme	# of Channels	# of Transmits per B-scan	Azimuthal Resolution (mm)	Axial Resolution (mm)	SNR (dB)
Scheme 1	64	1	0.57	0.27	31.2
Scheme 1 (averaged)	64	64	0.57	0.27	32.2
FORCES (Bin Size: 1)	64	64	0.45	0.24	38.7
FORCES (Bin Size: 2)	64	32	0.48	0.24	38.0

Table VI: Wire Phantom Measurement Elevational Scanning Results

Transducer	Imaging Scheme	# of Channels	# of Transmits per B-scan	Aperture Width (mm)	Elevational Resolution at 1.5 cm (mm)	Elevational Resolution at 2.0 cm (mm)	Elevational Resolution at 2.5 cm (mm)
Relaxor Array	Scheme 1	64	1	9.79	0.61	0.47	0.67
Relaxor Array	Scheme 1 (averaged)	64	64	9.79	0.61	0.47	0.67
Relaxor Array	FORCES (Bin Size: 1)	64	64	9.79	0.54	0.46	0.54
Relaxor Array	FORCES (Bin Size: 2)	64	32	9.79	0.55	0.46	0.56
L12-5 Linear Array	64 Compound Plane-Wave	64	64	14.3	0.87	0.72	0.89
L12-5 Linear Array	64 Compound Plane-Wave	46	64	10.3	0.88	0.80	0.93

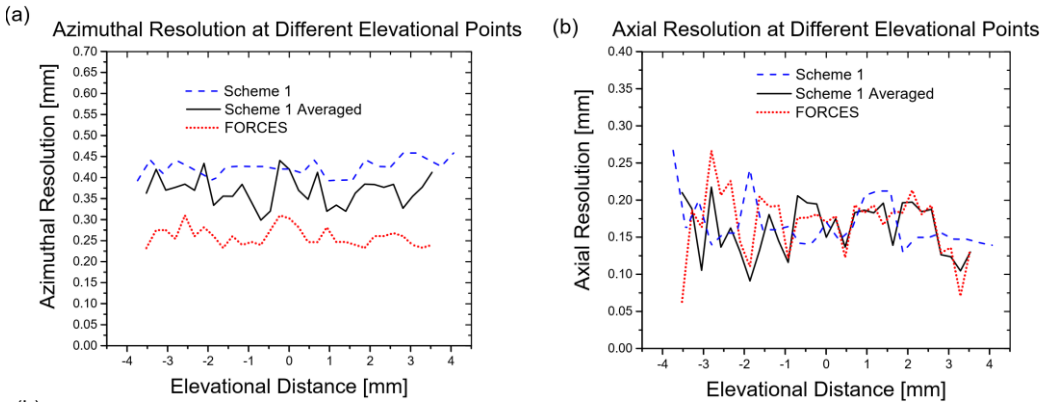

Figure 5.8: (a) Azimuthal and (b) axial resolution of a wire phantom at different elevational points for the three crossed-electrode imaging schemes: Scheme 1, Scheme 1 averaged, and FORCES. The phantom is located 20 mm from the array.

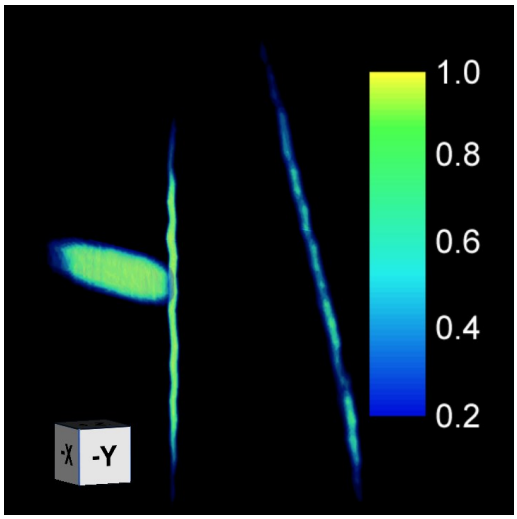

Figure 5.9: Reconstructed 3D data of three wires using the FORCES imaging scheme. The first two wires are perpendicular to one another while the third is diagonal at a 45˚ angle. 31 elevational steering angles are used with two axial focal depths. Video file of this animation is available at http://ieeexplore.ieee.org.

5.3.3 Rat heart experiments

Figure 5.10 shows a B-scan image using (a) Scheme 1, (b) Scheme 1 with 64 frame averaging, (c) FORCES with a bin size of 1, and (d) FORCES with a bin size of 2. The contrast-to-speckle ratio, defined as:

$$\mathrm{CSR} = \frac{\mu_{\mathrm{in}} - \mu_{\mathrm{out}}}{\sqrt{\sigma_{\mathrm{in}}^2 - \sigma_{\mathrm{out}}^2}} \qquad 5.1$$

where μ is the mean signal and σ is the standard deviation of the signal, was calculated based on the heart wall relative to the heart cavity as well as relative to the medium outside of the heart. The contrast was calculated as $(\mu_{in}-\mu_{out})/\mu_{out}$. In these cases, μ_{in} and σ_{in} refer to the area of interest, in this case the heart wall. These results are summarized in Table VII. B-scans of the rat heart at

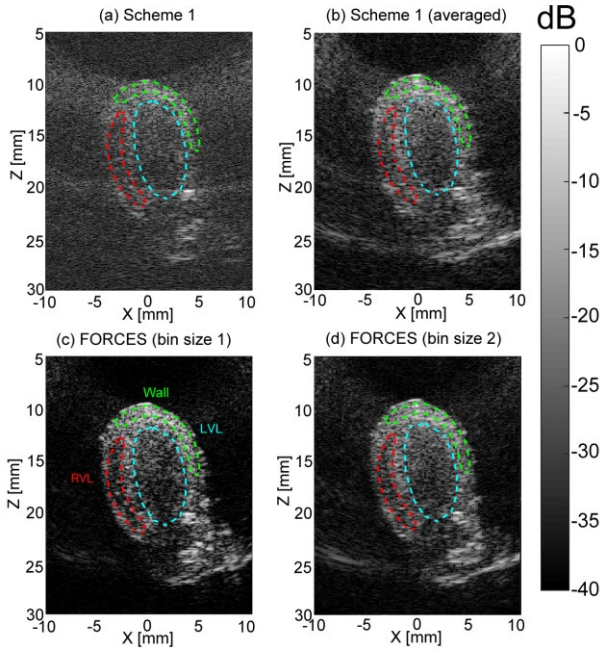

Figure 5.10: B-scan image of a rat heart using (a) Scheme 1, (b) Scheme 1 with 64 frame averaging, (c) FORCES with a bin size of 1, and (d) FORCES with a bin size of 2. The left ventricle (LVL), right ventricle (RVL) and heart wall area used for contrast and CSR calculations are highlighted in blue, red, and green respectively.

multiple elevations are shown in Figure 5.11 for FORCES and Scheme 1, along with a flythrough animation of the FORCES reconstruction with 31 elevational slices.

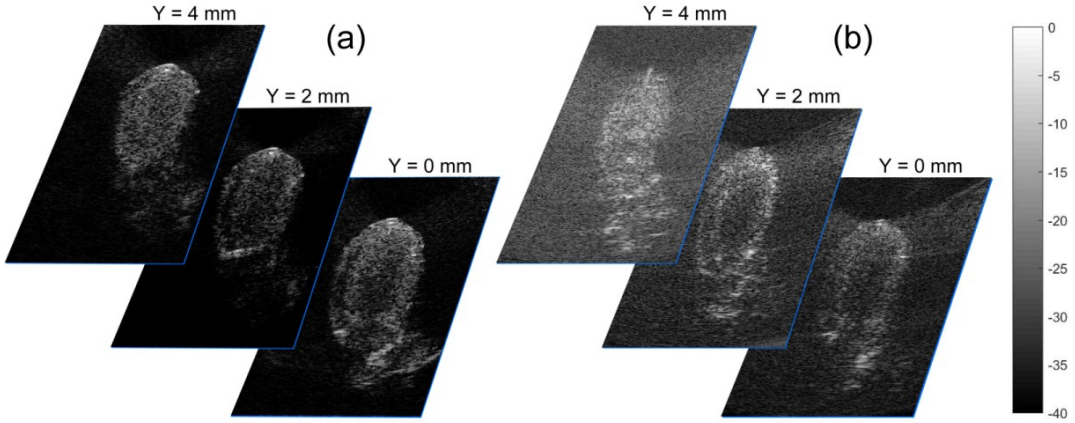

Figure 5.11: Comparison of rat heart B-Scans at multiple elevations using (a) FORCES with a bin size of 1 and (b) Scheme 1. A video file of a flythrough animation of the rat heart using FORCES imaging scheme with 31 elevational slices is available at http://ieeexplore.ieee.org.

Table VII: Rat Heart Imaging Performance

Imaging Scheme	Wall Relative to RVL		Wall Relative to LVL		Wall Relative to Medium	
	Contrast	CSR	Contrast	CSR	Contrast	CSR
Scheme 1 (no averaging)	0.27	0.22	0.23	0.19	0.34	0.29
Scheme 1 (averaged)	1.90	0.81	1.92	0.80	4.06	1.01
FORCES (bin size 1)	3.08	1.04	2.69	1.00	8.92	1.26
FORCES (bin size 2)	2.42	0.78	2.15	0.75	6.22	0.97

5.4 Discussion

The FORCES imaging scheme shows significant SNR and azimuthal resolution advantages over Scheme 1 which is to be expected since FORCES involves 64 acquisitions and Scheme 1 only a single acquisition. However, the comparison between FORCES and Scheme 1 averaged, where

FORCES demonstrates an improved azimuthal resolution and SNR, illustrates the two-way focusing advantages of FORCES.

The elevational resolution at multiple depths shows that the TOBE array schemes produced substantially improved elevational resolution compared to a linear array with fixed-elevation-focus acoustic lens and smaller elevational aperture (7.5mm for the linear array compared to 9.79 mm for the relaxor array), as expected. The TOBE array schemes discussed here achieve elevational resolution through the use of steered row-transmit beams enabling electronic focusing at different depths with multiple transmits. Thus, the TOBE FORCES technology may enable improvements in elevational slice thickness over an extended depth-of-focus compared to fixed-elevation-focus linear arrays. This is evident in Table IV, where for the linear array, elevational resolution degrades to 0.93 mm only 5 mm beyond the elevational focus, whereas FORCES with the electrostrictive relaxor array achieves 0.54mm elevation resolution at the same depth. FORCES demonstrates improved resolution and SNR when compared with Scheme 1, although FORCES requires 64 transmit events and Scheme 1 only a single transmit. However, the comparison with Scheme 1 averaged, which also uses 64 transmit events, highlights the utility of using coded column-biases to achieve two-way focusing due to the improved resolution and SNR.

The proposed FORCES imaging scheme offers excellent in-plane B-scan image quality but provides only one-way elevational focusing and may not be suitable for all 3D imaging applications where more isotropic resolution is required. Nevertheless, image quality improvements over previous row-column imaging schemes and mechanically scanned linear arrays may prove useful in a number of practical scenarios. The axial resolution of the TOBE imaging schemes possibly suffers from multiple edge wave responses due to the fact that element

heights cannot be reduced on receive since entire columns hold the same bias. In contrast, the fixed acoustic lens of the L12-5 transducer allows for both transmit and receive focusing in the elevational directions. It is possible to improve on this in the FORCES imaging scheme by switching the bias pattern from biased columns on transmit to biased rows on receive to allow for the height of the aperture to be reduced, improving axial resolution. However, this would require bias switching architecture which would allow for switching within a few microseconds, which could be considered in future work.

The present system is designed to provide first feasibility of the image quality enabled by the combination of the FORCES imaging scheme with bias-switchable TOBE arrays such as the current electrostrictive relaxor array. Because of the ms-switching times of the relay board, it is not meant to be a fast imaging system. Preliminary testing indicates that the material polarization can be switched with a few microseconds. This suggests that future developments may permit fast volumetric imaging. Although the imaging rate of the FORCES scheme is limited by the relay-based bias switching electronics, high-voltage solid-state switching integrate circuits such as HV2761 (Microchip Technology Inc., Chandler, Arizona, USA) are capable of switching biases in approximately 5 μs. Imaging at a 5 cm depth with a bin size of 2 and 31 elevational slices, the volumetric acquisition rate would be approximately 14.7 vol/sec with a 454 fps B-scan acquisition rate.[1]

Another row-column imaging scheme called Simultaneous Azimuthal and Fresnel-Elevational (SAFE) Compounding was recently proposed by Latham et al. [82]. SAFE compounding uses

[1] Since the publication of this paper, a preliminary solid-state bias switching PCB has been tested with the FORCES scheme to have a B-scan imaging rate of 43 ms with a volumetric imaging rate of approximately 1 vol/sec.

plane wave compounding for azimuthal focusing while using row-biasing to create Fresnel lenses for elevational focusing. In principle, SAFE compounding can achieve two-way focusing in both azimuth and elevation. However, given that FORCES can implement full synthetic aperture imaging in azimuth, achievable resolutions are finer with FORCES. Moreover, elevational resolution is less degraded when scanning off-center. When scanning near the edge of the array, SAFE compounding achieves a resolution of 0.39 mm in azimuth and 0.78 mm in elevation, when using the same array and system described here. In contrast, FORCES achieves a resolution of ~0.3 mm in azimuth and 0.46 in elevation.

5.5 Conclusion and Future Work

In summary, we have experimentally compared the imaging performance of Scheme 1, Scheme 1 averaged and FORCES. When investigating the elevational resolution, we also considered a mechanically translated L12-5 linear array at 10 MHz with 64 and 46 elements. The FORCES imaging schemed demonstrated significantly improved azimuthal resolution and SNR when compared with Scheme 1 and Scheme 1 averaged. In wire phantom experiments at a depth of 2 cm, the azimuthal resolution was found to be 0.42 mm, 0.42 mm, and 0.31 mm for Scheme 1, Scheme 1 averaged and FORCES respectively. The elevational resolution was found to be 0.47 mm, 0.47 mm, 0.46 mm and 0.72 mm for the Scheme 1, Scheme 1 averaged, FORCES and 64-element Linear array multi-angle plane-wave imaging, respectively.

Rat heart imaging experiments were also conducted with the three imaging schemes. The contrast of the heart wall relative to the RVL was calculated to be 3.08 for the FORCES imaging scheme with a column bin size of 1 and 1.90 for Scheme 1 averaged. This is likely due to the presence of two-way azimuthal focusing through bias-encoding when using FORCES. The FORCES scheme

also demonstrated improved contrast and CSR relative to the medium when compared with Scheme 1 averaged.

The advantages of the FORCES imaging scheme may outweigh any disadvantageous slight axial blurring. Moreover, the elevational and axial resolution of the FORCES imaging scheme could potentially be improved by switching the bias pattern between transmit and receive in order to limit the height of the receive aperture. Larger arrays could then be used with more elements to allow for improved azimuthal focusing and resolution without necessarily resulting in larger element heights.

In conclusion, the FORCES imaging scheme has been demonstrated experimentally with bias-sensitive crossed-electrode TOBE arrays. It offers two-way full synthetic aperture focusing in azimuth leading to high-quality B-scans and electronic 3D scanning capabilities which may prove to be competitive with more complex MATRIX probes with integrated beamforming electronics, and potentially for a fraction of the cost. Because this high image quality is achieved using only row- and column addressing and biasing without requiring addressing of individual elements, the presented approach may prove to be a key enabling platform technology for many future 3D ultrasound imaging systems. It may enable very large 2D arrays for whole organ imaging. Because of minimized channel count, it may also enable small endoscopic arrays for surgical guidance applications.

Chapter 6: TOBE 3D Photoacoustic Imaging

Photoacoustic imaging is unique in that is measures optical properties of tissue at greater depths than optical-only imaging techniques. From the perspective of TOBE arrays, photoacoustic imaging is also unique in that the array is not used for transmitting. This means that the array bias pattern can be selected without needing to consider the impact on the acoustic radiation pattern. This idea was used to develop a bias-encoding scheme which can acquire full 3D volumes rather than B-scan after each set of bias patterns. This is described in the journal paper "*3D Photoacoustic Imaging Using Hadamard-Bias Encoding with Crossed Electrode Relaxor Array*" [19] which is shown in this chapter. The contributions of this authors are as follows: C. Ceroici helped develop the imaging scheme described here, wrote the manuscript, as well as carried out the photoacoustic imaging experiments with the assistance of R. Chee and Q. Barber. B. Greenlay designed the interface PCB. The work of previously mentioned authors was supervised by R. J. Zemp who also

assisted with writing the manuscript and developing the imaging scheme. K. Latham constructed the relaxor array under the supervision of J. A. Brown.

6.1 Introduction

Photoacoustic imaging is the process of using acoustic waves generated from the absorption of electromagnetic energy to form images [28]. While ultrasonic imaging investigates mainly the mechanical properties of tissue, photoacoustic imaging allows for the probing of optical properties such as optical reporters [9], or oxygen saturation in blood vessels while allowing for deeper imaging depths than optical-only imaging [10].

Receiving photoacoustic signals on a 2D transducer array allows for the reconstruction of a 3D volume using dynamic receive beamforming. 3D photoacoustic imaging was performed using a clinical 2D matrix array in [83]. However, a major limitation in this approach is the size of a fully-connected 2D array. For example, an array with a size of 64×64 would have 4,096 transducer elements. This would require 4,096 receive channels which would become impractical due to wiring congestion as well as prohibitively expensive. Other approached to 3D photoacoustic imaging have included scanned linear arrays [11], ring array transducers [29], and sparse 2D arrays [30]. 3D photoacoustic imaging using optical etalons, such as that demonstrated in [25] and [26], allow for sensitive detection, but long readout times are required, etalon-uniformity problems have hampered parallel readouts, and these etalons are not designed as ultrasonic transmitters, precluding their use for co-registered ultrasound imaging. An alternative approach is using a cross-electrode or Top-Orthogonal-to-Bottom-Electrode (TOBE) wiring scheme [65]. In a TOBE array,

top transducer electrodes are all connected along columns while bottom connections are connected along rows. This allows for the addressing of elements in the array by transmitting/receiving along rows/columns with a greatly reduced channel count [8], [48]. A 64×64 TOBE array requires only 128 channels. In addition, bias sensitive transducers such as Capacitive Micromachined Ultrasound Transducers (CMUTs) or bias-sensitive piezoelectric relaxor arrays allow for additional types of operation by switching array biases. For example, the signal for a single element in a bias-sensitive 2D array can be obtained by biasing the corresponding column and receiving from the corresponding row. Unbiased elements will not receive signals and so will not contribute to the signals received at the connected row. Additionally, the polarity of the bias will dictate the polarity of the received signal.

By biasing a single column and then receiving along all rows, the signals for each respective biased element in the column can be obtained. By then stepping the biased column across the array, every element signal can be measured. This was demonstrated in [31] using a CMUT TOBE array, although using a mechanically scanned array rather than bias switching. This approach suffers from poor SNR since only a single column of elements is receiving at a given time.

In this Letter, we demonstrate a novel 3D photoacoustic imaging technique which utilizes bias encoding to allow for the entire TOBE array to receive signals providing a substantial improvement to SNR. We also introduce a novel crossed-electrode relaxor piezoelectric array for 3D photoacoustic imaging. This array permits not only bias-dependent amplitude sensitivity but also bias polarity-dependent phase sensitivity [81]. 3D acoustic imaging was demonstrated using this array in [16].

6.2 Methods

Rather than receive along a single biased column of elements j to obtain signals $x_{0j}(t), x_{1j}(t), \ldots\ x_{ij}(t)$, where i is the row number, all columns are biased using a scaled bias pattern chosen from the rows of a Hadamard matrix which is an invertible matrix consisting of ±1s. Each bias pattern (Hadamard matrix row vector) is applied to column biases and the row electrode information is measured providing the dataset $G(t)$. While Hadamard encoding has been widely used for encoded spectroscopy and patterned illumination-based optical and photoacoustic imaging [84] [85], it has not yet been applied for acoustic transducer encoding for photoacoustic applications.

$$G(t) = \begin{bmatrix} g_0^0(t) & g_1^0(t) \cdots & g_N^0(t) \\ g_0^1(t) & g_1^1(t) \cdots & g_N^1(t) \\ \vdots & \vdots & \vdots \\ g_0^B(t) & g_1^B(t) \cdots & g_N^B(t) \end{bmatrix} \tag{6.1}$$

N is the total number of rows while B is the number of bias patterns, equal to the number of rows in the Hadamard matrix. With a 64×64 element array, a 64×64 Hadamard matrix is used and therefor B is 64. Each measured signal $g_i^b(t)$ for row i and bias pattern b consists of the superimposed signals of all elements in row i, $x_{ij}(t)$, multiplied by the respective column bias pattern value $h_j(b)$ where j is the column index.

$$g_i^b(t) = x_{i0}(t)h_0(b) + \ldots\ x_{iN}(t)h_N(b) \tag{6.2}$$

In order to retrieve a dataset consisting of only the individual element signals X(t), the bias-encoded dataset G(t) is decoded by multiplying it with the inverted Hadamard matrix H.

$$X(t) = G(t)H^{-1} \tag{6.3}$$

The received element data in $X(t)$ can then be used to reconstruct a 3D image using dynamic receive beamforming, time-reversal, model-based reconstruction, or Fourier approaches. Hadamard bias-encoding offers a theoretical SNR improvement of $\sqrt{N}$ for an $N \times M$ size TOBE array where there are N elements read out per row.

Experiments were conducted using a 64×64 element relaxor array which was developed into a 1-3 composite 10-MHz transducer using a dice-and-fill approach described in [81]. The 9.79 mm × 9.79 mm array had a 123 µm element size with a 153 µm pitch (λ-pitch). Using an external 10 MHz single-element transducer calibrated with a HNP-0400 hydrophone, the noise-equivalent pressure as defined in [26] of a single element was found to be approximately 3 kPa. The experimental setup is shown in Figure 6.1. The array was wire bonded to a PCB which was then interfaced to a bias tee connecting to a relay-based bias switching board and receive preamplifiers. Analog-to-digital conversion was performed using a Verasonics Vantage experimental ultrasound system. A glass tank was attached to the PCB with two 17.8 µm-diameter aluminum wire phantoms in a cross shape with a 1 mm spacing at the intersection and a 12.8 mm spacing between the first

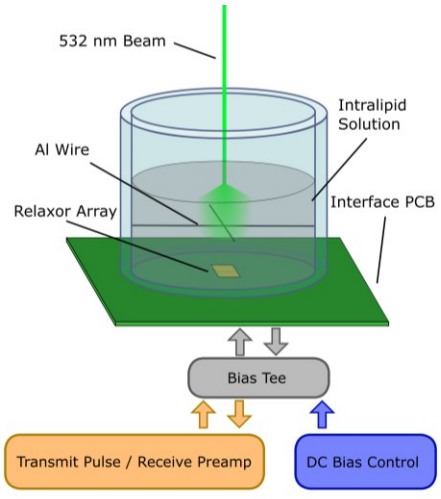

Figure 6.1: Diagram of experimental setup.

wire and the array. The tank was filled with a 1% intralipid solution to simulate tissue scattering. The intralipid surface was 9.5 mm above the first wire. A Nd:YAG laser 532 nm pulsed beam with a 20 mJ/cm^2 fluence was directed towards the wire intersection at the intralipid surface.

Imaging sequences were conducted using a single biased column stepped across the array and acquiring signals across all rows (equivalent to replacing H in Eq. 6.3 with the identity matrix) as well as using Hadamard-encoded bias patterns. Bias patterns were programmed using a microcontroller which switched an array of relays between ±50 V for each column electrode. Images were then reconstructed by using delay-and-sum beamforming in 3D. Both identity-matrix and Hadamard-matrix encoding schemes require the same number of transmits, and therefore have an equivalent acquisition speed. The reconstruction of Hadamard-encoded data requires the additional matrix-multiplication operation in equation 6.3 but this computation is negligible when compared to the delay-and-sum calculations. Currently the imaging speed is limited by the 10 Hz laser repetition rate as well as the relay-based switching electronics, however this could be improved by lasers with faster switching rates as well as solid-state-based switching electronics. Ultimately, the laser repetition rate will limit the volumetric acquisition speed.

6.3 Results

Figure 6.2 shows the XZ-plane reconstructed images for the case without bias-encoding (alternatively, identity matrix encoding), and with Hadamard-bias-encoding. In these reconstructions, the azimuthal direction is defined as perpendicular to the receiving rows, and the elevational resolution as perpendicular to the columns. The full-width-at-half-maximum (FWHM)

azimuthal resolution of the identity-bias sequence reconstruction was 487 µm while the Hadamard encoded bias sequence reconstruction was 311 µm.

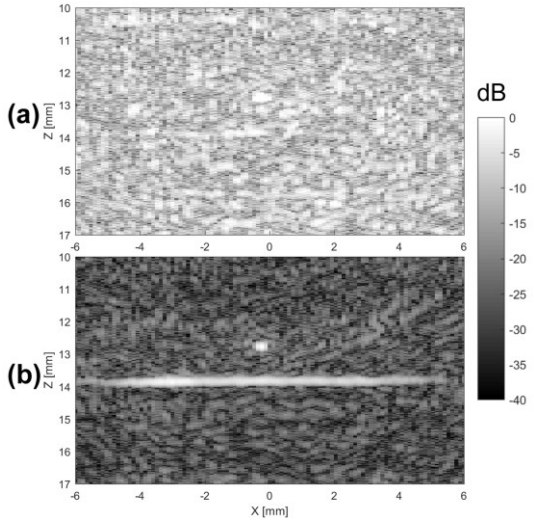

Figure 6.2: Experimental XZ-plane photoacoustic reconstruction of two crossed wires in optical scattering medium using (a) identity matrix bias sequence (no encoding) and (b) Hadamard bias sequence encoding.

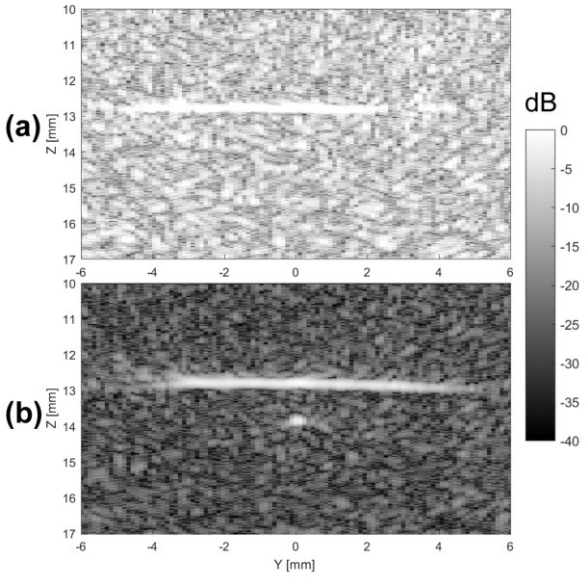

Figure 6.3: Experimental YZ-plane photoacoustic reconstruction of two crossed wires in optical scattering medium using (a) identity matrix bias sequence (no encoding) and (b) Hadamard bias sequence encoding.

Figure 6.3 shows the YZ-plane reconstruction through the wire intersection for both biasing schemes. The elevational FWHM resolution was 396 μm for the identity-matrix encoded scheme and 369 μm for the Hadamard encoded scheme.

The theoretical lateral resolution, determined by the array's 10 MHz center frequency, 9.79 mm aperture size, and the 12.8 mm phantom depth, was calculated using $1.4f_{\#}\,\lambda$ to be 270 μm. Here, $f_{\#}$ is the ratio of the focal distance to the aperture size, and λ is the wavelength. The observed resolution values are slightly larger than the 270 μm theoretical lateral resolution when assuming a 10 MHz photoacoustic signal. The theoretical resolution was predicted using a 10 MHz center frequency, the center frequency of the array. In actuality, the center frequency of the measured photoacoustic signal was closer to 8 MHz with a 20 dB bandwidth of approximately 10 MHz. Along with nonidealities of the array, this may explain the discrepancies between the predicted and measured resolution.". Since azimuthal resolution is determined from the row-measurements and elevational resolution is obtained retrospectively through decoding, the two resolutions are not expected to be perfectly symmetrical. Imperfect reconstructions are likely due to several dead row/columns across the array introducing artifacts in the decoding process. In addition, it is possible that in either case the wires are not exactly within the reconstruction plane resulting in some distortion on the wire edges. The imaging performance of both biasing schemes is summarized in Table VIII.

Table VIII: Summary of Imaging Results

	Identity Matrix Bias Pattern	Hadamard Matrix Bias Encoding
Axial Resolution (μm)	250	220
Elevational Resolution (μm)	396	369
Azimuthal Resolution (μm)	487	311
SNR (dB)	8.8	25.3

By reconstructing with 61 azimuthal lines and 31 elevational lines, a reconstruction volume resolution chosen to be fine enough to measure point resolutions without large computation times, a 3D reconstruction of the crossed wires was obtained, as shown in Figure 6.4.

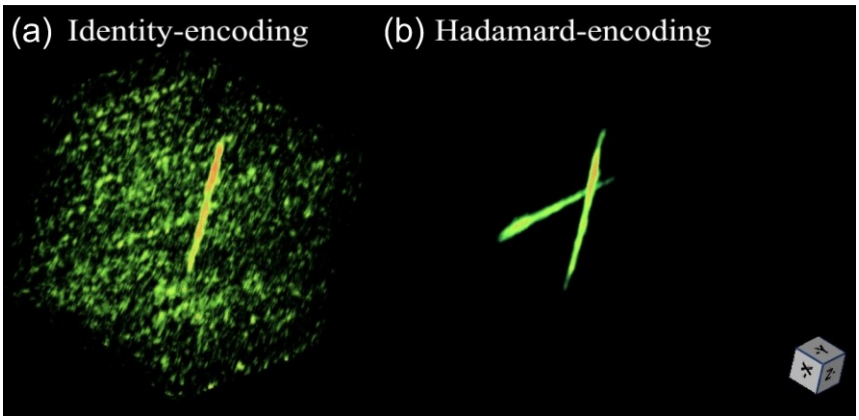

Figure 6.4: 3D reconstruction of crossed wires in scattering medium using (a) Identity matrix bias sequence (no encoding) and (b) Hadamard-bias encoding (see Visualization 1).

6.4 Conclusion and Future Work

The use of Hadamard-bias encoded imaging allows for acquisition across the whole array during the entire imaging sequence while also acquiring signals from all individual elements through the use of mathematical decoding. As a result, substantial SNR and resolution benefits were observed when compared with the single-column biasing approach. Since both approaches allow for 3D focusing, it is likely that the apparent resolution improvements observed with Hadamard bias encoding are due to the improved SNR. The 16.5 dB improvement observed when using Hadamard-bias encoding rather than identity matrix-bias encoding is slightly lower than the 18 dB theoretical improvement, potentially due to nonuniform element sensitivities.

Future work will involve in vivo imaging and increasing the imaging speed by using solid-state switching circuitry and high repetition-rate lasers. Additionally, larger TOBE arrays can be used without a substantial increase in channel count.

Chapter 7: Realtime 3D Ultrasound and Photoacoustic Imaging System Design

Most experimental results demonstrated for the FORCES and Hadamard photoacoustic imaging schemes used relay-based bias switching hardware and CPU-based decoding and beamforming software. As a result, the acquisition time of a FORCES volume with 31 elevational slices is ~30 minutes, and ~2 minutes for Hadamard-encoded photoacoustic imaging. The CPU-based reconstruction time of FORCES and Hadamard-encoded photoacoustic imaging is ~40 minutes and ~8 minutes, respectively. Ideally, both the acquisition time and reconstruction time would be above 20 frames/sec for realtime imaging. In order to achieve this, both the hardware and software is modified to incorporate solid-state bias switching and GPU-based reconstruction.

7.1 TOBE Array Interface PCB Design

The relay-based TOBE interface PCB is shown in Figure 5.3. 64 Single Pole Double Throw (SPDT) switches are located on a separate PCB and controlled with a ULN2803 relay driver and a microcontroller. These relays have a switching speed of approximately 100 ms. To both reduce the size of the bias switching electronics as well as increase bias switching speed, HV2761 switching integrated circuits are used instead. Voltage measurements of the bias switching from -20 V to +20V using the HV2761 are shown in Figure 7.1. The time to transition to 80% of the final voltage level is 1.6 µs, which is equivalent to an acoustic propagation distance of 1.2 mm in water. This means that the voltage can be switched while acquiring with a 1.2 mm depth "dead zone" in the measured data.

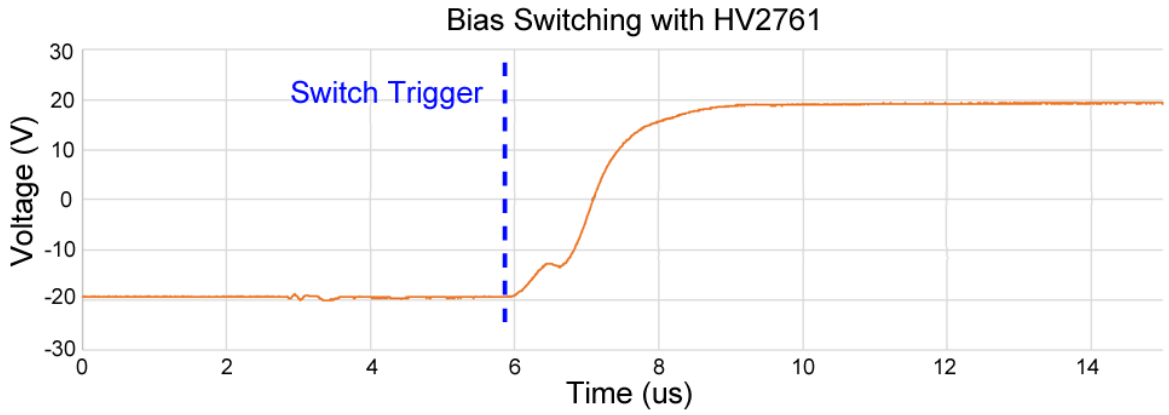

Figure 7.1: Voltage switching from -20 V to +20 V using HV2761. The blue line represents the bias switch trigger. The switch time to reach 80% of the final voltage level is 1.6 µs.

While the bias can be switched within this time scale, it is also important to determine whether the polarity of the electrostrictive material can switch this quickly. To measure this, a +50 V bias was applied to the relaxor array and a 40 V transmit pulse was applied. The pressure signal trace at 2 cm from the array surface was measured with a hydrophone. The bias is then switched from +50

V to -50 V and a second transmit pulse was applied after some delay time t_D. This second pressure trace is measured and compared with the first to calculate the phase shift. Since the array is under a positive bias during the first transmit and a negative bias during the second, we expect a 180° phase shift between them, as was shown in Figure 5.4 (c). Figure 7.2 shows that the effect remains true even when the second transmit pulse arrives $t_c = 2.6$ µs after the bias switch with a 174° phase shift.

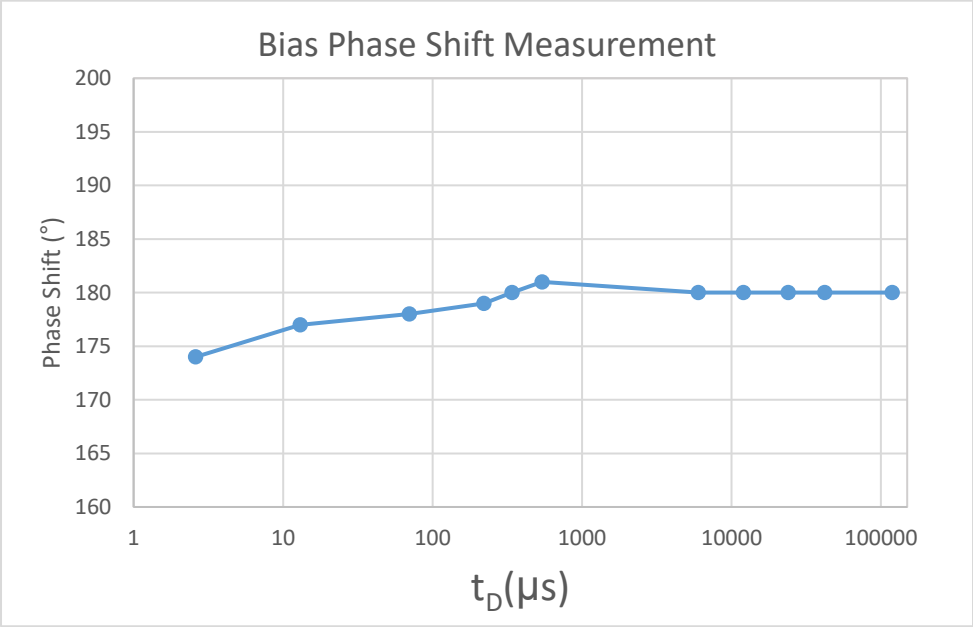

Figure 7.2: Electrostrictive relaxor array bias switching experiment. t_c represents the time between a bias transition from ground to +50V and an applied 40 V transmit pulse. The normalized pressure measured from a hydrophone characterizes the degree to which the

An interface board which uses these HV2761 switching ICs was designed and shown in Figure 7.3. The DC outputs of the HV2761s connect to the channel lines through bias tees consisting of 2.2 nH inductors and 4700 pF capacitors. These values provide sufficient high-pass and low-pass

filtering, respectively, while having a ~82 MHz resonance frequency which is sufficiently far from the operating frequencies to prevent unwanted oscillations. Four layers were used in this design, the top and bottom layers were mainly used for shielding to improve SNR. Signals are routed from the array and through the bias tees to strip the DC bias and then through micro-coaxial cables to

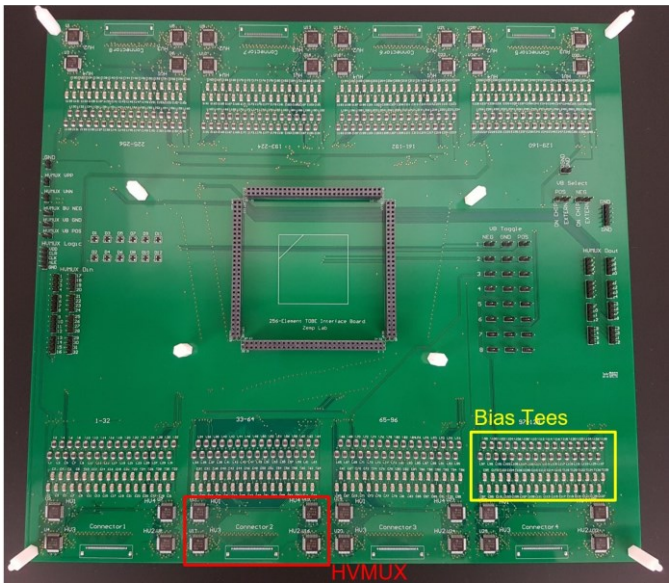

Figure 7.3: TOBE array interface board with HV2761 high-speed bias switching ICs highlighted in red, and bias tees in yellow. The center headers support arrays up to 128×128 elements, which are mounted on a separate PCB. The board connects to the Verasonics acquisition system via micro-coaxial cables.

the Verasonics system for digitization.

Using this system, the acquisition time for a single FORCES B-scan (64 acquisition with 64 different bias patterns) was measured to be 43 ms. This is a ~148× speed improvement over relay-based switching, and allows for acquisition rates of up to 23 frames/sec. Using a bin size of 2 would result in a 46 frames/sec acquisition rate with minimal compromises on imaging quality. This could be improved further by using a faster clock speed on the microcontroller used to program the HV2761s.

The volumetric acquisition rate of Hadamard-encoded photoacoustic imaging was previously limited by the relay-based switching speed. In this case, since the solid-state switching is substantially faster, the acquisition rate is instead limited by the 100 Hz repetition rate of the laser. For a 64×64 element array without binning, this results in an acquisition rate of 1.56 volumes/sec. Faster repetition rate lasers are available which could improve the acquisition rate.

Using solid-state switching, realtime B-scan acquisition is possible using the FORCES approach with near-realtime ultrasound and photoacoustic volumetric imaging.

7.2 GPU-Accelerated Reconstruction

Reconstructing 3D ultrasound is computationally expensive due to the large 3D imaging grids. This is compounded by the need for decoding when using TOBE bias-coding approaches. Using the FORCES imaging scheme, the decoding and delay-and-sum reconstruction time of a single B-scan with the i7-4790k 4.4 GHz processor is 101s. For 31 elevational planes, the volumetric reconstruction rate is 0.00032 volumes/sec.

To dramatically improve reconstruction rates for realtime imaging, parallelization can be used. CUDA is a general-purpose programming interface for parallel computing on NVIDIA graphical processing units (GPUs). By distributing the decoding and beamforming calculations across a GPU using CUDA, much faster reconstruction can be achieved.

Parallel calculations, or threads, are divided into blocks in the CUDA architecture, where each block contains a set number of threads, typically 128 or 256. These blocks can be arranged and visualized as being three dimensional, which is useful in the case of 3D beamforming. Figure 7.4

illustrates how calculations are organized across the 3D grid. A B-scan is calculated for each channel, and then summed across all channels for a SAI B-scan.

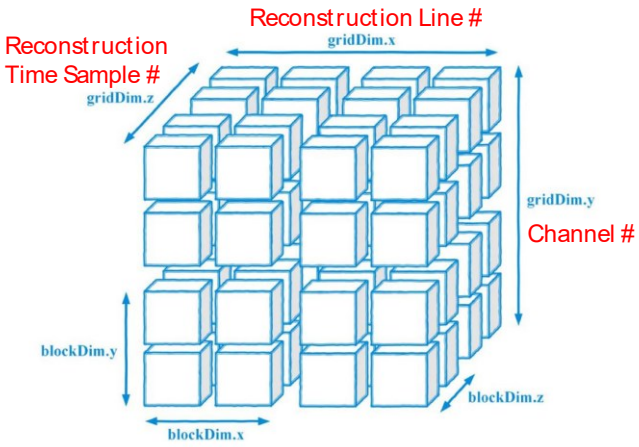

Figure 7.4: FORCES reconstruction CUDA block calculation diagram, based on [99]. Each pixel (the time sample and line number) is calculated for each channel. The results are then compounded across channels to form a single B-scan.

CUDA also allows for data to be stored as texture memory. This can be beneficial for beamforming since texture memory has hardware-based linear interpolation. This means that when accessing the raw input data, interpolated values between data points can be directly accessed without any

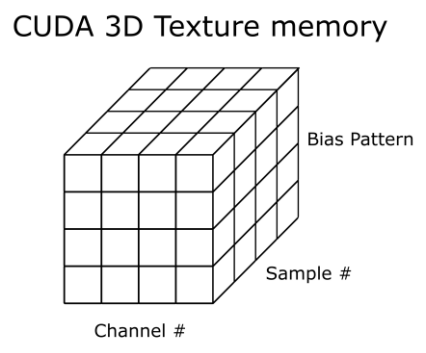

Figure 7.5: Diagram of 3D texture memory storage of FORCES channel data.

additional calculations. Figure 7.5 shows a diagram of how channel data was stored on 3D texture memory.

Channel data decoding was performed using the NVIDIA cuBLAS linear algebra library. The FORCES CUDA reconstruction code is shown in Appendix A: FORCES 3D Ultrasound GPU (CUDA) Reconstruction Code. Using an NVIDIA Titan V GPU, the reconstruction time for a single B-scan is 39 ms or 25.6 frames/sec. With 31 elevational slices the volumetric reconstruction rate is 0.806 volumes/second, a 2,370× speed improvement over the CPU-based approach.

In the case of Hadamard-encoded photoacoustic imaging, the full volume is reconstructed at once rather than in steps of B-scans, but the channel data storage and calculation grid can be structured in a similar manner to what was previously described. In addition to this delay-and-sum beamforming approach, a frequency-domain-based approach is possible for photoacoustic beamforming which is described in [86] for a linear array with 2D beamforming. Instead of calculating pixel/voxel values by summing the delayed channel values, this frequency-domain approach uses temporal backward projection. This assumed that the pressure wave can be described as

$$p(x,y,z,t) = -\rho_0 \frac{\partial \varphi(x,y,z,t)}{\partial t} \tag{7.1}$$

where ρ_0 is the density of the medium and $\varphi(x,y,z,t)$ is the velocity potential which can be written in the form of the homogenous wave equation

$$\frac{\partial^2 \varphi(x,y,z,t)}{\partial^2 t} = c^2 \Delta \varphi(x,y,z,t) \tag{7.2}$$

where c is the speed of sound in the medium. By relating the received channel data to the propagated pressure waves, the original pressure sources $p(x, y, z, t = 0)$ can be calculated using a spatial inverse Fourier transform which is described in detail in [86] for the 2D case. This approach was extended to a 3D space for volumetric photoacoustic reconstruction and the code is shown in Appendix B: Hadamard Encoded 3D Photoacoustic GPU Beamforming in Fourier Space. A comparison of TOBE array photoacoustic reconstruction times is shown in Figure 7.6. Using Fourier-based temporal backward projection, 11.5 volumes/second were reconstructed with 81×81×500 voxels in the reconstruction grid.

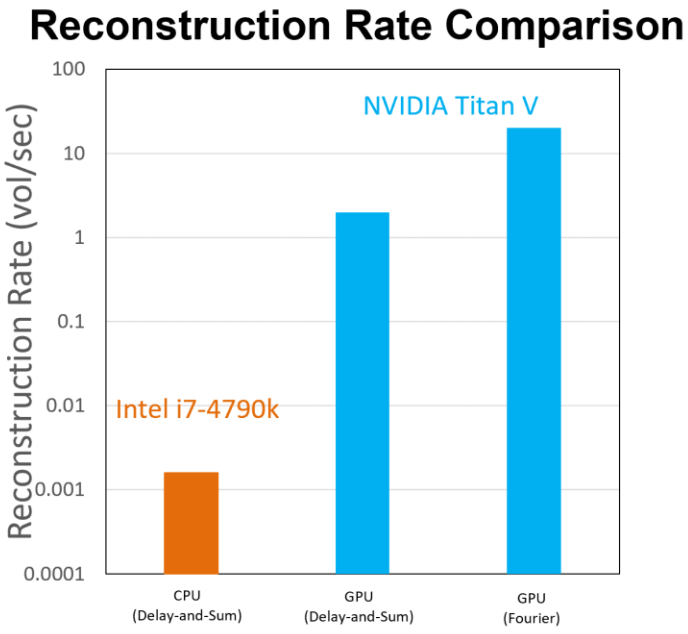

Figure 7.6: Comparison of TOBE array photoacoustic volumetric reconstruction times using CPU (orange) and GPU (blue) approaches. Both delay-and-sum and Fourier-based temporal backward projection were tested on the GPU. The 3D simulation space consisted of 81×81×500 voxels in all cases.

Chapter 8: Conclusion

Ultrasound imaging is widely used for 2D imaging but faces many technical challenges when extended to 3D. This has hindered the adoption of 3D ultrasound imaging systems despite there being a wide variety of clinical applications such as imaging tumors, large organs, and biopsy needle tracking. 3D photoacoustic imaging is an emerging technology capable of imaging optical characteristics, such as the oxygen saturation in blood, at greater depths than optical-only methods but is also limited by existing 2D array technology. TOBE arrays offer the possibility of overcoming the primary challenge in building large 2D ultrasound arrays: the large number of channels needed to drive a 2D array. This is because TOBE arrays require only 2N channels rather

than N^2 for a N×N array. TOBE arrays have been shown to provide comparable imaging quality to linear array, but they also suffer from limitations due to the lack of connections to individual elements. This results in the inability to transmit elevationally and azimuthally simultaneously and the inability to receive along individual elements to build a true 2D array dataset.

This thesis describes techniques which leverages the bias-sensitive characteristics of electrostrictive relaxor composite and capacitive micromachined ultrasound transducer arrays to enable greater 3D imaging flexibility and performance with TOBE arrays.

A key performance metric of TOBE arrays is the ability to isolate the activity of individual elements. This metric will have a direct impact on imaging performance, particularly when utilizing the row and column biases for array control. A comprehensive optimization study is performed on a simulated TOBE CMUT array analyzing which factors impact the dominant-element isolation. It was found that by maximizing the CMUT gap height, minimizing the AC pulse and DC bias, and maximizing the membrane radius, the dominant-element isolation could be maximized. However, minimizing the AC driving waveform and DC bias will also limit the transmit amplitude, decreasing the SNR. CMUTs are becoming increasingly popular in modern ultrasound systems, and their bias-sensitivity makes them excellent candidate transducers for TOBE arrays. This model provides a tool for designing large-scale TOBE CMUT arrays where the relationship between the array parameters and imaging characterizes can be explored. While the lumped-element equivalent circuit CMUT model has been shown to have good agreement with finite element CMUT deflection simulations in [2], this model neglects higher-order harmonics in the membrane mechanics which may have a significant impact with very large displacements or with driving functions far from the center frequency. This model is also unable to simulate the

membrane completely snapping down. This special case can be useful since snapped-down membranes will have different frequency characteristics, allowing for multimode operation [87]. Recently, a lumped-element model has been developed which incorporates snap-down (collapse-mode) operation [88].

Circuit-level CMUT simulations were also linked with Field II acoustic field simulations to investigate the impact of crosstalk on the transmitted pressure waveforms. In the work shown here, the combined circuit-level and field-level simulation array size is limited to 10×10 due to memory constraints. This is not large enough for practical array simulations, and future improvements in the simulation model would allow for simulated transmit and receive imaging sequences of physical arrays where the simulated channel data could be used to reconstruct images.

A TOBE bias-encoding approach for 3D ultrasound imaging called Fast Orthogonal Row-Column Electronic Scanning (FORCES) is presented which uses Hadamard bias-encoding along with electronics transmit focusing for simultaneous azimuthal and elevational transmit focusing. This results in two-way azimuthal focusing, a feature lacking in most previously proposed TOBE imaging methods but present in most linear array imaging schemes. Unlike linear arrays however, FORCES uses electronic steering for elevational focusing without the need for a mechanical stepper. The FORCES approach was found in simulation to have superior 3D cyst imaging resolution and SNR when compared with a commonly used 3D imaging scheme, Explososcan. Experimentally, the FORCES scheme was demonstrated to have superior wire phantom 3D resolution and SNR to the rectilinear row-column imaging approach and equivalent 2D imaging performance to a linear array using flash angle compounding. This imaging schemes overcomes one of the main limitations of previous 3D schemes, the poor 2D imaging quality. Since FORCES

can achieve near-equivalent imaging quality to that of linear arrays with a similar number of channels, it could effectively replace a linear array-based imaging system providing the added advantage of elevational scanning. The main disadvantage of the FORCES scheme is the number of acquisitions required for volumetric imaging. Each B-scan with a N×N array requires N acquisition, although this can be reduced with some tradeoffs. For a volume consisting of 31 B-scans at a maximum depth of 5 cm, a 64×64 element array can reach an imaging speed of ~8 volumes/second, which may not be sufficient for many applications such as cardiac imaging or Doppler flow imaging. While using bias binning will decrease the number of acquisitions needed, this will also increase the effective size of the transmit or receive elements, decreasing image quality. An alternative solution to this is to use a non-square M×N coding matrix rather than the Hadamard matrix, where M is the number of acquisitions and N is the number of elements. Even though this matrix can't be inverted and therefore can't be directly used in equation 6.3, compressive sensing [89] and neural network-based approaches [90] have been showed to be effective reconstruction methods for similar problems and offer a potential solution here. In contrast to Explososcan, the FORCES approach combines multiple B-scans to form a 3D volume rather than reconstructing the volume directly. This means that there will be distinct differences in the azimuthal and elevational resolution since the elevational resolution will be dependent on the array's focusing ability. Future potential TOBE 3D ultrasound imaging schemes could use biases encoding both in transmit and receive, allowing for a full 2D array dataset. This would permit beamforming of the entire volume with a homogeneous azimuthal and elevational resolution. While in theory this approach would provide as much information as a fully connected 2D array, the fully connected array using multiplexing or micro-beamforming would likely provide better imaging performance since the decoding process can introduce artifacts when there are element

sensitivity variations. The fully connected array would also acquire volume at a faster rate than a bias-encoded TOBE scheme, since only a single acquisition may be needed. Future developments in array interposer electronics could make large-scale 2D fully connected arrays feasible and would have these performance advantages over TOBE arrays.

A 3D photoacoustic imaging approach called Hadamard bias-encoded photoacoustic imaging was presented which allows for a full 2D array dataset to be acquired using N acquisition (or fewer with bias binning) for a N×N array. Compared with a previous approach where single columns were biased individually, the scheme presented here allows for the entire array to receive during all acquisition providing a theoretical $\sqrt{N}$ factor SNR improvement. Through wire phantom experiments in an intralipid scattering medium, the SNR of the Hadamard bias-encoding approach was 25.3 dB and 8.8 dB for the previously demonstrated scheme without bias-coding. The Hadamard-encoded approach also showed a 37.1% improvement in azimuthal resolution, likely due to the higher SNR. Hadamard bias-encoded photoacoustic imaging offers the ability to acquire full 2D-array datasets at the cost of additional acquisitions. Most other 3D photoacoustic imaging experiments have used mechanically scanned linear arrays. While this linear array approach has relatively slow elevational scanning speed and poor elevational resolution compared with the bias-encoded TOBE approach, a linear array would provide much faster B-scan imaging since only a single acquisition may be needed. This is especially important in photoacoustic imaging since the imaging speed is typically limited by the laser pulse repetition rate which is on the order of ms.

Both ultrasound and photoacoustic 3D ultrasound imaging benefit from larger array sizes since increased aperture size will improve SNR and lateral resolution. In theory, electrostrictive or CMUT-based TOBE arrays could be expanded to much greater sizes and element counts than what

has previously been possible. These very-large scale TOBE arrays could offer unprecedented 3D imaging quality for existing applications as well as explore new applications such as full-organ imaging.

Bibliography

[1] P. Beard, A. M. Hurrell and T. N. Mills, "Characterization of a polymer film optical fiber hydrophone for use in the range 1 to 20 MHz: A comparison with PVDF needle and membrane hydrophones.," *IEEE Transactions on ultrasonics, ferroelectrics, and frequency control,* vol. 47, no. 1, pp. 256-264, 2000.

[2] H. Koymen, A. Atalar, E. Aydogdu, C. Kocabas, H. K. Oguz, S. Olcum, A. Ozgurluk and A. Unlugedik, "An improved lumped element nonlinear circuit model for a circular CMUT cell," *IEEE transactions on ultrasonics, ferroelectrics, and frequency control,* vol. 59, no. 8, pp. 1791-1799, 2012.

[3] R. E. Davidsen, S. R. Freeman and B. J. Savord, "Matrix ultrasound probe with passive heat dissipation". US Patent 9,730,677, 17 August 2017.

[4] R. Solomon and B. Savord, "Fully sampled matrix transducer for real time 3D ultrasonic imaging," *2003 IEEE Symposium on Ultrasonics,* vol. 1, pp. 945-953, 2003.

[5] D. P. Shattuck, M. D. Weinshenker, S. W. Smith and O. T. von Ramm, "Explososcan: A parallel processing technique for high speed ultrasound imaging with linear phased arrays," *The Journal of the Acoustical Society of America,* vol. 75, no. 4, pp. 1273-1282, 1984.

[6] M. F. Rasmussen, G. Férin, R. Dufait and J. A. Jensen, "Comparison of 3D synthetic aperture imaging and explososcan using phantom measurements," *IEEE Ultrasonics Symposium (IUS),* pp. 113-116, 2012.

[7] C. H. Seo and J. T. Yen, "A 256 x 256 2-D array transducer with row-column addressing for 3-D rectilinear imaging," *IEEE transactions on ultrasonics, ferroelectrics, and frequency control,* vol. 56, no. 4, 2009.

[8] C. E. Demore, A. W. Joyce, K. Wall and G. R. Lockwood, "Real-time volume imaging using a crossed electrode array," *IEEE transactions on ultrasonics, ferroelectrics, and frequency control,* vol. 56, no. 6, pp. 1252-1261, 2009.

[9] Y. Wang, S. Hu, K. Maslov, Y. Zhang, Y. Xia and L. V. Wang, "In vivo integrated photoacoustic and confocal microscopy of hemoglobin oxygen saturation and oxygen partial pressure," *Optics letters,* vol. 36, no. 7, pp. 1029-1031, 2011.

[10] R. J. Paproski, A. Heinmiller, K. Wachowicz and R. J. Zemp, "Multi-wavelength photoacoustic imaging of inducible tyrosinase reporter gene expression in xenograft tumors," *Scientific reports,* vol. 4, p. 5329, 2014.

[11] B. Yin, D. Xing, Y. Wang, Y. Zeng, Y. Tan and Q. Chen, "Fast photoacoustic imaging system based on 320-element linear transducer array," *Physics in medicine and biology,* vol. 47, no. 9, p. 1339, 2004.

[12] C. Ceroici and R. J. Zemp, "Large-Scale Nonlinear Lumped and Integrated Field Simulations of Top-Orthogonal-to-Bottom-Electrode CMUT Architectures," *IEEE Transactions on Ultrasonics, Ferroelectrics, and Frequency Control,* vol. 64, no. 7, pp. 1087 - 1091, 2017.

[13] C. Ceroici, M. Maadi and R. J. Zemp, "Nonlinear lumped modelling of large-scale CMUT TOBE architectures," in *IEEE International Ultrasonics Symposium*, 2015.

[14] C. Ceroici and R. J. Zemp, "Measurements and Large-Scale Simulations of CMUT TOBE Array Parasitic Effects," in *Micromachined Ultrasound Transducers*, 2016.

[15] C. Ceroici, T. Harrions and R. J. Zemp, "Fast Orthogonal Row–Column Electronic Scanning With Top-Orthogonal-to-Bottom Electrode Arrays," *IEEE Transactions on Ultrasonics, Ferroelectrics, and Frequency Control,* vol. 64, no. 6, pp. 1009-1014, 2017.

[16] C. Ceroici and R. J. Zemp, "Fast Orthogonal Row-Column Electronic Scanning (FORCES) Experiments and Comparison," *IEEE Transactions on Ultrasonics, Ferroelectrics and Frequency Control,* pp. (Accepted, awaiting publication), 2018.

[17] C. Ceroici, K. Latham, R. Chee, J. A. Brown and R. J. Zemp, "Bias-sensitive crossed-electrode relaxor 2D arrays for 3D photoacoustic imaging," in *SPIE Photonics West*, San Francisco, 2018.

[18] C. Ceroici, Y. Fu, K. Latham, J. A. Brown and R. J. Zemp, "Crossed-Electrode Relaxor 2D Arrays and GPU Reconstruction for fast 3D Photoacoustic-Ultrasound Imaging," in *SPIE Photonics West*, San Francisco, 2019.

[19] C. Ceroici, K. Latham, R. Chee, B. Greenlay, Q. Barber, J. A. Brown and R. J. Zemp, "3D photoacoustic imaging using Hadamard-bias encoding with a crossed electrode relaxor array," *Optics letters,* vol. 43, no. 14, pp. 3425-3428, 2018.

[20] R. Chee, A. Sampaleanu, D. Rishi and R. J. Zemp, "Top orthogonal to bottom electrode (TOBE) 2-D CMUT arrays for 3-D photoacoustic imaging," *IEEE transactions on ultrasonics, ferroelectrics, and frequency control,* vol. 61, no. 8, pp. 1393-1395, 2014.

[21] T. L. Szabo, Diagnostic ultrasound imaging: inside out, Academic Press, 2004.

[22] J. Huang, J. K. Triedman, N. V. Vasilyev, Y. Suematsu, R. O. Cleveland and P. E. Dupont, "Imaging artifacts of medical instruments in ultrasound-guided interventions," *Journal of Ultrasound in Medicine,* vol. 26, no. 10, pp. 1303-1322, 2007.

[23] A. Rosencwaig and A. Gersho, "Theory of the photoacoustic effect with solids," *Journal of Applied Physics,* vol. 47, no. 1, 1976.

[24] F. A. McDonald and G. C. Wetsel Jr, "Generalized theory of the photoacoustic effect," *Journal of Applied Physics,* vol. 49, no. 4, pp. 2313-2322, 1979.

[25] A. P. Jathoul, J. Laufer, O. Ogunlade, B. Treeby, B. Cox, E. Zhang and M. F. Lythgoe, "Deep in vivo photoacoustic imaging of mammalian tissues using a tyrosinase-based genetic reporter," *Nature Photonics,* vol. 9, no. 4, pp. 239-246, 2015.

[26] E. Zhang, J. Laufer and P. Beard, "Backward-mode multiwavelength photoacoustic scanner using a planar Fabry-Perot polymer film ultrasound sensor for highresolution three-dimensional imaging of biological tissues," *Applied Optics,* vol. 47, no. 4, pp. 561-577, 2008.

[27] P. Beard, "Biomedical photoacoustic imaging," *Interface focus,* p. rsfs20110028, 2011.

[28] M. Xu and L. V. Wang, "Photoacoustic imaging in biomedicine," *Review of scientific instruments,* vol. 77, no. 4, p. 041101, 2006.

[29] J. Xia, M. Chatni, K. Maslov, Z. Guo, K. Wang, M. Anastasio and L. V. Wang, "Whole-body ring-shaped confocal photoacoustic computed tomography of small animals in vivo," *Journal of Biomedical Optics,* vol. 17, no. 5, p. 050506 , 2012.

[30] P. Ephrat, L. Keenliside, A. Seabrook, F. S. Prato and J. J. Carson, "Three-dimensional photoacoustic imaging by sparse-array detection and iterative image reconstruction," *Journal of Biomedical Optics,* vol. 13, no. 5, pp. 054052-054052, 2008.

[31] R. K. Chee, A. Sampaleanu, D. Rishi and R. J. Zemp, "Top orthogonal to bottom electrode (TOBE) 2-D CMUT arrays for 3-D photoacoustic imaging," *IEEE transactions on ultrasonics, ferroelectrics, and frequency control,* vol. 61, no. 8, pp. 1393-1395, 2014.

[32] K. E. Thomenius, "Evolution of ultrasound beamformers," in *Proceedings IEEE International Ultrasonic Symposium*, 1996.

[33] J. A. Jensen, S. I. Nikolov, K. L. Gammelmark and M. H. Pedersen, "Synthetic aperture ultrasound imaging," *Ultrasonics,* vol. 44, no. e5-e15, 2006.

[34] M. O'Donnell and Y. Wang, "Coded excitation for synthetic aperture ultrasound imaging," *IEEE transactions on ultrasonics, ferroelectrics, and frequency control,* vol. 52, no. 2, pp. 171-176, 2005.

[35] N. Sloane, T. Fine, P. G. Phillips and M. Harwitt, "Codes for multiplex spectrometry," *Applied Optics,* vol. 8, no. 10, pp. 2103-2106, 1969.

[36] A. Fenster, A. Landry, D. B. Downey, R. A. Hegele and J. D. Spence, "3D ultrasound imaging of the carotid arteries," *Current Drug Targets-Cardiovascular & Hematological Disorders,* vol. 4, no. 2, pp. 161-175, 2004.

[37] O. V. Solberg, F. Lindseth, H. Torp, R. Blake and T. A. N. Hernes, "Freehand 3D Ultrasound Reconstruction Algorithms—A Review," *Ultrasound in Medicine & Biology,* vol. 33, no. 7, pp. 991-1009, 2007.

[38] G. O. Unsgaard, O. M. Rygh, T. Selbekk, T. B. Muller, F. Kolstag, F. Lindseth and T. N. Hernes, "Intra-operative 3D ultrasound in neurosurgery," *Acta neurochirurgica,* vol. 148, no. 3, pp. 235-253, 2006.

[39] F. Cenni, D. Monari, K. Desloovere, E. Aertbeliena, S. H. Schless and H. Bruyninckx, "The reliability and validity of a clinical 3D freehand ultrasound system," *Computer Methods and Programs in Biomedicine,* vol. 136, pp. 179-187, 2016.

[40] J. Provost, C. Papadacci, J. E. Arango, M. Imbault, M. Fink, J. Gennisson, M. Tanter and M. Pernot, "3D ultrafast ultrasound imaging in vivo," *Physics in Medicine & Biology,* vol. 59, no. 19, p. L1, 2014.

[41] M. A. Bell, B. C. Byram, E. J. Harris, P. M. Evans and J. C. Bamber, "In vivo liver tracking with a high volume rate 4D ultrasound scanner and a 2D matrix array probe," *Physics in Medicine & Biology,* vol. 57, no. 5, p. 1359, 2012.

[42] B. Savord and R. Solomon, "Fully sampled matrix transducer for real time 3D ultrasonic imaging," *IEEE Symposium on Ultrasonics,* vol. 1, pp. 945-953, 2003.

[43] M. M. Nguyen, S. Huang, S. Zhou, C. Hu, N. Ledoux, B. Savord, V. Shamdasani and H. Xie, "Real-Time X-Plane Shear Wave Elastography Feasibility on Philips 2D xMatrix Transducer," *IEEE International Ultrasonics Symposium,* pp. 1-9, 2018 .

[44] H. Jeffrey, "Ultrasound Transducer Assembly Having Improved Thermal Management". U.S. Patent 11/912,617, 7 August 2008.

[45] A. Austeng and S. Holm, "Sparse 2-D arrays for 3-D phased array imaging-design methods," *IEEE transactions on ultrasonics ferroelectrics, and frequency control,* vol. 49, no. 8, pp. 1073-1086, 2002.

[46] S. I. Nikolov and J. A. Jensen, "Application of different spatial sampling patterns for sparse array transducer design," *Ultrasonics,* vol. 37, no. 10, pp. 667-671, 2000.

[47] G. R. Lockwood, J. R. Talman and S. S. Brunke, "Real-time 3-D ultrasound imaging using sparse synthetic aperture beamforming," *IEEE transactions on ultrasonics, ferroelectrics, and frequency control,* vol. 45, no. 4, pp. 980-988, 1998.

[48] C. E. Morton and G. R. Lockwood, "Theoretical assessment of a crossed electrode 2-D array for 3-D imaging," *IEEE Symposium on Ultrasonics,* vol. 1, pp. 968-971, 2003.

[49] Y. Q. Chen, Y. X. Li, Y. Chen, Z. Y. Ju, L. Q. Tap, Y. Pang, Y. Yang and T. L. Ren, "Large-Scale and High-Density pMUT Array Based on Isolated Sol-Gel PZT Membranes for Fingerprint Imaging," *Journal of The Electrochemical Society,* vol. 164, no. 7, pp. B377-B381, 2017.

[50] T. L. Christensen, M. F. Rasmussen, J. P. Bagge, L. N. Moesner, J. A. Jensen and E. V. Thomsen, "3-D imaging using row–column-addressed arrays with integrated apodization—part II: Transducer fabrication and experimental results," *Transducer fabrication and experimental results. IEEE transactions on ultrasonics, ferroelectrics, and frequency control,* vol. 62, no. 5, pp. 959-971, 2015.

[51] A. S. Logan, L. L. Wong and J. T. Yeow, "2-D CMUT wafer bonded imaging arrays with a row-column addressing scheme," *IEEE International Ultrasonics Symposium,* pp. 984-987, 2009.

[52] M. Engholm, T. L. Christiansen, C. Beers, J. P. Bagge, L. N. Moesner, H. Bouzari and E. V. Thomsen, "A hand-held row-column addressed CMUT probe with integrated electronics for volumetric imaging.," *IEEE International Ultrasonics Symposium,* pp. 1-4, 2015.

[53] M. Flesch, M. Pernot, J. Provost, G. Ferin, A. Nguyen-Ding, M. Tanter and T. Deffieux, "4D in vivo ultrafast ultrasound imaging using a row-column addressed matrix and coherently-compounded orthogonal plane waves," *Physics in Medicine & Biology,* vol. 62, no. 11, p. 4571, 2017.

[54] M. F. Rasmussen and J. A. Jensesn, "3D ultrasound imaging performance of a row-column addressed 2D array transducer: a simulation study," *International Society for Optics and Photonics.,* vol. 8675, p. 86750C, 2013.

[55] N. M. Daher and J. T. Yen, "Rectilinear 3-D ultrasound imaging using synthetic aperture techniques," *IEEE Ultrasonics Symposium,* vol. 2, pp. 1270-1273, 2004.

[56] A. Sampleanu and R. J. Zemp, "Synthetic aperture 3D ultrasound imaging schemes with S-sequence bias-encoded top-orthogonal-to-bottom-electrode 2D CMUT arrays," *2013 IEEE International Symposium on Ultrasonics,* pp. 1994-1997, 2013.

[57] M. F. la Cour, T. L. Christiansen, J. A. Jenson and E. V. Thomsen, "Electrostatic Analysis of CMUTs with Circular and Square Anisotropic Plates," *IEEE Transactions on Ultrasonics, Ferroelectrics and Frequency Control,* pp. 1-13, 2014.

[58] M. Vallet, Varray F., J. M. Boutet, J. M. Dinton, G. Caliano, A. S. Savoia and D. Vray, "Quantitative comparison of PZT and CMUT probes for photoacoustic imaging: Experimental validation," *Photoacoustics,* vol. 8, pp. 48-58, 2017.

[59] B. Greenlay and R. J. Zemp, "CMUT isolated isolation posts," *IEEE International Ultrasonics Symposium,* pp. 1-1, 2017.

[60] R. E. Davidsen and S. W. Smith, "Relaxor ferroelectric materials in two-dimensional transducer arrays," *IEEE Ultrasonics Symposium,* vol. 2, pp. 1283-1286, 1995.

[61] S. M. Pilgrim, "Electrostrictive ceramics for low-frequency active transducers," *IEEE transactions on ultrasonics, ferroelectrics, and frequency control,* vol. 47, no. 4, pp. 861-876, 2000.

[62] A. F. Devonshire, "Theory of ferroelectrics," *Advances in physics,* vol. 3, no. 10, pp. 85-130, 1954.

[63] K. Latham, C. A. Samson, A. Bezanson, R. Adamson and J. A. Brown, "Design and preliminary experimental results for a high-frequency crossed electrode phased array, based on a reconfigurable Fresnel lens," *2016 IEEE International Symposium on Ultrasonics,* pp. 1-4, 2016.

[64] O. Oralkan, A. S. Ergun, C. Ching-Hsiang, J. A. Johnson, M. Karaman, T. H. Lee and B. T. Khuri-Yakub, "Volumetric ultrasound imaging using 2-D CMUT arrays," *IEEE Transactions on Ultrasonics, Ferroelectrics and Frequency Control,* vol. 50, no. 11, pp. 1581-1984, 2003.

[65] A. Sampleanu, P. Zhang, A. Kshirsagar, W. Moussa and R. J. Zemp, "Top-orthogonal-to-bottom-electrode (TOBE) CMUT arrays for 3-D ultrasound imaging," *IEEE transactions on ultrasonics, ferroelectrics, and frequency control,* vol. 61, no. 2, pp. 266-276, 2014.

[66] H. Koymen, M. N. Senlik, A. Atalar and S. Olcum, "Parametric linear modeling of circular cMUT membranes in vacuum," *IEEE transactions on ultrasonics, ferroelectrics, and frequency control,* vol. 54, no. 6, pp. 1229-1239, 2007.

[67] H. K. Oguz, S. Olcum, M. N. Senlik, V. Tas, A. Atalar and H. Koymen, "Nonlinear modeling of an immersed transmitting capacitive micromachined ultrasonic transducer for harmonic balance analysis," *IEEE transactions on ultrasonics, ferroelectrics, and frequency control,* vol. 57, no. 2, pp. 438-447, 2010.

[68] I. O. Wygant, M. Kupnik and B. T. Khuri-Yakub, "Analytically calculating membrane displacement and the equivalent circuit model of a circular CMUT cell," *IEEE Ultrasonics Symposium,* pp. 2111-2114, 2008.

[69] J. A. Jensen, "Field: A program for simulating ultrasound systems," *10th NordicBaltic Conference on Biomedical Imaging,* vol. 4, no. 1, pp. 351--353, 1996.

[70] P. Zhang, G. Fitzpatrick, T. Harrison, W. A. Moussa and R. J. Zemp, "Double-SOI wafer-bonded CMUTs with improved electrical safety and minimal roughness of dielectric and electrode surfaces," *Journal of Microelectromechanical Systems,* vol. 21, no. 3, pp. 668-680, 2012.

[71] J. T. Yen, C. H. Seo, S. I. Awad and J. S. Jeong, "A dual-layer transducer array for 3-D rectilinear imaging," *IEEE Transactions on Ultrasonics, Ferroelectrics and Frequency Control,,* vol. 56, no. 1, pp. 204-212, 2009.

[72] A. S. Logan, L. L. Wong, A. L. Chen and J. T. Yeow, "A 32x32 element row-column addressed capacitive micromachined ultrasonic transducer," *IEEE Transactions on Ultrasonics, Ferroelectrics and Frequency Control,* vol. 58, no. 6, pp. 1266-1271, 2011.

[73] M. F. Rasmussen, T. L. Christiansen, E. V. Thomsen and J. A. Jensen, "3-D imaging using row-column-addressed arrays with integrated apodization-Part I: Apodization design and line element beamforming," *IEEE transactions on ultrasonics, ferroelectrics, and frequency control,* vol. 62, no. 5, pp. 947-958, 2015.

[74] S. Bennet, D. K. Peterson, D. Corl and G. S. Kino, "A real-time synthetic aperture digital acoustic imaging system," *Acoust. Imaging,* vol. 10, pp. 669-692, 1982.

[75] J. Ylitalo and H. Ermert, "Ultrasound synthetic aperture imaging: monostatic approach," *IEEE Transactions on Ultrasonics Ferroelectrics, and Frequency Control,* vol. 41, no. 3, pp. 333-339, 1994.

[76] N. Sloane, T. Fine, P. G. Phillips and M. Harwitt, "Codes for multiplex spectrometry," *Applied Optics,* vol. 8, no. 10, pp. 1203-2106, 1969.

[77] S. I. Nikolov and J. A. Jensen, "Fast Simulation of Ultrasound Images," *IEEE International Ultrasonics Symposium,* vol. 2, pp. 1721-1724, 2000.

[78] S. Park and T. R. Shrout, "Ultrahigh strain and piezoelectric behavior in relaxor based ferroelectric single crystals," *Journal of Applied Physics,* vol. 4, no. 1804-1811, p. 82, 1997.

[79] A. Savoia, V. Bavaro, G. Caliano, A. Caronti, R. Carotenuto, P. Gatta, C. Longo and M. Pappalardo, "P2B4 Crisscross 2D cMUT Array: Beamforming Strategy and Synthetic 3D Imaging Results," *IEEE Ultrasonics Symposium,* pp. 1514-1517, 2007.

[80] R. Y. Chiao, L. J. Thomas and S. D. Silverstein, "Sparse array imaging with spatially-encoded transmits," *IEEE Ultrasonics Symposium,* vol. 2, pp. 1679-1682, 1997.

[81] K. Latham, C. Samson, C. Ceroici, R. J. Zemp and J. A. Brown, "Fabrication and performance of a 128-element crossed-electrode relaxor array, for a novel 3D imaging approach," *IEEE International Ultrasonics Symposium,* pp. 1-4, 2017.

[82] K. Latham, C. Ceroici, C. Samson, R. J. Zemp and J. A. Brown, "Simultaneous Azimuth and Fresnel Elevation (SAFE) Compounding: A Fast 3D Imaging Technique for Crossed Electrode Arrays," *IEEE transactions on ultrasonics, ferroelectrics, and frequency control,* vol. 65, no. 9, pp. 1657-1668, 2018.

[83] Y. Wang, Z. Guo, L. V. Wang, T. N. Erpelding, L. Jankovic, J. L. Robert and G. David, "In vivo three-dimensional photoacoustic imaging based on a clinical matrix array ultrasound probe," *Journal of Biomedical Optics,,* vol. 17, no. 6, p. 061208, 2012.

[84] W. G. Fateley, R. M. Hammaker, J. V. Paukstelis, S. L. Wright, E. A. Orr, A. N. Mortensen and K. J. Latas, "Application of a two-dimensional Hadamard encoding mask for the imaging of thin-layer chromatography plates by laser-induced fluorescence or surface-enhanced Raman scattering and for use with a photoacoustic detector to generate three-dimensional photoaco," *Applied spectroscopy,* vol. 47, no. 9, pp. 1464-1470, 1993.

[85] H. Coufal, U. Moller and S. Schneider, "Photoacoustic imaging using the Hadamard transform technique," *Applied optics,* vol. 21, no. 1, pp. 116-120, 1982.

[86] K. P. Kostli, M. Frenz, H. Bebie and H. P. Weber, "Temporal backward projection of optoacoustic pressure transients using Fourier transform methods," *Physics in Medicine & Biology,* vol. 46, no. 7, p. 1863, 2001.

[87] O. Oralkan, B. Bayram, G. G. Yaralioglu, A. S. Ergun, M. Kupnik, D. T. Yeh, I. O. Wygant and B. T. Khuri-Yakub, "Experimental characterization of collapse-mode CMUT operation," *IEEE transactions on ultrasonics, ferroelectrics, and frequency control,* vol. 53, no. 8, pp. 1513-1523, 2006.

[88] E. Aydogdu, A. Ozgurluk, A. Atalar and H. Koymen, "Parametric nonlinear lumped element model for circular CMUTs in collapsed mode," *IEEE transactions on ultrasonics, ferroelectrics, and frequency control,* vol. 61, no. 1, pp. 173-181, 2014.

[89] H. Liebgott, A. Basarab, D. Kouame, O. Bernard and D. Friboulet, "Compressive sensing in medical ultrasound," *IEEE International Ultrasonics Symposium,* pp. 1-6, 2012.

[90] M. Mardani, E. Gong, J. Y. Cheng, S. Vasanawala, G. Zaharchuk, M. Alley, N. Thakur, S. Han, W. Dally, J. M. Pauly and L. Xing, "Deep generative adversarial networks for compressed sensing automates MRI," *arXiv preprint arXiv:1706.00051,* 2017.

[91] J. Shen, C. Simon, O. S. Haddadin, S. Lucas and E. S. Ebbini, "A new pulse-echo system for real-time 3D ultrasonic imaging-phantom tests," *Ultrasonics Symposium,* vol. 2, pp. 1387-1390, 1996.

[92] J. F. Synnevag, A. Austeng and S. Holm, "Adaptive beamforming applied to medical ultrasound imaging," *IEEE transactions on ultrasonics, ferroelectrics, and frequency control,* vol. 54, no. 8, pp. 1606-1613, 2007.

[93] T. Harrison, A. Sampaleanu and R. J. Zemp, "S-sequence spatially-encoded synthetic aperture ultrasound imaging," *IEEE transactions on ultrasonics, ferroelectrics, and frequency control,* vol. 61, no. 5, pp. 886-890, 2014.

[94] R. J. Zemp, C. Ceroici and T. Harrison, "Practical S-Sequence aperture coding schemes for volumetric imaging with Top Orthogonal to Bottom Electrode (TOBE) arrays," *2015 IEEE International Ultrasonics Symposium,* pp. 1-4, 2015.

[95] S. A. Morris and C. G. Hutchens, "Implementation of Mason's model on circuit analysis programs," *IEEE transactions on ultrasonics, ferroelectrics, and frequency control,* vol. 33, no. 3, pp. 295-298, 1986.

[96] B. A. Greenlay and R. J. Zemp, "Fabrication of Linear Array and Top-Orthogonal-to-Bottom Electrode CMUT Arrays With a Sacrificial Release Process," *IEEE transactions on ultrasonics, ferroelectrics, and frequency control,* vol. 64, no. 1, pp. 93-107, 2017.

[97] S. Satir and F. L. Degertekin, "A computationally efficient nonlinear system model for CMUT arrays," 2014. [Online]. Available: http://ieeexplore.ieee.org/document/6932162. [Accessed 23 10 2017].

[98] Y. Roh and B. T. Khuri-Yakub, "Finite element analysis of underwater capacitor micromachined ultrasonic transducers," *IEEE transactions on ultrasonics, ferroelectrics, and frequency control,* vol. 49, no. 3, pp. 293-298, 2002.

[99] X. Liu, H. Zhao, G. Zhan, K. Zhong, Z. Li, Y. Chao and Y. Shi, "Rapid and automatic 3D body measurement system based on a GPU–Steger line detector," *Applied optics,* vol. 55, no. 21, pp. 5539-5547, 2016.

Appendix A: FORCES 3D Ultrasound GPU (CUDA) Reconstruction Code

The following C++ code is used for reconstructing 3D volumes using multiple elevation slices of data from the FORCES imaging scheme. The input is the raw column channel data from the array encoded with the Hadamard matrix. The code is implemented as a MATLAB MEX file to efficiently transfer channel data from the Verasonics MATLAB interface to the GPU and C++ environment and then display the data using MATLAB. This code uses the NVIDIA CUBLAS library for GPU-based matrix operations.

```
#include "mex.h"
#include "gpu/mxGPUArray.h"
#include <cstdlib>
#include "cublas_v2.h"

#include <stdio.h>
#include <stdlib.h>

#include "cuda_runtime.h"
#include "device_launch_parameters.h"
#include "cuda.h"
#pragma comment(lib, "cublas.lib")

//            Frequently used data such as polar coordinate arrays are stored in
//            constant memory for faster access
__constant__ float sin_theta_gpu[256];
__constant__ float cos_theta_gpu[256];
__constant__ float R_gpu[1500];

using namespace std;

// Initialize texure memory used for storing channel data
texture<float, cudaTextureType2DLayered, cudaReadModeElementType> tex;
#define FULL_MASK 0xffffffff
```

```
// Kernel for inverting data from columns with negative biases
__global__ void decoding_negation_kernel(float *Hadmard, float *channel_data_flat, float
*negated_channel_data_flat, int max_time, int n_ele){
	int sa = blockIdx.x;
	int ele = blockIdx.y;
	int t_idx = blockIdx.z;
	__shared__ float H_value;
	H_value = Hadmard[sa+ele*n_ele];
	int thIdx = max_time*n_ele*sa + ele*max_time + t_idx * max_time/2 + threadIdx.x;
	negated_channel_data_flat[thIdx] = H_value*channel_data_flat[thIdx];
}

// Kernal for decoding channel data using matrix multiplication with inverted Hadamard
matrix
void decoding_kernel_cublas(float *invH, float *channel_data_flat, float *outdata, int
max_time, int n_ele){
	int lda=max_time*n_ele,ldb=n_ele,ldc=n_ele*max_time, m=max_time*n_ele;
	const float alf = 1.0f;
    const float bet = 0.0f;
    const float *alpha = &alf;
    const float *beta = &bet;
    // Create a handle for CUBLAS
    cublasHandle_t handle;
    cublasCreate(&handle);
    // Perform multiplication
    cublasSgemm(handle, CUBLAS_OP_N, CUBLAS_OP_N, m, n_ele, n_ele, alpha,
channel_data_flat, lda, invH, ldb, beta, outdata, ldc);
    // Destroy the handle
    cublasDestroy(handle);
}
```

```
// mex function for interface with MATLAB and transfering data
void mexFunction(int nlhs, mxArray *plhs[],
                 int nrhs, mxArray const *prhs[]){
       int max_time;
       int no_lines;
       int n_ele = 64;
       float c_speed = 1540 * 0.94;
       int sample_rate = 36000000;
       float pitch = 153e-6;
       float kerf = 30e-6;
       float R_max = 30e-3;
       float R_min = 5e-3;
       mxGPUArray const *channel_data_flat;
       mxGPUArray *bf_data;
       mxGPUArray const *Hadmard;
       mxGPUArray const *invH;
       mxGPUArray *channel_data_flat_decoded;
       mxGPUArray *channel_data_flat_copied;

       float *ptr_channel_data_flat;
       float *ptr_bf_data;
       float *ptr_Hadmard;
       float *ptr_invH;
       float *ptr_channel_data_flat_decoded;
       float *ptr_channel_data_flat_copied;

       // Initialize the MathWorks GPU API
       mxInitGPU();

       // Initialize GPU memory
       channel_data_flat = mxGPUCreateFromMxArray(prhs[0]);
       ptr_channel_data_flat = (float *)(mxGPUGetDataReadOnly(channel_data_flat));
       Hadmard = mxGPUCreateFromMxArray(prhs[1]);
       ptr_Hadmard = (float *)(mxGPUGetDataReadOnly(Hadmard));
       invH = mxGPUCreateFromMxArray(prhs[2]);
       ptr_invH = (float *)(mxGPUGetDataReadOnly(invH));
       no_lines = mxGetScalar(prhs[3]);
       max_time = mxGetScalar(prhs[4]);
       mwSize dims_a[] = {n_ele*max_time*n_ele, 1};
       channel_data_flat_copied = mxGPUCreateGPUArray(2,
                            dims_a,
                            mxSINGLE_CLASS,
                            mxGPUGetComplexity(channel_data_flat),
                            MX_GPU_DO_NOT_INITIALIZE);
       ptr_channel_data_flat_copied = (float *)(mxGPUGetData(channel_data_flat_copied));
```

```
// kernal for performing synthetic aperture beamforming on decoded data
__global__ void PolarBF_kernel_SA(float* outdata, int max_time, int no_lines, int n_ele,
float c_speed, int sample_rate, float pitch, float kerf) {
	// Determine the polar coordinate (pixel) to calculate during kernal execution
	__shared__ float radius;
	int time = blockIdx.x;
	radius = R_gpu[time];
	__shared__ float sin_angle, cos_angle;
	int line = blockIdx.y;
	sin_angle = sin_theta_gpu[line];
	cos_angle = cos_theta_gpu[line];
	__shared__ float frame_ele_offset;
	int frame = blockIdx.z;
	frame_ele_offset = frame*pitch + (pitch - kerf) / 2 - (n_ele*pitch - kerf) / 2;
	float ele_offset = ele*pitch + (pitch - kerf) / 2 - (n_ele*pitch - kerf) / 2;

	// Calulate the delay value in samples
	float delay;
	float delay_sample;
	delay = (__fsqrt_rn((radius*sin_angle - ele_offset)*(radius*sin_angle -
ele_offset)+(cos_angle*radius)*(cos_angle*radius)) + __fsqrt_rn((radius*sin_angle -
frame_ele_offset)*(radius*sin_angle -
frame_ele_offset)+(cos_angle*radius)*(cos_angle*radius)))/c_speed;
	delay_sample = delay * sample_rate;
	if (delay_sample >= max_time)
		delay_sample = max_time - 1.0f;

	// Access the interpolated channel data using the sample value
	float Ch_data = tex2DLayered(tex, delay_sample+0.5f, ele+0.5f, frame+0.5f);

	for (int offset = 16; offset > 0; offset /= 2)
		Ch_data += __shfl_down_sync(FULL_MASK, Ch_data, offset);

	// Compound the synthetic aperture acquisitions
	if(threadIdx.x == 0 || threadIdx.x == 32)
		atomicAdd(&outdata[line*max_time + time], Ch_data);
}
```

```
	mwSize dims[] = {no_lines*max_time, 1};
	bf_data = mxGPUCreateGPUArray(2,
	                        dims,
	                        mxSINGLE_CLASS,
	                        mxGPUGetComplexity(channel_data_flat),
	                        MX_GPU_INITIALIZE_VALUES);

	ptr_bf_data = (float *)(mxGPUGetData(bf_data));

	mwSize dims_c[] = {n_ele*max_time*n_ele, 1};
	channel_data_flat_decoded = mxGPUCreateGPUArray(2,
	                        dims_c,
	                        mxSINGLE_CLASS,
	                        mxGPUGetComplexity(channel_data_flat),
	                        MX_GPU_INITIALIZE_VALUES);
	ptr_channel_data_flat_decoded = (float
	*)(mxGPUGetData(channel_data_flat_decoded));


	// Calculate beamforming grid
	float sector = 3.14159 / 3;
	float theta[256];
	float sin_theta[256];
	float cos_theta[256];
	float R[1500];
	for (int i = 0; i < no_lines; i++){
	       theta[i] = (i*((float)no_lines / ((float)no_lines - 1)) - (float)no_lines /
	2) / (float)no_lines*sector;
	       sin_theta[i] = sin(theta[i]);
	       cos_theta[i] = cos(theta[i]);
	}
	for (int i = 0; i < max_time; i++){
	       R[i] = R_min + i*(R_max - R_min)/(float)(max_time-1);
	}

	// Transfer grid arrays to GPU
	cudaMemcpyToSymbol(sin_theta_gpu, sin_theta, sizeof(float)*256);
	cudaMemcpyToSymbol(cos_theta_gpu, cos_theta, sizeof(float)*256);
	cudaMemcpyToSymbol(R_gpu, R, sizeof(float)*1500);

	// Initialize texure memory for channel data storage
	       cudaChannelFormatDesc channelDesc = cudaCreateChannelDesc(32, 0, 0, 0,
	cudaChannelFormatKindFloat);
	cudaArray* channelArray;
	cudaMalloc3DArray(&channelArray, &channelDesc, make_cudaExtent(max_time, n_ele,
n_ele), cudaArrayLayered);

	// Set texture parameters
	tex.addressMode[0] = cudaAddressModeClamp;
	tex.addressMode[1] = cudaAddressModeClamp;
	tex.addressMode[2] = cudaAddressModeClamp;
	tex.filterMode = cudaFilterModeLinear;
	tex.normalized = false;
```

```
// Invert negatively biased channels
       decoding_negation_kernel<<<dim3(n_ele, n_ele, 2), max_time/2>>>(ptr_Hadmard,
ptr_channel_data_flat, ptr_channel_data_flat_copied, max_time, n_ele);
       cudaDeviceSynchronize();
       // Perform decoding
       decoding_kernel_cublas(ptr_invH, ptr_channel_data_flat,
ptr_channel_data_flat_decoded, max_time, n_ele);

       // Bind decoded channel data to 3D texture
       cudaMemcpy3DParms p = { 0 };
       p.dstArray = channelArray;
       p.srcPtr = make_cudaPitchedPtr(ptr_channel_data_flat_decoded,
max_time*sizeof(float),max_time,n_ele);
       p.extent.width = max_time;
       p.extent.height = n_ele;
       p.extent.depth = n_ele;
       p.kind = cudaMemcpyDeviceToDevice;
       cudaMemcpy3D(&p);
       cudaBindTextureToArray(tex, channelArray, channelDesc);

       // Perform synthetic aperture beamforming
       PolarBF_kernel_SA <<<dim3(max_time, no_lines, n_ele), n_ele >>> (ptr_bf_data,
max_time, no_lines, n_ele, c_speed, sample_rate, pitch, kerf);

       // Set MEX output as beamformed data
    plhs[0] = mxGPUCreateMxArrayOnGPU(bf_data);

    // Destroy allocated GPU memory
    mxGPUDestroyGPUArray(channel_data_flat);
    mxGPUDestroyGPUArray(bf_data);
    mxGPUDestroyGPUArray(Hadmard);
    mxGPUDestroyGPUArray(invH);
    mxGPUDestroyGPUArray(channel_data_flat_decoded);
    mxGPUDestroyGPUArray(channel_data_flat_copied);
       cudaFreeArray(channelArray);
       //Unbind the texture for delay
       cudaUnbindTexture(tex);
}
```

Appendix B: Hadamard Encoded 3D Photoacoustic GPU Beamforming in Fourier Space

The following CUDA code performs a full volumetric reconstruction of photoacoustic data from a Hadamard-encoded row-electrode dataset. Rather than using delay-and-sum beamforming as is shown in Appendix A: FORCES 3D Ultrasound GPU (CUDA) Reconstruction Code, the following code is a CUDA implementation of the Fourier-domain temporal backprojection approach described analytically in [86]. This code uses the NVIDIA CUFFT library for GPU-based Fourier transforms.

```
#include <stdlib.h>
#include <stdio.h>
#include <string.h>
#include <math.h>
#include "mex.h"
#include "gpu/mxGPUArray.h"
#include <cuda_runtime.h>
#include "device_launch_parameters.h"
#include "cuda.h"
#include <cufft.h>
#pragma comment(lib, "cufft.lib")

// Frequency-domain grid stored in constant memory for faster access
__constant__ float kx_vec_gpu[3199];
__constant__ float ky_vec_gpu[64];
__constant__ float kz_vec_gpu[64];

// Complex data declaration
typedef float2 Complex;
static __device__ __host__ inline Complex ComplexAdd(Complex, Complex);
static __device__ __host__ inline Complex ComplexScale(Complex, float);
static __device__ __host__ inline Complex ComplexMul(Complex, Complex);
static __global__ void ComplexPointwiseMulAndScale(Complex *, const Complex *, int,
float);

// Declare 3D texture memory for channel data
texture<float2, cudaTextureType3D, cudaReadModeElementType> tex;
```

```
// Kernel for interpolation from time frequency domain to spatial frequency domain
__global__ void PA_fft_beamforming_kernel(Complex *fft_pressure_signal, Complex
*interpolated_pressure_signal, float c_speed, float dt, int flipped_time, int n_ele){
	int x_index = blockIdx.x; // Time
	int y_index = blockIdx.y; // Dimension for columns
	int z_index = threadIdx.x; // Dimension for rows
	float Kx_value = kx_vec_gpu[x_index];
	float Ky_value = ky_vec_gpu[y_index];
	float Kz_value = kz_vec_gpu[z_index];
	float w_K_value = c_speed * sqrt(Kx_value*Kx_value + Ky_value*Ky_value +
Kz_value*Kz_value);
	float w_K_index = w_K_value*dt*flipped_time/(2*3.14159);

	if(w_K_index > (flipped_time/2)){
		interpolated_pressure_signal[z_index*flipped_time*n_ele +
y_index*flipped_time + x_index].x = 0;
		interpolated_pressure_signal[z_index*flipped_time*n_ele +
y_index*flipped_time + x_index].y = 0;
	}
	else{
		interpolated_pressure_signal[z_index*flipped_time*n_ele +
y_index*flipped_time + x_index] = tex3D(tex, w_K_index+0.5f, y_index+0.5f, z_index+0.5f);
	}
}

// mex function for interface with MATLAB and transfering data
void mexFunction(int nlhs, mxArray *plhs[],
		 int nrhs, mxArray const *prhs[]){

	int max_time = 1600;
	int flipped_time = max_time*2-1;
	float pitch = 153e-6;
	int n_ele = 64;
	float c_speed = 1540 * 0.94;
	int sample_rate = 36000000;
	float dt = 1.0/(float)sample_rate;
    float dy, dz;
	dy = dz = pitch;
	mxGPUArray const *channel_data_flat;
	mxGPUArray *channel_data_flat_fft;
	mxGPUArray *channel_data_flat_fft_interpolated;
	Complex *ptr_channel_data_flat;
	Complex *ptr_channel_data_flat_fft;
	Complex *ptr_channel_data_flat_fft_interpolated;

	mxInitGPU();

	cudaEvent_t start, stop;
	cudaEventCreate(&start);
	cudaEventCreate(&stop);
	cudaEventRecord(start);

	channel_data_flat = mxGPUCreateFromMxArray(prhs[0]);
	ptr_channel_data_flat = (Complex *)(mxGPUGetDataReadOnly(channel_data_flat));
```

```
        mwSize dims_a[] = {n_ele*flipped_time*n_ele, 1};
        channel_data_flat_fft = mxGPUCreateGPUArray(2,
                                                    dims_a,
                                                    mxSINGLE_CLASS,
                                                    mxCOMPLEX,
                                                    MX_GPU_INITIALIZE_VALUES);
        ptr_channel_data_flat_fft = (Complex *)(mxGPUGetData(channel_data_flat_fft));

        channel_data_flat_fft_interpolated = mxGPUCreateGPUArray(2,
                                                                 dims_a,
                                                                 mxSINGLE_CLASS,
                                                                 mxCOMPLEX,

        MX_GPU_INITIALIZE_VALUES);
        ptr_channel_data_flat_fft_interpolated = (Complex
*)(mxGPUGetData(channel_data_flat_fft_interpolated));


        // Initialize frequency-domain grid
        float kx_vec[3199];
        float ky_vec[64];
        float kz_vec[64];

        // Calculate kx
        int i=0;
        for(;i<=(flipped_time-1)/2;i++){
                kx_vec[i] = 2*3.14159*i/(dt * c_speed * flipped_time);
        }
        for(;i<flipped_time;i++){
                kx_vec[i] = -1*kx_vec[flipped_time-i];
        }
        // Calculate ky,kz
        int j=0;
        for(;j<n_ele/2;j++){
                ky_vec[j] =  2*3.14159*j/(dy*n_ele);
                kz_vec[j] =  2*3.14159*j/(dz*n_ele);
        }
        for(;j<n_ele;j++){
                ky_vec[j] = -1*ky_vec[n_ele-1-j];
                kz_vec[j] = -1*kz_vec[n_ele-1-j];
        }
        cudaMemcpyToSymbol(kx_vec_gpu, kx_vec, sizeof(float)*flipped_time);
        cudaMemcpyToSymbol(ky_vec_gpu, ky_vec, sizeof(float)*n_ele);
        cudaMemcpyToSymbol(kz_vec_gpu, kz_vec, sizeof(float)*n_ele);

    // Initialize CUFFT Fourier transform
    cufftHandle plan;
    cufftPlan3d(&plan, n_ele, n_ele, flipped_time, CUFFT_C2C);

    // Transform signal and kernel
    cufftExecC2C(plan, (cufftComplex *)ptr_channel_data_flat, (cufftComplex
*)ptr_channel_data_flat_fft, CUFFT_FORWARD);
```

```
        // Bind Fourier-transformed channel data to texture memory
        cudaChannelFormatDesc channelDesc = cudaCreateChannelDesc(32, 32, 0, 0,
cudaChannelFormatKindFloat);

        cudaArray* channelArray;
        cudaMalloc3DArray(&channelArray, &channelDesc, make_cudaExtent(flipped_time,
n_ele, n_ele));
        tex.addressMode[0] = cudaAddressModeBorder;
        tex.addressMode[1] = cudaAddressModeBorder;
        tex.addressMode[2] = cudaAddressModeBorder;
        tex.filterMode = cudaFilterModeLinear;
        tex.normalized = false;

        cudaMemcpy3DParms p = { 0 };

        p.dstArray = channelArray;
        p.srcPtr = make_cudaPitchedPtr(ptr_channel_data_flat_fft,
flipped_time*sizeof(float2),flipped_time,n_ele);

        p.extent.width = flipped_time;
        p.extent.height = n_ele;
        p.extent.depth = n_ele;
        p.kind = cudaMemcpyDeviceToDevice;
        cudaMemcpy3D(&p);

        cudaBindTextureToArray(tex, channelArray, channelDesc);

        // Convert channel data from time domain to spatial frequency domain
        PA_fft_beamforming_kernel<<<dim3(flipped_time, n_ele, 1), n_ele>>>
(ptr_channel_data_flat_fft, ptr_channel_data_flat_fft_interpolated, c_speed, dt,
flipped_time, n_ele);
    cudaDeviceSynchronize();
    // Convert data back to time domain
    cufftExecC2C(plan, (cufftComplex *)ptr_channel_data_flat_fft_interpolated,
(cufftComplex *)ptr_channel_data_flat_fft_interpolated, CUFFT_INVERSE);

        // Set reconstructed array as MEX output
        plhs[0] = mxGPUCreateMxArrayOnGPU(channel_data_flat_fft_interpolated);

        // Clean up CUDA memory
    cufftDestroy(plan);
    mxGPUDestroyGPUArray(channel_data_flat);
    mxGPUDestroyGPUArray(channel_data_flat_fft);
    mxGPUDestroyGPUArray(channel_data_flat_fft_interpolated);
        cudaFreeArray(channelArray);
        cudaUnbindTexture(tex);
        cudaEventRecord(stop);
        cudaDeviceSynchronize();
}
```

```
// Complex addition
static __device__ __host__ inline Complex ComplexAdd(Complex a, Complex b)
{
    Complex c;
    c.x = a.x + b.x;
    c.y = a.y + b.y;
    return c;
}

// Complex scalar multiplication
static __device__ __host__ inline Complex ComplexScale(Complex a, float s)
{
    Complex c;
    c.x = s * a.x;
    c.y = s * a.y;
    return c;
}

// Complex multiplication
static __device__ __host__ inline Complex ComplexMul(Complex a, Complex b)
{
    Complex c;
    c.x = a.x * b.x - a.y * b.y;
    c.y = a.x * b.y + a.y * b.x;
    return c;
}

// Complex pointwise multiplication
static __global__ void ComplexPointwiseMulAndScale(Complex *a, const Complex *b, int
size, float scale)
{
    const int numThreads = blockDim.x * gridDim.x;
    const int threadID = blockIdx.x * blockDim.x + threadIdx.x;

    for (int i = threadID; i < size; i += numThreads)
    {
        a[i] = ComplexScale(ComplexMul(a[i], b[i]), scale);
    }
}
```